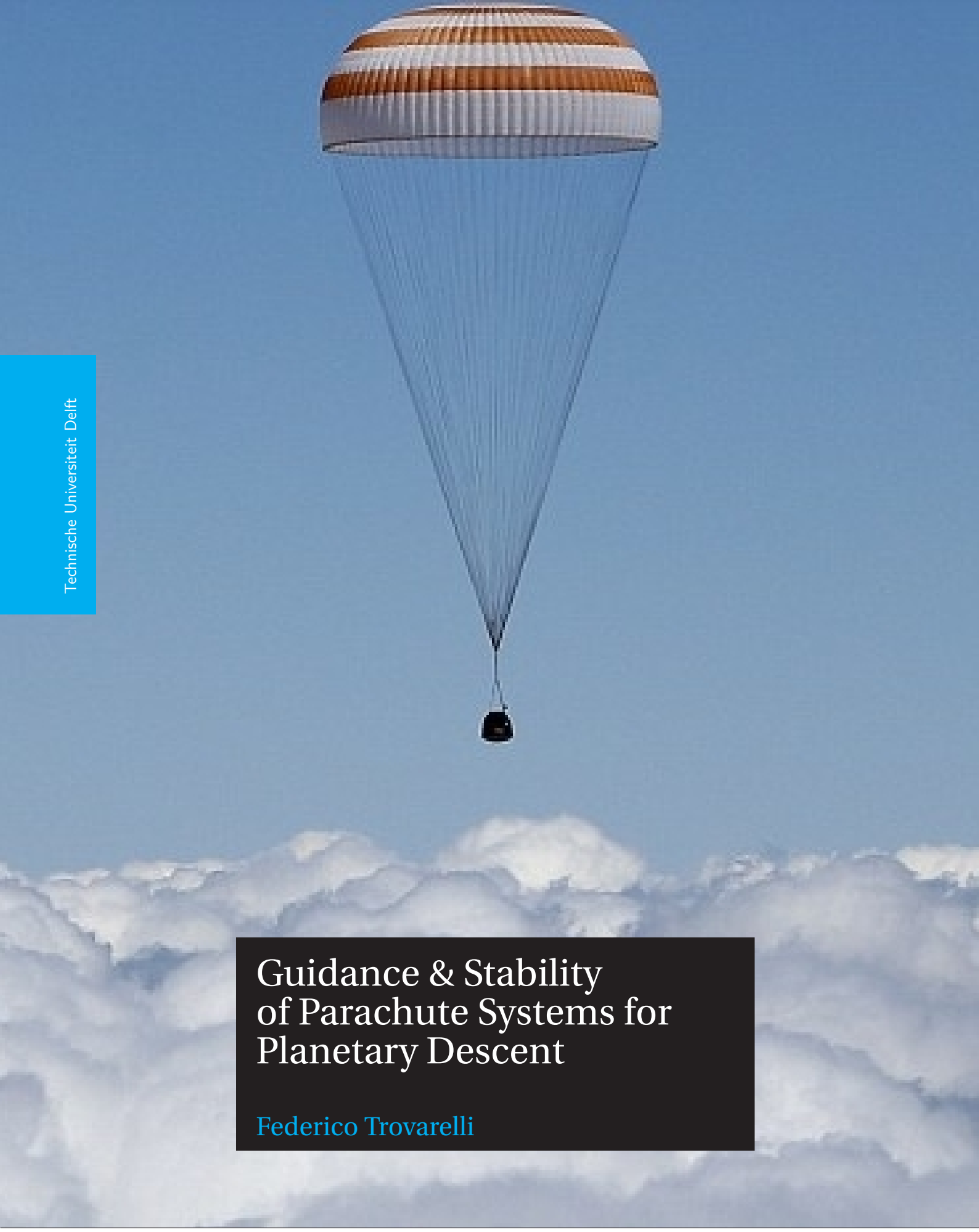

Technische Universiteit Delft

Guidance & Stability of Parachute Systems for Planetary Descent

Federico Trovarelli

TU Delft Delft University of Technology

Challenge the future

GUIDANCE & STABILITY OF PARACHUTE SYSTEMS FOR PLANETARY DESCENT

FEDERICO TROVARELLI

in partial fulfilment of the requirements for obtaining the degree of

Master of Science in Aerospace Engineering

at Delft University of Technology
to be defended publicly on Thursday March 29th, 2018 at 09:00

Student number:	4519132	
Committee members:	prof.dr.ir. P.N.A.M. Visser,	Delft University of Technology (Chairholder)
	ir. J.A. Melkert,	Delft University of Technology
	dr. ir. E. Mooij,	Delft University of Technology (Supervisor)

Cover Picture:	Soyuz Parachute Descent [AFP/Getty Images].
Date:	15th March, 2018

TU Delft Delft University of Technology

ACKNOWLEDGEMENTS

I hereby take this opportunity to thank my thesis supervisor, Erwin Mooij, for helping me to climb the last step for becoming an engineer. He taught me a lot in any sense and had the patience to insist with me when I was stubborn.

Also, I would like to thank the friends I grew up with in all the phases of my youth: Stefano, Leonardo, Francesco and Mattia, Riccardo and Daniele, Davide, Michele and Leonardo, Marco, Francesco, Paolo and Francesca, Stefano, Cristian and Giuseppe, Edoardo, Tommaso, Matteo, Antonio, Umberto, Luca Davide, Greta, Alessandro, Simone, Camilla, Lucrezia, Alessandro, Federica, Gabriele, Luigi, Alessandro, Luca, Simone and Matteo, Leon and Corné. Each of them has influenced somehow the person that I am now.

A special thank goes to my parents Marco and Francesca, who were always present when I needed them, to my sister Chiara, that will be my best friend for all my life, and to my grandparents, Bianca Maria, Nazareno, Magda and Lorenzo, who indirectly always remind me where I come from.

Finally, I would like to thank my girlfriend Giulia that is the icing on the cake of my life.

Federico Trovarelli
Delft, 15th March, 2018

ABSTRACT

Since the beginning of the new century, we are experiencing a renovated enthusiasm with respect to the human conquest of Mars, that now represents the greatest challenge for space engineering. Before sending a man to Mars, however, a number of technologies still need to be developed or improved. In this respect, entry, descent and landing is one of the most crucial research fields. In particular, a manned mission requests that a supply can be delivered within a short distance from a previously landed asset or inside a very tiny area. In response to these needs, NASA addressed the so called pinpoint landing accuracy requirement. A mission that satisfies this requirement shall be able to land its payload within 100 m from the nominal target.

A typical Mars entry, descent and landing mission consists of a hypersonic entry, a parachute deceleration phase and a powered terminal descent. This architecture derives from the successful Viking mission launched by NASA in 1975. The best landing accuracy up to now has been achieved by the Mars Science Laboratory mission, whose landing ellipse had a major axis of about 20 km. This was possible thanks to the implementation of a novel guidance system for controlling the trajectory of the spacecraft during the entry phase. The residual uncertainty is mainly due to navigation error, but also the atmospheric disturbances affecting the parachute flight play a significant role. After Mars Science Laboratory mission, in fact, the parachute descent remains the only unguided phase of a typical Mars entry, descent and landing mission.

Considering these, the objective of this research project is to understand whether a guidance system that can control the horizontal position of the parachute-backshell-payload spacecraft during the descent in the atmosphere of Mars, using the thrust generated by the backshell thrusters, represents a performing and efficient solution for compensating the disturbances affecting this flight phase and thus reducing the size of the final landing ellipse on the surface of the Red Planet.

The advantage of having a system that autonomously follows a reference descent trajectory comes at the cost of having on board a thrusters, fuel and a tank resulting in a non negligible additional mass and, most of all, that the use of thrust perturbs the dynamic behaviour of the vehicle. Because of this, before to develop a parachute descent guidance system, it is fundamental to understand how the parameters of the spacecraft influence its stability characteristics. The first step of the research consisted in the development of a rigid body model simulating the translational and attitude motion of the parachute-payload spacecraft. This model was then linearised for a descent flight in steady-state conditions. The analysis of the eigenmotion of the system, based on the study of its Jacobian matrix, highlighted the contrasting effect that the inertia and aerodynamic properties of the vehicle have on its dynamics.

At this point a PD controller for stabilizing the horizontal position and velocity of the spacecraft around a chosen reference equilibrium condition was designed, integrated with the available rigid body model and then tuned for obtaining the desired response. The resulting closed-loop system was also linearised for a steady-state descent flight. The analysis of its Jacobian yielded interesting information for understanding how the control action influences the dynamics of the system.

After this preliminary phase, a new multibody model based on the Neustadt methodology was developed. The response to gusts and turbulences obtained using this model, that simulates the relative motion of the parachute, backshell and payload elements, was used to characterize with more accuracy the stability properties of the vehicle and to determine a configuration that is appropriate for the integration of the descent guidance system. The final step consisted of evaluating the performance and efficiency of the closed-loop system with respect to different aspects of the guided descent flight.

The results of the analysis are encouraging. They show that the open-loop system naturally tends to the vertical flight condition at equilibrium velocity. In particular, the more the aerodynamic forces of the parachute are relevant with respect to the inertia properties of the vehicle, the more stable the system will be. The introduction of the control action due to the guidance system in the dynamics of the system results in the stabilization of its horizontal motion around a chosen position-velocity target. By adjusting the gains of the controller and the lengths of the risers it is possible to optimise the response of the closed loop-system. The simulations show that in a descent flight of about 60 s the system can compensate a horizontal position error up to 900 m with approximately 8 kg of fuel.

CONTENTS

LIST OF SYMBOLS

Roman

a	Speed of sound	[m/s]
$\mathbf{a}$	Acceleration vector	$[\mathrm{m/s^2}]$
A	Amplitude	[varies]
A	Jacobian matrix element	[varies]
$\mathbf{A}$	Jacobian matrix	[varies]
$\mathbf{A}$	State matrix	[varies]
$\mathbf{B}$	Input matrix	[varies]
c	Response	[varies]
$\mathbf{C}$	Output matrix	[varies]
$\mathbf{C}$	Rotation matrix	[−]
d	Nominal length	[m]
$\mathbf{D}$	Feedforward matrix	[varies]
C_D	Drag coefficient	[−]
C_L	Lift coefficient	[−]
C_l	Roll Moment coefficient	[−]
C_m	Pitch Moment coefficient	[−]
C_n	Yaw Moment coefficient	[−]
C_S	Side force coefficient	[−]
D	Drag force	[N]
D_0	Parachute diameter	[m]
E	Energy	[J]
f	Function	[varies]
$\mathbf{f}$	Multidimensional function	[varies]
$\mathbf{F}$	Force vector	[N]
g	Gravitational acceleration	$[\mathrm{m/s^2}]$
$\mathbf{g}$	Gravitational acceleration vector	$[\mathrm{m/s^2}]$
h	Altitude	[m]
$\mathbf{h}$	Hinge position vector	[m]
I	Moment of inertia	$[\mathrm{kg/m^2}]$
$\mathbf{I}$	Identity matrix	[−]
$\mathbf{I}$	Inertia tensor	$[\mathrm{kg/m^2}]$
I_{sp}	Thrust specific impulse	[s]
k	Parameter	[varies]
k	Elastic constant	[N/m]
$\mathbf{K}$	Gain matrix	[−]
K_d	Derivative controller gain	[−]
K_i	Integral controller gain	[−]
K_p	Proportional controller gain	[−]
l	Double pendulum bar length	[m]
L	Length	[m]
L	Lift force	[N]
$\mathbf{L}$	Position vector	[m]
m	Mass	$[\mathrm{kg}]$
M	Mach number	[−]
M	Moment	[Nm]
$\mathbf{M}$	Moment vector	[Nm]
N_{sus}	Number of suspension lines	[−]
$\mathbf{O}$	Origin of the reference frame	[varies]
p	Parachute porosity	[−]

p	Pressure	$[\mathrm{N/m^2}]$
P	Period	[s]
q_{dyn}	Dynamic pressure	$[\mathrm{N/m^2}]$
$\mathbf{r}$	Position vector	[m]
R	Radius	[m]
R	Universal gas constant	$[\mathrm{Jkg^{-1}K^{-1}}]$
R_M	Mars equatorial radius	[m]
S	Side force	[N]
S_{ref}	Reference surface	$[\mathrm{m^2}]$
t	Time	[s]
T	Temperature	[K]
T	Thrust	[N]
$\mathbf{T}$	Thrust vector	[N]
$\mathbf{T}$	Translation vector	[varies]
$\mathbf{u}$	Control vector	[varies]
$\mathbf{v}$	Generic vector	[−]
$\mathbf{v}_\lambda$	Eigenvector	[−]
V	Lyapunov function	[−]
V	Velocity	[m/s]
$\mathbf{V}$	Velocity vector	[m/s]
$\mathbf{W}$	Weight vector	[N]
x,y,z	x Cartesian position components	[m]
$\mathbf{x}$	State vector	[varies]
$\hat{\mathbf{x}}$	Unit vector	[−]
X,Y,Z	Reference frame axes	[−]
$\mathbf{y}$	Output vector	[varies]

Greek

α	Angle of attack	$[\mathrm{deg}]$
α	Generic angle	$[\mathrm{deg}]$
β	Sideslip angle	$[\mathrm{deg}]$
γ	Flight path angle	$[\mathrm{deg}]$
γ	Heat ratio capacity	$[-]$
δ	Latitude	$[\mathrm{deg}]$
Δ_l	Riser lengthening	[m]
Δ_{h_t}	Gust transient size	[m]
Δ_t	Time fraction	[s]
Δ_y	Horizontal position error	[m]
ϵ	Average rate of dissipation of turbulent kinetic energy	$[\mathrm{m}^2/\mathrm{s}^3]$
ζ	Damping factor	$[-]$
η	Kolmogorov length scale	[m]
θ	Attitude angle	$[\mathrm{deg}]$
θ	Pitch angle	$[\mathrm{deg}]$
$\ddot{\boldsymbol{\theta}}$	Rotational acceleration vector	$[\mathrm{deg}/\mathrm{s}^2]$
λ	Eigenvalue	$[-]$
$\boldsymbol{\lambda}$	Eigenvalue column vector	$[-]$
μ_M	Mars gravitational constant	$[\mathrm{m}^3/\mathrm{s}^2]$
ν	Kinematic viscosity	$[\mathrm{m}^2/\mathrm{s}]$
ρ	Density	$[\mathrm{kg}/\mathrm{m}^3]$
ρ	Radial polar coordinate	[m]
σ	Bank angle	$[\mathrm{deg}]$
σ	Standard deviation	[varies]
τ	Longitude	$[\mathrm{deg}]$
τ_η	Kolmogorov time scale	[s]
ϕ	Roll angle	$[\mathrm{deg}]$
Φ	Suspension lines angle	$[\mathrm{deg}]$
χ	Heading angle	$[\mathrm{deg}]$
ψ	Yaw angle	$[\mathrm{deg}]$
ω	Frequency	[Hz]
ω_n	Natural frequency	[Hz]
$\boldsymbol{\omega}$	Angular velocity vector	$[\mathrm{deg}/\mathrm{s}]$

LIST OF ABBREVIATIONS

AGAS	Affordable Guided Airdrop System
AGU	Airborne Guidance Unit
CARP	Calculated Air Release Point
CEP	Circular Error Probable
COM	Centre Of Mass
COP	Centre Of Pressure
CPU	Central Processing Unit
DOF	Degrees Of Freedom
DUT	Delft University of Technology
EOM	Equations Of Motion
EDL	Entry, Descent and Landing
ESA	European Space Agency
EMCD	European Mars Climate Database
GCM	General Circulation Models
GNC	Guidance Navigation and Control
GPS	Global Positioning System
IC	Initial Conditions
IMU	Inertial Measurement Unit
LTI	Linear Time Invariant
MER	Mars Exploration Rover
MIMO	Multiple-Input Multiple-Output
MGP	Mars Guided Parachute
MPF	Mars PathFinder
MSc	Master of Science
MSL	Mars Science Laboratory
NASA	National Aeronautics and Space Administration
PID	Proportional Integral Derivative
PD	Proportional Derivative
ROSCOSMOS	Russian Agency for Aviation and Space
RSM	Response Surface Method
RTG	Radioisotope Thermal Generator
SISO	Single-Input Single-Output
TRN	Terrain Relative Navigation
UHF	Ultra High Frequency
USSR	Union of the Socialist Soviet Republics
USA	United States of America

1

INTRODUCTION

In the last 60 years space-technology advancement has been impressive. In 1969 human kind has been able to walk on another world, the Moon, and to safely come back home. From that moment on it was clear that the destiny of our species was to colonise other planets. It is the duty of space engineers to make it possible the conquest of the 21st century New World, Mars.

The first soft landing on the Red Planet, after many failed attempts, dates back to 19 June 1976 when the NASA lander Viking touched down in Chryse Planitia. The main purpose of the Viking mission was not only to increase the human knowledge of Mars, but also to validate a performing mission architecture that would have served as a basis for future missions. This architecture consisted of a hypersonic entry, a parachute deceleration phase and a powered terminal descent. Both these goals were fully achieved. Viking was followed by Mars Pathfinder (MPF) and Mars Exploration Rover (MER), in which new landing concepts were tested.

During these years also other countries invested in Mars EDL technology. In particular, ESA launched its first lander Beagle 2 in 2003, and Schiaparelli in 2016, as part of project ExoMars. The former touched down on Mars, but a failure of the solar panels obstructed any communication. The latter, instead, was not able to properly decelerate in the Martian atmosphere and impacted at high velocity on the surface.

All these missions were not designed for achieving high target accuracy at touchdown. In fact, as Figure 1.1 shows, the semi-major axis of the landing ellipses ranged from 140 km for Viking to 75 km for MER, and, as suggested by Portigliotti et al. [2010], was of the same order of magnitude also for Schiaparelli. After the first Mars missions, however, the objective of landing the first man on Mars as well as new scientific needs triggered the development of new technologies to ensure the capability to deliver a large cargo close to a previously landed asset or in a specific spot within a hazardous Martian region. For responding to this need, NASA addressed the so called *pinpoint landing accuracy requirement*, requesting that a payload can be landed within 100 m from its desired target. The first effort in this direction is represented by the launch of the Mars Science Laboratory (MSL) mission in 2011. In fact, thanks to the implementation of an autonomous guidance and control system for the hypersonic entry phase and to the development of a high performance descent system, the 900 kg rover Curiosity could be delivered inside a 10 km semi-major axis landing ellipse.

Even if MSL represented a significant advancement in Mars EDL technology, pinpoint landing accuracy is still far from being reached. According to Brand et al. [2004], the size of the landing ellipse on Mars depends on many factors that affect with variable magnitude the performance of one or more phases of the EDL sequence. These can be grouped into three areas: unknown variations of the Martian environment, errors due to imprecise knowledge of the interactions between the spacecraft and the Mars environment and errors of the GNC system. EDL engineering research mostly focuses on this last aspect. There exist a number of studies, such as Cheng-Chih [2006] and Wolf et al. [2011], that offer a survey of possible solutions for improving the design of EDL GNC systems to achieve better landing accuracy. These include more accurate navigation units based on orbital images and optical sensors and improved guidance an control strategies for the entry and powered descent phases. External perturbations during the entry phase and navigation error represent indeed the main source to landing inaccuracy. Terminal descent thrusters, instead, are already equipped on the vehicle for hazard avoidance and final deceleration purposes. The additional amount of control authority that they guarantee can eventually be also used for reducing the accumulated landing error.

Even if navigation and entry and terminal descent guidance are at the centre of current Mars EDL research efforts, there are also other topics whose result could be beneficial for landing accuracy. In particular, during

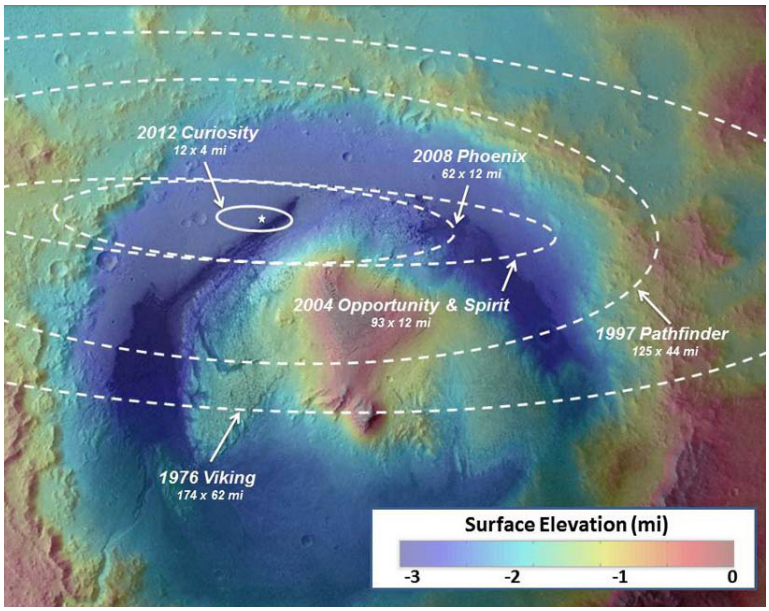

Figure 1.1: Improvements of landing accuracy for NASA Mars mission. Image credit: NASA/JPL

the parachute phase the vehicle is subjected gusts and atmospheric turbulence and the landing dispersion increases due to the presence of winds. Wolf et al. [2005] suggest that a system for guiding the spacecraft during this phase could compensate for the wind drift effect and significantly contribute to the reduction of the final landing ellipse. The final objective of the present study is then to determine the benefits that such a system can yield with respect to the landing accuracy problem on Mars. The question that arises is:

> *Can a guidance system for controlling the spacecraft parachute descent trajectory represent a performing and efficient solution for increasing the landing accuracy on Mars?*

To respond to this question, however, first the disturbances affecting the parachute descent phase have to be analysed. The question is:

Q1. *What are the most relevant external disturbances during the parachute descent on Mars?*

With this information it is now possible to determine some characteristics that the spacecraft should have. In particular, Wolf et al. [2005] introduces two possible solutions for the purpose of a guiding the spacecraft during the parachute descent on Mars. One consists of exploiting a steerable parachute for gliding in the desired direction while the other is based on the use of thrusters that can push the spacecraft towards the target. While the former approach is already used for military applications on Earth and some studies for adapting it to Mars delivery already exist, the potentialities of the latter concept have never been investigated. These considerations suggest the question:

Q2. *What actuators are more appropriate for controlling the spacecraft descent trajectory on Mars and what guidance strategy could be more performing?*

The results that we will obtain at the end of the study will be particularly influenced by the model that has been adopted for simulating the dynamics of the parachute-payload spacecraft. With respect to this aspect we want to know:

Q3. *What are the key characteristics of modelling the spacecraft as a rigid body or a multibody system? When are the differences between these two approaches significant?*

The motion of the parachute-payload spacecraft is characterized by some key parameters. It is important to know how these influence its dynamic stability properties and how they can be modified before to integrate the guidance system with the vehicle. Also, it is interesting to determine how the key parameters of the guidance system influence its response. In summary, the question is:

Q4. *How do the the key system parameters determine the dynamic properties of the parachute-payload spacecraft in both the cases of passive and guided descent?*

Once the information for responding to the previous questions is available, the performance of the parachute guided descent concept can be evaluated:

Q5. *How much control authority can the designed guided descent system yield and what target accuracy it can achieve? How is the system performance influenced in case of external perturbations?*

Clearly, the possibility to actively control the descent trajectory comes at a price. In particular, what is important to determine is:

Q6. *What are the disadvantages of controlling the parachute descent spacecraft trajectory with the designed system?*

Finally, it has to be considered that the guidance system that has been implemented interacts with real navigation and control subsystems. This suggests the question:

Q7. *How is the guided descent system influenced by the performance of the navigation and control subsystems of the spacecraft?*

The main research question and the corresponding sub-questions will be used as a guideline throughout the research projects. The following report layout has also been designed according to the research questions.

Chapter 2 introduces the exploration of the Red Planet and the problem of the landing accuracy that has driven the evolution of the technology of Mars EDL missions. In here, the possibility to realise a guidance and control system for the parachute descent phase that can help reducing the size of the final landing ellipse is discussed. Also, some existing concepts related to this topic are presented to determine whether their characteristics are appropriate for use on Mars. After this, the importance of the stability properties of parachute-payload systems and the influence that the dynamic model used has on the results of the analysis are also mentioned. The chapter is concluded by the description of the reference mission and vehicle, and the mission and system requirements that will drive the study.

The mathematical and physical background, including frame transformations, coordinate systems and other general concepts at the basis of flight dynamic studies, is presented in Chapter 3. This part is followed by the definition of a rigid-body model and, later, a multibody model based on the methodology of Neustadt et al. [1967], both describing the motion of the parachute-backshell-payload MPF reference vehicle. In Chapter 4 the characteristic environment of Mars, in which the EDL reference mission takes place, is described and modelled. In particular, it will focus on the atmospheric phenomena, such as winds, gusts and atmospheric turbulence, that are encountered in the planetary boundary layer and that have a significant effect on the trajectory and attitude dynamics of the spacecraft during its descent.

Chapter 5 describes instead the tools used during the project and the software architecture for implementing the models developed in Chapter 3 and integrated with the environment description from Chapter 4. Also, it documents their verification and validation.

The analysis phase starts in Chapter 6. Here, the rigid body model is linearised and its dynamic stability characteristics are studied analytically, according to classical stability theory, for the case of a steady-state descent flight. Chapter 7 introduces the parachute descent guidance system to be integrated with the models of the MPF reference spacecraft. The dynamic properties of the resulting closed-loop system are then analytically evaluated similarly to what has already been done in the previous chapter for the open-loop case.

Chapter 8 evaluates the response to gust and atmospheric turbulence of the MPF reference vehicle modelled as a multibody system. The aim is to determine its dynamic stability properties and an appropriate configuration for the implementation of the guidance system that can still guarantee robustness in presence of external disturbances. The chapter is concluded by the evaluation of the closed-loop system performance with respect to different aspects of the mission. Finally, Chapter 9 sums up the all the relevant information gathered during the project and gives a concise replies to the research questions stated earlier. Also, it includes some recommendations for continuing the research.

2

MISSION HERITAGE

In 1960, the first mission to Mars was launched by the Soviet Union, failing already at launch. From that moment on, many other missions were launched both by USSR and USA. The first successful flyby of the Red Planet was performed in 1969 by the American probe Mariner 6, while the Mariner 9 was capable of entering Mars orbit in 1971. Nevertheless, all of the landing attempts had failed, until the Americans launched the Viking missions in 1975.

In this chapter, first the most significant Mars EDL missions will be reviewed in Section 2.1 with the aim to understand what are their key characteristics and what advancements they brought to space technology. After this, in Section 2.2 the landing accuracy problem, already introduced in Chapter 1, will be discussed in more detail. This part is followed by the presentation of some autonomous descent concepts either for Earth or Mars use in Section 2.3. Section 2.4 discusses the importance of dynamic stability for parachute-payload vehicles and gives a brief overview of the available approaches for modelling the dynamics of these systems. Section 2.5 concludes the chapter with the description of a reference mission and vehicle and a collection of requirements that, togehter with research question, will serve as a guideline during the project.

2.1. THE EXPLORATION OF MARS

The Viking 1 & 2 spacecraft were launched from Cape Canaveral, both by means of a Titan-IIIE rocket. These probes consisted of an orbiter and a lander. Viking 1 touchdown, in 1976, represented the first soft Mars landing. All the following Mars missions, not only by NASA, referred to this one both in terms of mission profile and spacecraft design.

The objective of the Viking mission was to increase the human knowledge of the Martian environment, with particular focus on its possibility to support life. This could be done by means of orbital observations and direct measurements realised by the lander, whose instrumentation had been designed for acquiring data about biology, geology, meteorology and atmosphere, during the descent phase and after landing.

The Viking lander was protected by an aeroshell during the hypersonic entry phase and landed on three shock absorbing legs. Power was supplied by two Radioisotope Thermal Generators (RTG) and data transfer was guaranteed by an Ultra High Frequency (UHF) antenna pointing the orbiter and a safe-mode omni-directional S-band antenna to directly communicate with the Earth in case of signal losses. The lander had hydrazine engines dedicated to deorbit and landing operations, while a large parachute ensured deceleration and stability during the descent phase. Data were acquired by means of radar altimeter, Inertial Measurement Unit (IMU) and a four-beam Doppler radar. The total mass of the spacecraft at entry was 1185 kg, while the lander had a wet mass of 663 kg.

The mission consisted of a cruise phase followed by the separation between the orbiter and the lander, that at this point enters hypersonic flight. The navigation goal in this phase was to converge to an accurate estimation of the altitude prior to reach 6000 m, where the spacecraft velocity was around 250 m/s (corresponding to a Mach number $M \approx 1.2$) and the main parachute opened. This was a 16.2 m diameter disk-gap-band parachute, made of Dacron and weighting 50 kg. It was deployed with a mortar that caused a transient variation in angular rates to be taken into account not to lose the altitude correct estimation. During the parachute descent the payload, standing at a distance of 30 m from the aerodecelerator, performed a roll manoeuvre intended to find the best orientation for the scientific operations after landing. The parachute was finally released at an altitude

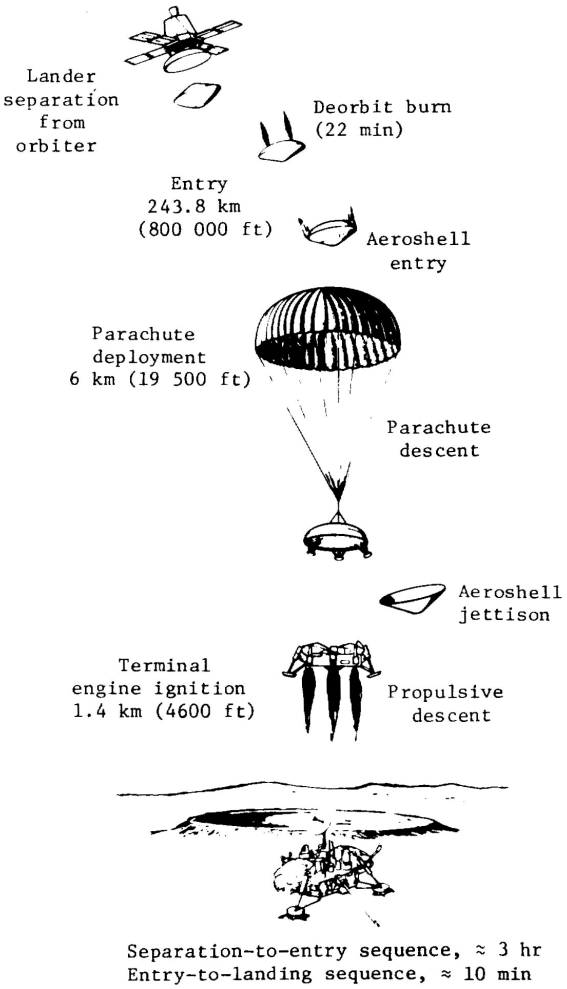

Figure 2.1: Viking mission entry, descent and landing sequence [Holmberg et al., 1980].

of 1400 m and a velocity of 54 m/s. At this moment the terminal descent engines were ignited for the final deceleration to achieve a soft touchdown.

More detailed information about Viking lander system design can be found in Ball et al. [2007], while an accurate description of the EDL operations, whose architecture represents the reference for all the subsequent Mars landing missions, is included in Holmberg et al. [1980].

After this first successful landing NASA decreased the budget dedicated to Mars exploration to focus on the Space Shuttle program. Mars Pathfinder (MPF) was the second Mars landing mission by NASA and was launched in 1996, about 20 years after Viking. The purpose of the 584 kg (wet mass) lander was to take measurements in the Ares Vallis, a particularly rocky area on the red planet. The parachute was similar to the one used for Viking but had a wider band for increased stability and, since it could resist to a dynamic pressure up to 703 N/m^2, was opened at higher altitude and velocity, respectively 9.4 km and 400 m/s according to the mission reconstruction by Braun et al. [1997], about 80 s prior to landing. During the descent phase the lander was lowered and distanced from the backshell by means of a 20 m bridle, so that the touchdown subsystem, an airbag, had enough space for inflation. At a velocity of 65 m/s the engines on the backshell were ignited to provide further deceleration and the payload (lander+airbags) was released. The parachute was dragged away by the residual thrust of the backshell engines[1]. The interested reader is referred to Spencer and Braun [1996] and Braun et al. [1997] for in depth data about the mission. An interesting aspect of the MPF vehicle is that, for the terminal part of its parachute descent, it was characterized by a three body configuration, depicted in Figure 2.2, consisting of the parachute, providing drag force, the backshell, that produces thrust upwards, and the payload, whose weight had to be balanced.

[1]The EDL sequence for MPF has been reconstructed according to *Mars Pathfinder, Entry,Descent and Landing*, accessible at http://mars.nasa.gov/MPF/mpf/edl/edl1.html. Last accessed: 13/01/2018

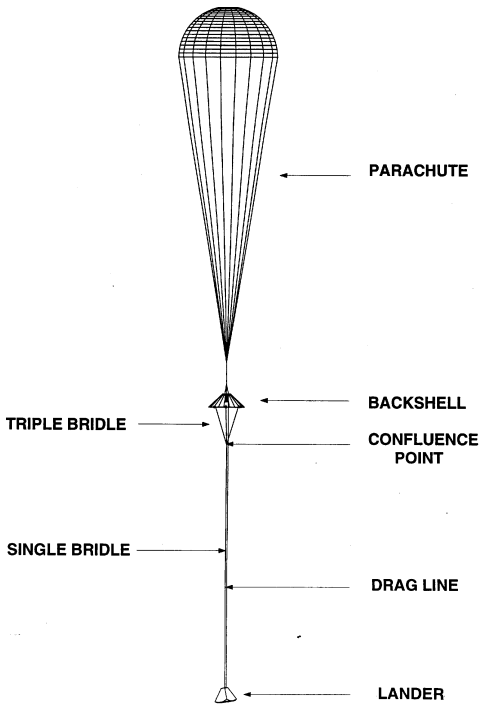

Figure 2.2: Mars Pathfinder terminal descent configuration [Spencer et al., 1999].

An analogous EDL sequence, reconstructed in Desai and Knocke [2004], as well as the 3-body chain-like configuration and the touchdown airbag system of MPF were successfully employed also in 2004 to land the rovers Spirit and Opportunity, both part of the Mars Exploration Rover (MER) program. According to Witkowski et al. [2005], in that period a dust storm in the predicted target area on Mars had caused the air density to increase so that the dynamic pressure at the deployment of the main parachute was significantly higher with respect to all previous missions. Nevertheless, the parachute had been further reinforced since Mars Pathfinder and could bear a dynamic pressure at deployment of 900 N/m^2, as was shown by post launch tests[2]. The absence of failures was an additional proof that the Viking derived parachute design and mission architecture were absolutely reliable, reasons why actual Mars landing missions still refer to it.

Until the first years of the new millennium, the main purpose of Mars landing missions had been to acquire generic scientific data about the planet. Viking, MPF and MER missions were characterized by a landing accuracy in the order of 100 km, that is enough if the interest area is large. In the new century, however, the scientific community directed its attention towards very specific features of the planet and to the next step in space exploration, the first man on Mars. These objectives require, amongst others, the capability to precisely deliver a cargo and, especially, to land close to a previously landed asset or within a very tiny area. For these applications a landing accuracy in the order of 10-100 m, namely a *pinpoint landing accuracy*, is needed.

As will be explained in more detail in Section 2.2 the size of the final landing ellipse is determined by many errors sources. Up to the present moment the better landing accuracy has been achieved by Mars Science Laboratory mission. This mission, whose EDL sequence details are available from Striepe et al. [2006], Karlgaard et al. [2012] and Cruz et al. [2014], represented an evolution with respect to all previous NASA missions. The MSL spacecraft, in fact, was equipped with a GNC system capable of counteracting the landing site dispersions, mainly variations in the density of the upper atmosphere and displacements in the initial entry conditions, affecting the delivery accuracy of this hypersonic entry. Thanks to this approach the Curiosity rover was landed in 2012 with an accuracy in the order of 10 km, paving the way for future precision landing missions[3].

In these years, also the younger European space program dedicated some effort to Mars exploration. The first European mission to Mars, Mars Express, was launched in 2003 within the same launch window as MER. The mission, whose limited budget was mainly provided by the British Government and ESA, included an orbiter and a small lander, Beagle 2. The capsule design for this lander was derived from the previously flown Cassini/Huygens mission. At the end of the hypersonic phase a disk-gap-band pilot parachute was fired us-

[2] Mars Exploration Rover mission overview is accessible at http://mars.nasa.gov/mer/home/.Last accessed 13/01/2018.
[3] Further data about Mars Science Laboratory mission is accessible at http://mars.nasa.gov/msl/. Last accessed 13/01/2018.

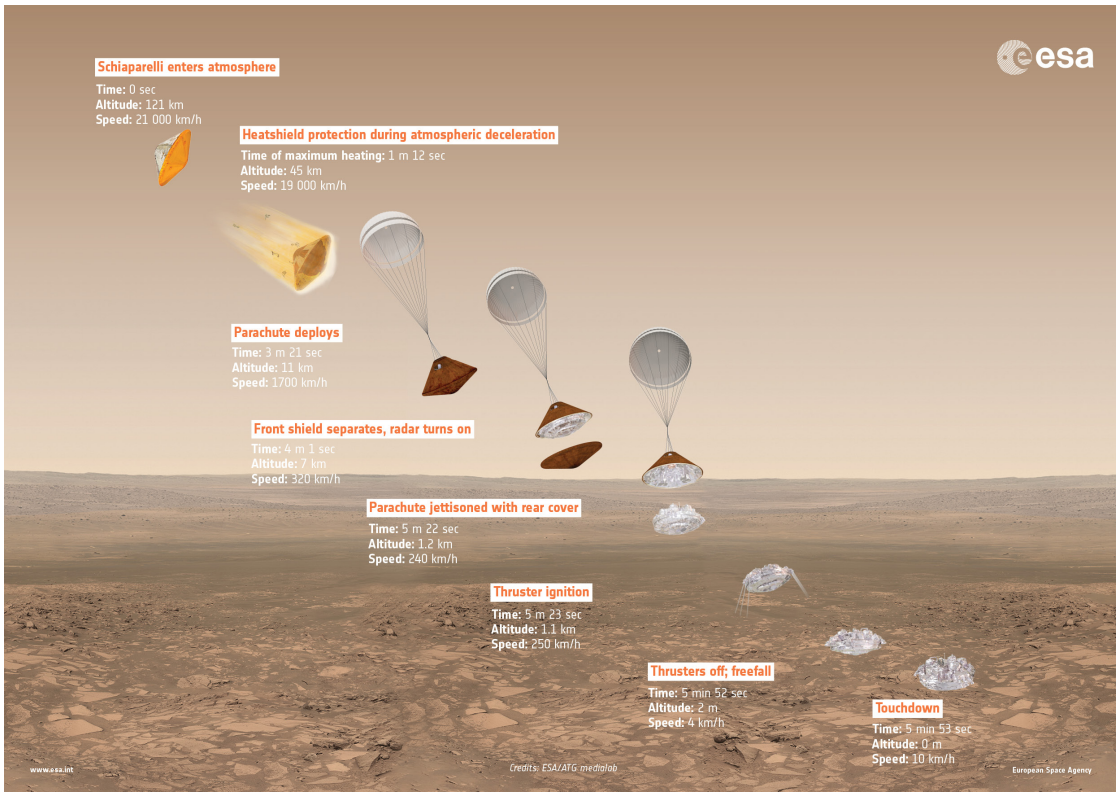

Figure 2.3: Schiaparelli entry, descent and landing sequence. Image credit: ESA

ing a mortar to stabilize and reduce velocity from $M \approx 1.5$ to subsonic. At $M \approx 0.6$ the main ringsail parachute, whose design is explained in Northey [2003], was deployed to provide maximum deceleration. Thanks to the small dimensions of the lander, the kinetic energy at the end of the parachute phase was low, so that an airbag system was enough for absorbing it. However, the communications with the Beagle 2 lander were lost just after touchdown, together with a lot of significant data. Still, the know-how acquired by ESA engineers during the mission design phase has been fundamental for the coming projects and strongly influenced the development of the following Schiaparelli lander.

ExoMars is an ESA/ROSCOSMOS program for the exploration of Mars. The first Exomars mission was launched in 2016 with the purpose to study some geological and biological features of Mars. Beside this, the spacecraft was equipped with the lander Schiaparelli, whose objective was to serve as a technology demonstrator for analysing several aspects of a Mars surface mission, prior to the launch of a second Mars EDL mission around 2020. The Schiaparelli mission layout is described by Bayle et al. [2016]. The parachute system to decelerate this vehicle during the descent phase was designed to be deployed in supersonic conditions. It could stand a maximum dynamic pressure of 910 N/m^2 and mach number of 2.1. The deployment conditions were met after the hypersonic phase when the velocity was around 500 m/s at approximately 7000 m over the predicted landing site, the Meridiani planum. When the drag acceleration corresponding to this interface was sensed, the pilot chute was fired by a mortar. This was a 12 m diameter disk-gap-band parachute, featuring 36 gores and a porosity of 22.4%. According to Lingard et al. [2009], the main aerodecelerator, deployed by the pilot, was instead a 20° conical ringslot parachute with a diameter of 25.5 m and 20% porosity, flying 28.5 m behind the probe. The pilot chute drag coefficient C_D was around 0.6, while the main had 0.53. In addition to this, after the deployment sequence, taking up to 3 s, the 50 kg heat-shield had to be separated and the lander, characterized by a high C_D, was uncovered. The initial driving requirement for this subsystem was that it was supposed to reduce the velocity of the 450 kg lander to 75 m/s when the altitude over the ellipsoid reached 4000 m.

Unfortunately, also Schiaparelli was lost during the EDL operations in 2016. Nielsen [2016] states that this was due to a combination of events including a flaw in the flight software and a problem in merging the data coming from different sensors. Up to now ESA has not been able to successfully land on Mars, but precision landing was also not a main concern for Beagle 2 and Schiaparelli, whose landing ellipse size was still in the order of 100 km.

2.2. THE LANDING ACCURACY PROBLEM

According to Brand et al. [2004], Mars landing missions can be divided into 4 classes depending on their objective and performance. Missions like Viking, Mars Pathfinder and ExoMars, whose EDL system key requirement was the capability to land a non-massive payload softly on the Red Planet, represent the first class of Mars landing missions. Their landing accuracy requirements were loose, in the order of 100 km. Mars Exploration Rover missions served to further prove that the Viking-derived mission architecture was robust. From that moment on the NASA Mars Exploration Program invested a lot of effort in GNC technologies for precise landing. Mars Science Laboratory was initially designed to achieve a 25×20 km landing ellipse, with the major axis oriented in the approach direction. According to Mendeck and Craig McGrew [2014], the final confidence landing area for the 900 kg Curiosity rover, also considering the event of strong wind, was a 19.1×6.9 km ellipse in the Gale Crater region. This was the first second class Mars landing mission and represents the current state of the art for Mars EDL technology. The third and fourth class missions are characterized, respectively, by the achievement of pinpoint landing accuracy and the capability to land the first man on Mars. In this respect, Mars Science Laboratory can be considered as a starting point for the development of the technologies needed for future missions and will be used in this section as a reference to understand how the landing site dispersion accumulates during the EDL mission phases.

Mars Science Laboratory was launched in October 2011 from Cape Canaveral, Florida, on board an Atlas V-541 rocket. After an 8 months interplanetary cruise it arrived in the Martian system at the beginning of August 2012. The EDL sequence was initiated on the 6^{th} of that month, when the lander, after separation from the Centaur cruise stage, was placed on a Mars reentry orbit.

The hypersonic entry phase started when the vehicle intersected the upper atmosphere boundary, sensed by means of the IMU that integrates acceleration starting several hours before entry operations. At this point a landing site dispersion had already grown during the cruise due to navigation errors in this phase, so that the atmospheric entry position and velocity were affected by a significant uncertainty. MSL was the first Mars landing mission that implemented a guidance and control system for the entry phase. Its objective was to get rid of delivery uncertainties at atmospheric entry, caused by manoeuvre execution errors and orbit determination uncertainties during the interplanetary trajectory, as well as uncertainties caused by density anomalies in the atmosphere and errors in the definition of the aerodynamic coefficients. The bank-angle control authority to compensate for these uncertainties was guaranteed by the capability to change the position of the centre of mass of the capsule by means of auxiliary mass ejections. After a *prebank phase*, where the bank angle was ground-commanded, the entry guidance algorithm started to work autonomously. The bank angle magnitude was modified to minimize predicted downrange error at parachute deployment and bank reversals were executed to handle crossrange error. After this *range control phase*, during which both peak heating and peak loading occurred, the guidance algorithm was set to maximize the parachute deploy altitude and minimize residual crossrange error. The *heading alignment phase* ended when the parachute deployment sequence was initiated, at approximately an altitude of 10 km.

To successfully deploy the parachute it was requested that the altitude was higher than 6 km, the Mach number within 1.1 and 2.3 and the dynamic pressure lower than 750 Pa. The design goal for the entry guidance and control system consisted of meeting these conditions within 10 km from the nominal parachute deployment position. Indeed, despite the implementation of a guidance system for the hypersonic entry, the position-velocity knowledge error at atmospheric entry caused by cruise navigation uncertainties, used to grow during the hypersonic phase, this being mainly due to the growth of the IMU integration error. As a result both the altitude and horizontal position uncertainties at deployment were in the order of ≈3 km (3σ).

In addition to navigation uncertainties, during the parachute phase the vehicle is subjected to the disturbances caused by the atmosphere of Mars, in particular winds. The wind drift is indeed the dominant source of uncertainty between the parachute deployment and the terminal descent thrusters ignition. It eventually causes the vehicle to drift up to a few km away from the reference trajectory, thus significantly contributing to the final landing error.

The parachute descent phase ends when the terminal descent thrusters are ignited, at an altitude of ≈1 km and a speed lower than 100 m/s. The purpose of this last phase is to decelerate the payload to achieve a soft touchdown. For an unguided parachute phase, following an MSL-like guided hypersonic entry, the delivery uncertainty at engine ignition can be seen as the sum of the uncertainty at parachute deployment due to navigation errors that accumulates during cruise, entry and descent phases and uncertainty caused by wind drift. According to Baker et al. [2014], the terminal descent system of MSL, that can rely on much more accurate navigation units with respect to those available for previous mission phases, ensures a control authority to correct for up to 50 m altitude error and to counteract the dispersions that affect this phase. Also, thanks to hazard

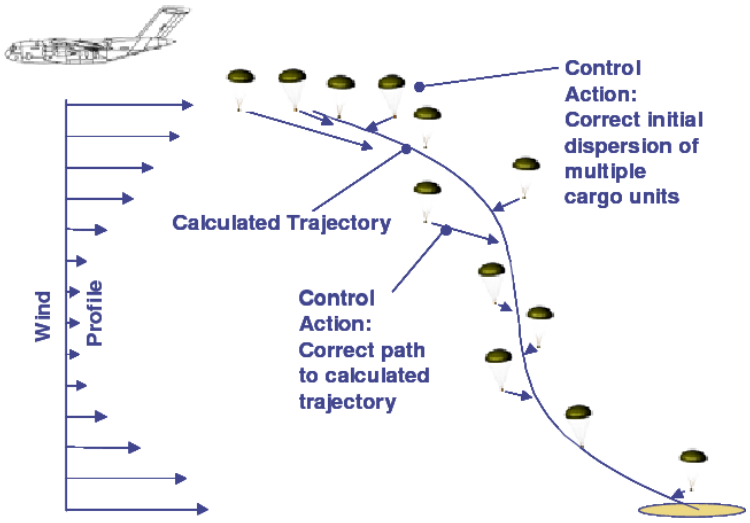

Figure 2.4: AGAS 2000 concept of operations [Jorgensen and Hickey, 2005].

avoidance system improvement, a small amount of additional control authority over the horizontal position could be guaranteed. It is clear, however, that the terminal descent GNC system cannot significantly reduce the landing inaccuracy that has been accumulated up to this point.

After the development of a GNC system for the hypersonic entry phase on the MSL spacecraft, the only EDL phase that remains unguided is the parachute deceleration. Considering these, a guidance and control system that can contrast wind disturbance during this phase and eventually reduce the overall position error at terminal descent thrusters ignition, could represent an efficient solution for improving the final landing accuracy on Mars.

2.3. GUIDED DESCENT CONCEPTS

Pinpoint landing accuracy is not exclusively a space-related requirement. In the military field such a capability is fundamental, for example, to deliver supplies to surrounded troops or to land provisions within a small area. This is why military engineers, from the US army in particular, started to study concepts for a guided descent long before this topic became interesting for EDL engineers.

Nowadays paratroopers use the parafoil to accurately land on a target. By djusting the length of the risers to modify the shape of the wing, the airman is able to control the direction and magnitude of the aerodynamic forces. One such example is the DRAGONFLY concept, introduced in Benney et al. [2005] that exploits a guidance logic as well as actuators and CPU to autonomously control the length of the risers and, in turn, the parafoil, taking into account the position of the landing site and the descent conditions. According to Hattis et al. [2000], the Airborne Guidance Unit (AGU), containing sensors, a computer and actuators, using Global Positioning System (GPS) and IMU measurements, guides the parafoil from the deployment altitude to landing within 100 m from the target and can be adapted for several mission scenarios, always ensuring good performance. Clearly, many other autonomous systems have been developed and extensively tested until now, but all of them rely on the same working principle and are pretty similar.

Despite several advantages that the parafoil has when compared to the parachute, it is less robust and must always be guided somehow. In addition to this, when landing with a parafoil a residual horizontal velocity, even in absence of wind, has to be taken into account. This can be unfavourable for some applications. Finally, not only a parafoil dissipates energy less efficiently with respect to a parachute, but also it costs more, resists a lower dynamic pressure at deployment and can suffer from inflation problems. Finally, the deceleration requirements for a Mars EDL mission coupled with the low atmosphere density would result in a parafoil with prohibitive dimensions. The solution of using a parafoil to control the descent on Mars is thus discarded.

Parachute systems are in general more appropriate if the objective is to decelerate a high speed payload. They maintain the first place in the field of military and space deliveries and are still object of research and optimisation. The Affordable Guided Airdrop System 2000 (AGAS 2000) is a US military project to achieve high accuracy payload delivery using a simple and affordable system. The AGAS 2000 system, whose concept of operations in depicted in Figure 2.4, consists of a flat circular cargo parachute and a GNC unit. This unit includes

actuators that directly control the length of the risers and is analogous to the one used for the previously cited DRAGONFLY. As suggested by Dellicker et al. [2003] Differently from the parafoil, a circular parachute does not have a fixed heading axis, so that, if properly inclined, can glide in every direction. However, while a parafoil can be released from an airplane within a very wide area around the target, the AGAS 2000 system is designed to only counteract the dispersions caused by the errors in wind estimations and in the effective aircraft release position. In fact, the Calculated Air Release Point (CARP), together with the nominal trajectory, are computed according to the pre-flight wind predictions. The guidance logic receives in input the GPS estimated position and controls the parachute inclination, i.e., the drag force vector, with the objective to remain within 30 m from the nominal trajectory. The low control authority that AGAS 2000 guarantees, implies that the final achievable landing accuracy strongly depends on the accuracy at release and, most of all, on the accuracy of wind estimates. This is why, according to the data of Jorgensen and Hickey [2005], the Circular Error Probable (CEP), that is a sort of landing ellipse, increases from 211 m to 38 m when a wind probe in the landing site area is available.

This parachute descent mission scenario on Mars, described earlier, is similar to what AGAS 2000 is supposed to do in an Earth environment. Mars Guided Parachute (MGP) program aims at proving that the technology developed for AGAS 2000 can successfully be adapted to operate on Mars for improving landing accuracy. The system, adapted for Mars landing, uses a ringsail parachute because a disk-gap-band one would not be capable of gliding. Also, the ringsail has already been used in Beagle 2 mission. According to the paper of McKinney and Lowry [2009], simulations and tests in a Mars relevant environment (low density atmosphere) proved this configuration is performing, even if a more accurate development is needed.

The MGP program represents a possible solution for realizing a guidance system for the parachute descent on Mars with the aim reducing the size of the landing ellipse. The control force for this concept is the aerodynamic force generated by the parachute, whose vertical and horizontal components are adjusted to control, respectively, the vertical and horizontal motion of the vehicle. So, for example, if local wind has a vertical component pointing upwards that has to be compensated for, the canopy has to be inclined to reduce the vertical component of the aerodynamic force, but, in the meanwhile, a horizontal component is generated and the parachute glides even in case horizontal wind is absent. Furthermore, the actuation based on the control of the length of the risers has never flown in a space environment and the responsiveness could be too low if the control has to be realized in a ≈ 60 s parachute descent phase. Also, as for AGAS 2000, MGP guarantees a limited amount of control authority that is enough only for compensating the wind drift effect.

At this point, one could think to implement a guidance and control system for parachute descent based on propulsive actuators, i.e., thrusters. This is a technology that has already been extensively used for Mars landing and could ensure a very high level of reliability and performance. In particular, the idea on which the present research is based is to evaluate whether the use of thrusters installed on the backshell of the vehicle can be used efficiently for guidance and control purposes during the parachute descent.

2.4. DYNAMIC STABILITY & MODELLING

A typical descent spacecraft consists of a parachute and payload connected by means of an elastic riser. Eventually, as Figure 2.2 shows for the MPF vehicle, a backshell can be present between them. In general, this configuration is rotationally symmetric around the axis that passes through the centres of mass of these elements. The hinges between the risers and the parachute, backshell and payload bodies can be considered as spherical connections. They constrain the horizontal and vertical relative motion of the rigid elements but allow their relative rotation. A parachute-payload system is thus non-rigid and its stability properties, that depend on many parameters including the parachute size and type, the mass of the payload and the distances between these element, are fundamental for the mission success. In fact, if the system oscillates too much, then it is possible, for example, that a certain feature on the surface of Mars exits from the field of view of an optical sensor or that a hardware component gets damaged due too large horizontal accelerations. Also, the terminal descent thrusters ignition requires that the vehicle is stable.

The objective of the parachute descent flight then is not only to dissipate energy, but also to stabilize the vehicle before the landing phase. In particular, it is desirable that the descent vehicle can damp dangerous oscillations due to the parachute mortar firing and inflation, that it can withstand the impact of atmospheric perturbations such as gusts and turbulences and that it can rapidly converge to the equilibrium vertical flight condition. In addition to this, the dynamic behaviour of the vehicle will be heavily influenced by the descent guidance system that will later be developed and integrated on it. To modify the spacecraft design for adapting it to the presence of this new subsystem, first the influence of the system parameters on its stability properties need to be investigated in detail.

Considering these, the analysis of the stability behaviour of parachute-payload systems will represent one of the main topics of the present project, together with the development and evaluation of the guided descent concept. For these purposes, however, a model that can simulate the dynamics of the system is needed. This model will influence significantly the results of the study and thus its choice has to be reasoned.

There exist 2 classical ways to determine the EOM that describe a dynamical system. These are the Newton-mechanics and Lagrangian-mechanics based methods. One of the main differences between these approaches lies in the way the constraint forces are considered and in how the structure of the system is mathematically modelled. The Newton-based approach, for example, provides a great insight into the EOM but it requires that all the constraint forces, that are present in case of non-rigid systems, are determined explicitly. On the other hand, by applying Lagrange mechanics one does not need to care about the constraint forces because they are already included in the EOM. In this case, in fact, the EOM with respect to any set of generalized coordinates can be analytically derived from the expression of an energy-like function associated to the system, the Lagrangian. However, determining the Lagrangian can sometimes be cumbersome. Also, the Newton mechanics-based approach, in case of systems with simple geometry, is much more straightforward with respect to the Lagrange one and it represents the best choice for the analysis of the dynamics of rigid body systems. Some pioneering studies focusing on the stability of parachute-payload systems, such as Helmut and Lawrence Jr. [1965], Heinrich and Haak [1971] and Hume [1973], exploited models based on classical mechanics.

When higher fidelity is required and the number of interconnected bodies and Degrees Of Freedom (DOF) of the system increase, then the task of determining the EOM using either Newton or Lagrange methods increases accordingly. Because of this, in the last decades new procedures for handling the dynamics of complex mechanical systems have been developed. By applying a multibody formalism, the user is no more concerned with the constraint forces, as with the Newton method, nor with the definition of an expression for the energy associated to the system, as happens when dealing with Lagrange mechanics. Generally, he only has to deal with matrices that define the configuration of the multibody and force vectors. The EOM for the system are obtained automatically by manipulating these elements. Some examples of parachute-payload multibody models characterized by a large number of DOF include Ibrahim and Engdahl [1974], Fallon [1991], Doherr and Schilling [1991] and Abdulkadir [2011]. Other models, specifically developed for analyzing the dynamics of parafoil-payload systems, similar to that of parachute-payload ones, are instead Vishnyak [1993], Müller et al. [2003] and Mooij et al. [2003].

A model derived using a multibody approach describing the motion of a parachute-payload spacecraft is not necessarily better than a rigid body one, determined for example using Newton. In fact, the former normally requires more time for being developed and, also, if the system has more DOF then the state vector describing its trajectory is larger and its dynamics more articulated. Additionally, the physical interpretation of the EOM is not straightforward, this being a fundamental requirement if the system has to be studied analytically. On the other hand, the multibody model can simulate the relative motion of the elements of the non-rigid spacecraft, while rigid body models can only reproduce its pendulum-like oscillations.

Considering the purpose of the present study, both a rigid body and a multibody model are needed. The first will indeed be used for deriving analytical results and have a better insight into the physics of the problem and on the parameters that most characterize the dynamics of the spacecraft. This model will be realized by applying the Newton approach for which an accurate investigation of the equilibrium of the forces and moments acting on the body is required.

For the multibody model, instead, two options seem to be appriopriate. In fact, the C++ code implementing the already cited model of Abdulkadir [2011], based on the multibody formalism of Wittenburg [2008], has been recovered and updated as part of the present project. It is robust, versatile and computationally efficient but offers poor insight into the dynamics of the problem. A second option would consist instead of building a multibody parachute-payload model starting from the idea of Neustadt et al. [1967]. In this publication the objective was to determine the optimal anchorage point between the parachute riser and the Apollo capsule. To study how these bodies influence each other, the riser was modelled as a spring. In particular, the parachute and capsule move independently under the effect of the respective forces and moments, the only influence between them being the elastic force caused by the connecting riser. The lengthening of the riser is due to the two body elements moving apart. This concept could be developed into a more extensive parachute-payload system. In the resulting model, the EOM of each rigid element would be determined using Newton and no constraint forces should be taken into account. This approach would allow to derive a model that can simulate the relative motion between the elements of the spacecraft in a short amount of time with respect to other multibody methodologies. Also, the resulting EOM would remain simple, this being an additional advantage of this approach. In Section 3.3 these two options will be further discussed, compared and investigated.

2.5. MISSION AND SYSTEM REQUIREMENTS

During this research project we will need a nominal mission and vehicle. This information will be used to build the model, to validate it and as a reference for the analysis.

The reference mission is a classical Mars EDL mission consisting of an entry phase, a parachute phase and a powered terminal descent phase, at the end of which the lander touches down on the Red Planet. Thanks to its proven robustness, this mission layout, with minor variations in the parachute deployment altitude and touchdown and entry strategies, since Viking mission represents the standard not only for NASA but also for every other Mars landing mission. In particular, we focus our attention on the parachute descent phase. For the MSL mission that, as explained, represents the state of art of Mars EDL missions, the parachute deployment sequence was initiated at a target altitude of 10 km, when the velocity is around 450 m/s. The constraints for a successful parachute inflation requested that the dynamic pressure was lower than 750 Pa and the Mach number between 1.1 and 2.3. After the inflation of the main chute, the drag force stabilized the system and decelerates until it reaches the vertical steady-state flight at around 6000-5000 m, depending on the atmospheric conditions the spacecraft faces once on Mars. From this point the only purpose of the parachute is to decelerate the vehicle until it reaches a vertical velocity around than 70-60 m/s at the target altitude of 1000 m, where the terminal descent thrusters ignite for ensuring a soft and safe touchdown. The total descent, from deployment to engine ignition, lasts around 100 s while the steady-state flight phase starts 70 s before target altitude is reached. These parameters, derived from the detailed MSL mission reconstruction of Mendeck and Craig McGrew [2014], will be used as a reference mission. The nominal flight condition is assumed to be a vertical descent flight in absence of winds starting at 6000 m with a velocity of 100 m/s (this value has been verified to be appropriate after several simulations with the reference vehicle). Also, the spacecraft is assumed to be oriented vertically for this nominal flight condition.

With respect to the reference vehicle, however, the MPF spacecraft is chosen. The EDL mission sequence for this mission, as already discussed earlier, was characterized by a powered descent phase in which, differently from MSL, the parachute was still in use. Its aim in this case was not only to reduce vertical speed, but also to stabilize the vehicle that was equipped with backshell thrusters pointing downwards, these being the main source of deceleration in this flight phase. The three-body architecture of this vehicle, depicted in Figure 2.2, is appropriate for housing the thrusters that in our case we want to use for position control at higher altitudes with respect to MPF treminal descent. Also, we decide to slightly modify the vehicle dimensions by assuming a shorter riser between the backshell and the payload. For our MPF vehicle we assume 5 m instead of $\approx$ 20 m. In fact, the reasons for having such a long riser were imputable to the need of avoiding impingement of the thrusters plume with the payload and of limiting the oscillation amplitude due to gusts impacting on the vehicle at low altitudes. On the other hand, a shorter riser can result in a system that responds more quickly to commanded lateral thrust. The length of the riser, however, is one of those parameters that significantly influence the system stability and the performance of the guided descent concept and thus the effect on its dynamics will be analysed in more detail in Chapter 8. The other relevant relevant vehicle parameters and properties, taken from Abdulkadir [2011] that also uses MPF as reference vehicle, are given in detail in Section 3.2.3.

Table 2.1 contains the mission requirements that determine how the present study will be approached. In addition to these, we also need the system requirements, reported in Table 2.2, defining the desired characteristics for the guided parachute-payload descent spacecraft. These requirements, that summarize the discussion of the present chapter, will yield an outline for guiding the models development and the analyses of Chapters 6 to 8.

A final remark has to be made with respect to the navigation and control subsystems. In particular, navigation heavily influences the performance of the guidance system because it receives in input the estimated state. In other words, when analysing the characteristics of the concept, we need to take into account this effect that, currently, represents the largest obstacle to climb if pinpoint landing accuracy on Mars has to be achieved. This is why Section 8.2.3 discusses this theme in more detail. Nevertheless, the present research project will focus more at determining if powered position control during the Mars parachute phase is efficient from the point of view of dynamic stability and if it is performing with respect to consumption and amount of error that can be compensated. The problem of having a navigation system that can make controlled descent possible, despite discussed, is somehow independent with respect to the present work and represents a later step in the development of the technology.

Table 2.1: Mars parachute descent guidance and control MISSION REQUIREMENTS.

Req. ID	Content
MR.1	A guidance system for the parachute descent flight on Mars shall be developed.
MR.2	A rigid body model of the reference vehicle shall be designed.
Rationale:	this model will be used for deriving analytical results with respect to the dynamic properties of parachute-payload systems.
MR.3	A multibody model of the reference vehicle shall be designed.
Rationale:	this model will be used for simulating the descent flight of the parachute-payload system.
MR.4	The analysis shall be performed using the MPF vehicle as reference.
MR.5	The environment of Mars between the altitudes of 10000 and 1000 m over its surface shall be modelled.
Rationale:	this is the altitude band where the parachute descent flight takes place.
MR.6	The dynamic response of the system to gusts and atmospheric turbulence shall be analysed.
Rationale:	gusts and turbulence are typical perturbations that are encountered in the planetary boundary layer of Mars. In particular the gust resembles a impulsive input and can be used to evaluate the rigidity of the system and its how well it damps oscillations. Turbulence instead continuously excites the oscillations of the system and can be used to determine which input frequencies are more dangerous.
Specification:	the characteristics of the gusts and turbulence for the analysis are given respectively in Section 4.1.2 and 4.1.3.
MR.7	The performance of the guidance system shall be analysed in both nominal and perturbed conditions.
Specification:	for perturbed conditions it is intended the case in which the vehicle is subjected to winds, gusts and turbulence during the descent flight.
MR.8	The influence of navigation error on the performance of the guidance system shall be analysed.

Table 2.2: Mars parachute descent guidance and control SYSTEM REQUIREMENTS.

Req. ID	Content
SR.1	The guidance system shall generate commands for the thrusters installed on the backshell of the reference vehicle.
SR.2	The guidance system for the Mars parachute descent flight shall control the position and velocity of the spacecraft.
Rationale:	these state variables are the most important to control for improving landing accuracy. In fact, the final landing error is indeed a position error and velocity errors directly influence it.
Specification:	This topic is discussed in more detail in Section 2.3.
SR.3	The mass, geometric, and aerodynamic properties of the MPF reference vehicle shall be taken from Abdulkadir [2011].
SR.4	The spacecraft is assumed to be equipped with an optical navigation system.
Rationale:	optical systems for Mars EDL navigation, as discussed in Section 8.2.3, are now object of research and could be adapted for being used also during the parachute descent phase.
Specification:	the characteristics of the navigation system shall refer to Johnson et al. [2015].
SR.5	The initial condition and constraints for the descent flight simulation shall refer to the MSL mission reconstruction of Mendeck and Craig McGrew [2014].
Specification:	the initial conditions for the simulations are not fixed. Sometimes they are varied around the reference values for highlighting certain aspects of the dynamics of the system.

3

FLIGHT MECHANICS

In Section 2.4 the need for models that can simulate the dynamics of the reference vehicle and are appropriate with respect to the requirements of the following analysis phase has been addressed. Before to develop them, however, Section 3.1 introduces the theory that forms the basis of flight mechanics studies. This includes Newton's laws, reference frame definitions and frame transformations, coordinate systems and, last but not least, the introduction of the general formulation of the EOM for a moving vehicle. This background represents the starting point for the definition, in Section 3.2, of a rigid body parachute-payload model that will serve for obtaining analytical preliminary information about dynamics of the spacecraft. Section 3.3, instead, is dedicated to the development of a multibody model that, amongst others, can reproduce the relative motion of the parachute, backshell and payload elements and can be used for higher fidelity response simulations.

3.1. MATHEMATICAL & PHYSICAL BACKGROUND

Mechanics is the discipline that studies the equilibrium of bodies subjected to a number of forces and moments acting on and around its COM. This discipline can be divided in three different branches. These are *statics*, that studies the equilibrium of the forces acting an a system at rest, *dynamics*, that studies the variations of the forces that act on a system causing its motion and yields information about the resulting linear and angular accelerations of the body itself and *kinematics*, that studies the motion of the body by simply analysing how the velocities caused by the forces the body is subjected to result in changes of its position and attitude.

The *Philosophiae Naturalis Principia Mathematica* written in the second half of the 17^{th} century by Sir Isaac Newton represents the foundation of all these three branches. In particular, the three Newton's laws of motion are at the basis of any other concept and theory related to the field of mechanics developed in the following centuries. These are [Wie, 2008]:

1. *First law:* A particle remains in its state of rest or uniform, straight-line motion unless it is acted upon by forces to change that state; this is the law of inertia. (Note that the term *particle* is a mathematical abstraction of a relatively small body and it is used interchangeably with the term *point mass*.).

2. *Second law:* The force acting on a particle equals the mass of the particle times its inertial acceleration. Mathematically this law is expressed as:

$$\mathbf{F} = m\mathbf{a} \tag{3.1}$$

   where $\mathbf{F}$ is the force acting on the particle, m is its constant mass and $\mathbf{a}$ its inertial acceleration.

3. *Third law:* For every applied force, there is an equal and opposite reaction force; this is the law of action and reaction.

The Newton's laws of motion are the starting point for determining the EOM of any dynamic system. Nevertheless, they only hold for an inertial reference frame. In flight dynamics applications, however, several non-inertial frames, described in 3.1.1 together with the topics of coordinates and frame transformations, are commonly used. To use the Newton's laws also is these cases it is necessary to add some corrective terms, the

apparent forces and moments, in the balance expressed by the EOM. This process is described in Section 3.1.2. In there, the problem of deriving the EOM for the the case of the parachute-payload descent vehicle will also be introduced. In particular, first an appropriate reference frame in which the EOM can be defined will be chosen, and second the forces and moments that dominate its motion will be discussed.

3.1.1. REFERENCE FRAMES & TRANSFORMATIONS

A reference frame consists of a set of three mutually orthogonal axes that intersect in the origin of the frame. For the purpose of studying the dynamics of a flying vehicle, many reference frames, either inertial or non-inertial, can be used. An inertial frame is fixed in space or translates with constant velocity, while non-inertial frames feature rotational and linear accelerations with respect to inertial ones. Some of the most used reference frames for flight dynamics purposes include [Mooij, 2015]:

- *Inertial planetocentric reference frame (I)*
  The origin of this frame coincides with the COM of the central body and the $X_I Y_I$-plane with its equatorial plane. The Z_I-axis corresponds to the rotational axis of the central body and points North while the X_I-axis the points the position of the reference meridian at time t_0. The Y_I-axis completes the right-handed system. For re-entry systems applications the motion of the rotational axis of the planet due to the gravitational influences of other bodies of the Solar System can be neglected.

- *Rotating planetocentric reference frame (R)*
  This frame corresponds to the I frame at time t_0 and after any complete rotation of the central body around its axis. Indeed, assuming no nutation and precession, the Z_R-axis frame always coincides with the Z_I-axis but the X_R-axis constantly points the reference meridian of the body and rotates with it. The Y_R-axis completes the right-handed system and also rotates with the central body.

- *Body reference frame (B)*
  The origin of this frame is fixed to the COM of the vehicle that is assumed to have a symmetry plane in longitudinal direction. This plane is the $X_B Z_B$-plane where the X_B-axis points in forward direction and the Z_B-axis points downwards. The Y_B-axis completes the right handed system.

- *Vertical reference frame (V)*
  The origin of this frame corresponds to the COM of the vehicle. The Z_V-axis points in radial direction towards the COM of the central body and the X_V-plane is perpendicular to it and points the northern hemisphere. The Y_V-axis completes the right-handed system. The $X_V Y_V$-plane perfectly coincides with the local horizontal plane when the central body is a sphere but in the real case, i.e., when the oblateness is considered, a small error is introduced.

- *Trajectory reference frame, airspeed based (TA)*
  The origin of this frame corresponds to the COM of the vehicle. The X_{TA}-axis points in the same direction as the velocity vector with respect to the atmosphere while the Z_{TA}-axis is perpendicular to X_{TA} and points downwards. The Y_{TA}-axis completes the right-handed system. An analogous frame (TG) can be defined also with respect to the groundspeed.

- *Aerodynamic reference frame, airspeed based (AA)*
  The origin of this frame corresponds to the COM of the vehicle. The X_{AA}-axis points in the same direction as the velocity vector with respect to the atmosphere while the Z_{AA}-axis that is perpendicular to X_{AA}, is collinear with the lift force vector (defined according to the airspeed velocity) but is opposite in direction. The Y_{AA}-axis completes the right-handed system. An analogous frame (AG) can be defined also with respect to the groundspeed. When the vehicle is not banking the TA-frame coincides with the AA-frame and the TG-frame coincides with the AG-frame.

- *Propulsion reference frame (P)*
  The origin of this frame corresponds to the COM of the vehicle. This frame is used when the thrust vector is identified using its magnitude and two direction angles defined with respect to the B-frame. The X_P-axis has the same direction as the thrust vector while Z_P- and Y_P-axis are obtained by rotating the B-frame around its Z_B- and Y_B-axis of an angle equal to the corresponding direction angles of the thrust vector.

The forces typically acting on a flying vehicle, characterized in Section 3.1.2, can have either a gravitational, aerodynamic or propulsive nature and normally they are not expressed with respect to the same reference

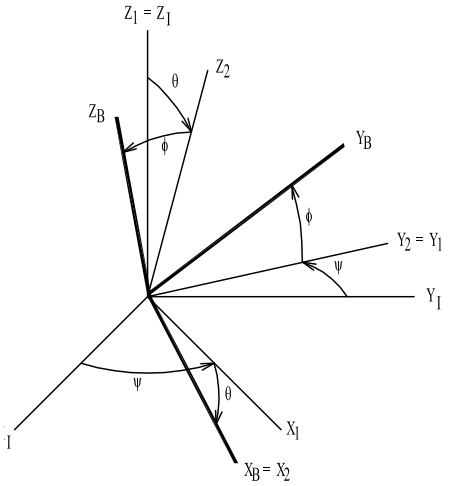

Figure 3.1: Classical angles θ, ϕ and ψ relating the body B-, and inertial planetocentric I-frames [Mooij, 2015].

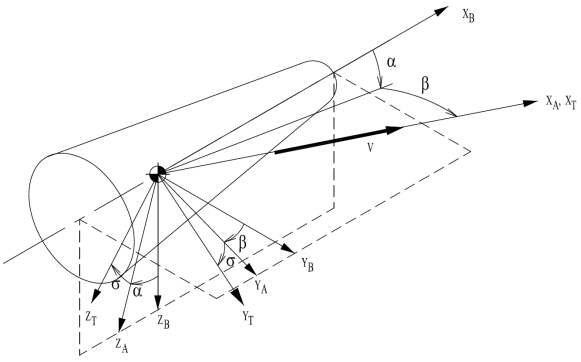

Figure 3.2: Aerodynamic angles α, β and σ relating the body B-, aerodynamic A- and trajectory T-frames (either airspeed or groundspeed based) [Mooij, 2015].

frame. The aerodynamic forces are identified in an aerodynamic reference frame, because their direction is always fixed with respect to the velocity of the vehicle relative to the atmosphere, while the gravity force is normally determined in the vertical reference frame and the thrust force in the body or propulsion reference frame. As a result, before to be included in the balance defined by the EOM describing the motion of the vehicle, all these vectors need to be expressed with respect to a common reference frame by means of frame transformations. Frame transformations are possible if the relative position and orientation of a frame with respect to another, namely the state and attitude of the vehicle, is known.

For identifying the spacecraft position and velocity several sets of variables can efficiently be adopted. Those relevant for our research are:

- *Cartesian components*: these components are normally used to determine the position and velocity of the vehicle with respect to the I or R frames. The position is identified by the elements x,y,z while the velocity is given by $\dot{x},\dot{y},\dot{z}$.

- *Spherical components*: this is also a set of six elements. The position of the vehicle with respect to the R-frame is identified by the distance from its origin R, the longitude τ ($0° \leq \tau < 360°$) measured positively towards the East direction starting from the reference meridian and the latitude δ ($-90° \leq \delta \leq 90°$) measured positive due north starting from the equator. The velocity, on the other hand, is identified using the groundspeed magnitude V_g, the flight-path angle γ_g and heading angle χ_g defined with respect to the groundspeed vector.

Analogously, the attitude of a vehicle can be determined using the sets:

- *Classical attitude angles*: these angles, namely the roll angle ϕ, the pitch angle θ and the yaw angle ψ, are used to determine the attitude of the vehicle with respect to the inertial frame or with respect to the local horizontal plane. When using these angles it is important to determine the sequence of rotations that realizes the transformation. For aerospace applications the most commonly used sequence is the 3-2-1, consisting of a yaw rotation about the $Z-$ axis followed by pitch and roll rotations around, respectively, the local $Y-$ and $X-$ axes.

- *Aerodynamic angles*: these angle, namely the angle of attack α ($-180° \leq \alpha < 180°$, $\alpha > 0$ for nose-up), the sideslip angle β ($-90° \leq \beta \leq 90°$, $\beta > 0$ for nose-left) and the bank angle σ ($-180° \leq \sigma < 180°$, $\sigma > 0$ for right bank), determine the attitude of the vehicle with respect to the groundspeed or airspeed vectors. The aerodynamic angles α, β and σ represent a set of Euler angles whose sequence has order 2-3-1. This set of angles is depicted in Figure 3.2.

Any frame transformation can be written as the sum of a translation and a rotation. To express the vector $\mathbf{v_A}$ in the **A** frame with respect to the **B** frame we write:

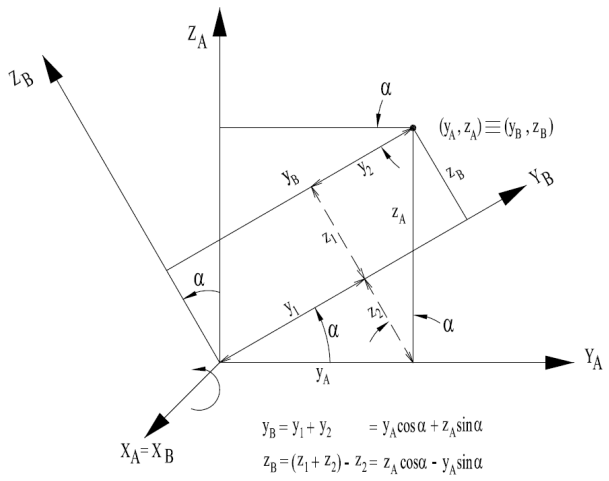

Figure 3.3: Reference frame transformation from **A** to **B** [Mooij, 2015].

$$\mathbf{v_B} = \mathbf{T} + \mathbf{C_{B,A}}\mathbf{v_A} \tag{3.2}$$

where **T** is the translation vector that goes from the origin of the **A** frame $\mathbf{O_A}$ to the origin of the **B** frame $\mathbf{O_B}$ and $\mathbf{C_{B,A}}$ is the rotation matrix from frame **A** to frame **B** given by [Mooij, 2015]:

$$\mathbf{C_{B,A}} = \begin{bmatrix} 1 & 0 & 0 \\ 0 & \cos\alpha & \sin\alpha \\ 0 & -\sin\alpha & \cos\alpha \end{bmatrix} \tag{3.3}$$

This orthonormal matrix, as suggested in Figure 3.3, can be derived by expressing the components of the vector $\mathbf{v_A}$, defined with respect to the axes of the **A** frame, with respect to the axes of the **B** frame. More generally, if identified with the notation $\mathbf{C}_1(\alpha)$, the matrix in Eq. (3.3) gives the counter-clockwise rotation of a frame around its X-axis of an angle α. Analogous expressions hold for the rotations around the Y- and Z- axes. We have respectively:

$$\mathbf{C}_2(\alpha) = \begin{bmatrix} \cos\alpha & 0 & -\sin\alpha \\ 0 & 1 & 0 \\ \sin\alpha & 0 & \cos\alpha \end{bmatrix} \tag{3.4}$$

$$\mathbf{C}_3(\alpha) = \begin{bmatrix} \cos\alpha & \sin\alpha & 0 \\ -\sin\alpha & \cos\alpha & 0 \\ 0 & 0 & 1 \end{bmatrix} \tag{3.5}$$

Also, a frame rotation can always be decomposed in a sequence of three rotations each around one of its independent axes. The resulting transformation matrix, that is still orthonormal, is found as the product of the three matrices $\mathbf{C}_1$, $\mathbf{C}_2$ and $\mathbf{C}_3$. Moreover, if $\mathbf{C_{B,A}}$ is the matrix transforming frame **A** into frame **B**, then the opposite transformation, thanks to the fact that rotation matrices are orthonormal, is given by the transpose:

$$\mathbf{C_{A,B}} = \mathbf{C_{B,A}^{-1}} = \mathbf{C_{B,A}^{T}} \tag{3.6}$$

According to this theoretical background about frame transformations, it is possible to define some standard relationships, collected in Table 3.1, between the reference frames presented above. The relations that are not directly reported can be obtained by combining those that are listed.

In cases when one is dealing with 2D vectors lying, then the rotation matrix can be reduced to size $[2 \times 2]$. In fact every 2D rotation can be described using a single angle and the row and column corresponding to the rotation axis (the one with only one term different from zero) is not needed any more. Also in this case the right hand rule determines the sign of the elements in the rotation matrix and the frame rotation direction can be counter-clockwise (as the one given by Eq. (3.3) or clockwise.

Table 3.1: Standard frame transformations [Mooij, 2015].

From	To	Transformation matrix	Involved variables
R	*I*	$\mathbf{C}_{I,R} = \mathbf{C}_3(-\omega_{cb}\,t)$	ω_{cb} = central body rotation rate t = time from epoch
V	*R*	$\mathbf{C}_{R,V} = \mathbf{C}_3(-\tau)\mathbf{C}_2(\frac{\pi}{2}+\delta)$	τ = planetocentric longitude δ = planetocentric latitude
W	*V*	$\mathbf{C}_{V,W} = \mathbf{C}_3(-\chi_w)\mathbf{C}_2(-\gamma_w)$	γ_w = flight path angle wrt wind vector χ_w = heading angle wrt wind vector
TG	*V*	$\mathbf{C}_{V,TG} = \mathbf{C}_3(-\chi_g)\mathbf{C}_2(-\gamma_g)$	γ_g = flight path angle wrt groundspeed vector χ_w = heading angle wrt groundspeed vector
TA	V	$\mathbf{C}_{V,TA} = \mathbf{C}_3(-\chi_a)\mathbf{C}_2(-\gamma_a)$	γ_a = flight path angle wrt airspeed vector χ_a = heading angle wrt airspeed vector
AA	*TA*	$\mathbf{C}_{TA,AA} = \mathbf{C}_1(\sigma_a)$	σ_a = bank angle wrt airspeed vector
B	AA	$\mathbf{C}_{AA,B} = \mathbf{C}_3(\beta_a)\mathbf{C}_2(-\alpha_a)$	β_a = sideslip angle wrt airspeed vector α_a = angle of attack wrt airspeed vector
B	*AG*	$\mathbf{C}_{AG,B} = \mathbf{C}_3(\beta_g)\mathbf{C}_2(-\alpha_g)$	β_g = sideslip angle wrt groundspeed vector α_g = angle of attack wrt groundspeed vector
B	*P*	$\mathbf{C}_{P,B} = \mathbf{C}_3(\psi_T)\mathbf{C}_2(\epsilon_T)$	ϵ_T = elevation angle of the thrust vector ψ_T = azimuth angle of the thrust vector

3.1.2. EQUATIONS OF MOTION & EXTERNAL FORCES

The EOM of a non-elastic body (6 DOF) are used to characterize the motion of and around its COM and directly derive from the application of the Newton's laws of motion and the Galileo Principle of Relativity to the dynamic system. In case these are defined with respect to a non-inertial reference frame then the terms for the relative forces have to be included in the balance. If the relativistic effects are neglected, this being possible because the characteristic velocity we are dealing with is much smaller than the speed of light, the translational EOM with respect to an arbitrary reference frame is:

$$\mathbf{F}_\mathrm{I} + \mathbf{F}_\mathrm{C} + \mathbf{F}_\mathrm{rel} = \widetilde{\mathbf{F}}_\mathrm{I} = m\frac{d^2\mathbf{r}_\mathrm{cm}}{dt^2} \tag{3.7}$$

For the rotational equilibrium a similar equation holds:

$$\mathbf{M}_\mathrm{cm} + \mathbf{M}_\mathrm{C} + \mathbf{M}_\mathrm{rel} = \widetilde{\mathbf{M}}_\mathrm{cm} = \int_m \tilde{\mathbf{r}} \times \left(\frac{d\boldsymbol{\omega}}{dt} \times \tilde{\mathbf{r}}\right) dm + \int_m \tilde{\mathbf{r}} \times [\boldsymbol{\omega} \times (\boldsymbol{\omega} \times \tilde{\mathbf{r}})]\, dm \tag{3.8}$$

In Eq. (3.7) and (3.7), $\mathbf{F}_\mathrm{I}$ and $\mathbf{M}_\mathrm{cm}$ are the total external force and moment with respect to COM of the body of mass m, and $\mathbf{F}_\mathrm{C}$, $\mathbf{F}_\mathrm{rel}$, $\mathbf{M}_\mathrm{C}$ and $\mathbf{M}_\mathrm{rel}$ are the Coriolis and relative forces and moments. Also, $\frac{d^2\mathbf{r}_\mathrm{cm}}{dt^2}$ is the acceleration of the COM in the inertial reference frame, $\boldsymbol{\omega}$ is the rotation vector of the body frame with respect to the inertial frame and $\tilde{\mathbf{r}}$ is the position of a mass element with respect to the COM of the body. While Eq. (3.7) can easily be inverted for isolating the linear acceleration of the body, the same is not possible for determining the rotational acceleration from Eq. (3.8). However, in case we are dealing with a rigid body, the latter can be simplified to the so called Euler equation, that directly expresses the angular acceleration vector of the body frame with respect to the inertial frame:

$$\dot{\boldsymbol{\omega}} = \mathbf{I}^{-1}\left(\tilde{\mathbf{M}}_\mathrm{cm} - \boldsymbol{\omega} \times \mathbf{I}\boldsymbol{\omega}\right) \tag{3.9}$$

where $\mathbf{I}$ is the inertia tensor of the body referred to the body frame B expressed as:

$$\mathbf{I} = \begin{bmatrix} I_{xx} & -I_{xy} & -I_{xz} \\ -I_{yx} & I_{yy} & -I_{yz} \\ -I_{zx} & -I_{zy} & I_{zz} \end{bmatrix} \tag{3.10}$$

$\mathbf{I}$ can be simplified if the body mass is symmetric with respect to some body axes and/or planes. The derivation of Eq.(3.7), (3.8) and (3.9), together with the defitions for the Coriolis and relative forces and moments, are not reported here, but can be found in Appendix A of Mooij [2015].

Consider now that the EOM Eq. (3.7) and (3.8) are defined in a reference frame whose origin is fixed to an arbitrary point of the surface of Mars. The Coriolis and relative forces and moments are due to the fact that this frame is non inertial, because it rotates with the planet, and due to time variations in mass distribution

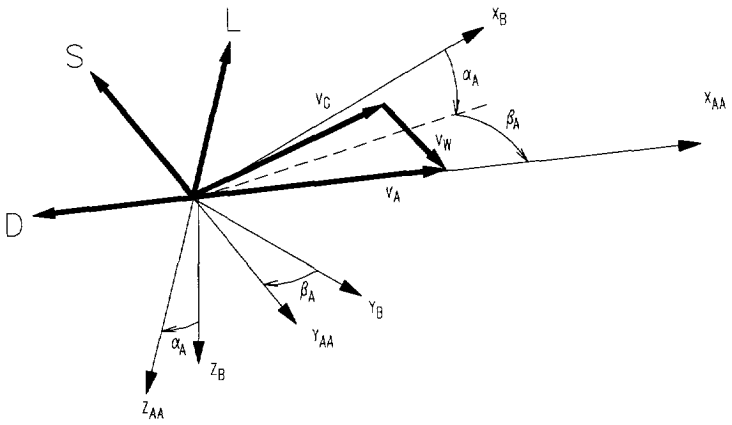

Figure 3.4: Aerodynamic forces defined in the aerodynamic AA-frame [Mooij, 1998a].

of the body. With respect to the parachute descent dynamics, however, we deal with a vehicle with constant mass and, also, the rotation of the planetary body does not have a significant influence on its motion since the descent flight is short. In such a case the effect of the relative forces and moments in the EOM can be neglected and the reference frame can be assumed to be inertial. In fact, if the planet does not rotate then this frame does not move with respect to the frame I described earlier. For convenience, in the following the EOM of the parachute-payload spacecraft will be defined in a frame, that will also be identified with the index I, whose origin lies in an arbitrary point of the surface of Mars[1]. The Z_I-axis is perpendicular to the surface pointing upwards. The Y_I- and X_I-axes complete the right handed system as shown in Figure 3.5.

What still remains to analyse before to derive the EOM describing the dynamics of the parachute descent vehicle are the forces that characterize its motion. If magnetic disturbances and gravitational perturbations of planetary bodies other than the central one are neglected, then the forces that dominate the motion of the spacecraft, to be translated into the same reference frame and included in the term $\mathbf{F}_\mathrm{I}$, are:

Aerodynamic forces

The aerodynamic forces (subscript 'a') depend on the air density and on the velocity of the vehicle. Most commonly they are determined in the AA-frame (see Figure 3.4) as:

$$\mathbf{F}_{\mathrm{a},AA} = \begin{pmatrix} -D \\ -S \\ -L \end{pmatrix} = \begin{pmatrix} -C_D q_\mathrm{dyn} S_\mathrm{ref} \\ -C_S q_\mathrm{dyn} S_\mathrm{ref} \\ -C_L q_\mathrm{dyn} S_\mathrm{ref} \end{pmatrix} \tag{3.11}$$

in which S_ref is the reference surface and the dynamic pressure is given by:

$$q_\mathrm{dyn} = \frac{1}{2}\rho V_a^2 \tag{3.12}$$

and C_D,C_S and C_L are the aerodynamic coefficients of the spacecraft and V_a its velocity with respect to the atmosphere. These coefficients are functions of the aerodynamic angles α and β, and of the Mach number M, that is:

$$M = \frac{V_a}{a} = \frac{V_a}{\sqrt{\gamma R T_\mathrm{air}}} \tag{3.13}$$

in which $a = \sqrt{\gamma R T_\mathrm{air}}$ is the speed of sound. In case of no wind it also holds that:

$$\mathbf{F}_{\mathrm{a},AG} = \mathbf{F}_{\mathrm{a},AA} \tag{3.14}$$

[1]This is possible because, according to the environment model described in Chapter 4, the variation of the characteristics of the atmosphere and gravity field of Mars as a function of the latitude and longitude of the spacecraft over the planet are neglected.

Aerodynamics does not only influence the motion of the COM, but also the motion around it. Indeed, a vehicle is characterized by both aerodynamic force coefficients and aerodynamic moment coefficients. The latter result in a moment around the COM that can be written, in the body frame B, as:

$$\mathbf{M}^{\mathbf{M}}_{\mathrm{a},B} = \begin{pmatrix} M_L \\ M_M \\ M_N \end{pmatrix} = \begin{pmatrix} C_l\, q_{\mathrm{dyn}}\, S_{\mathrm{ref}}\, b_{\mathrm{ref}} \\ C_m\, q_{\mathrm{dyn}}\, S_{\mathrm{ref}}\, c_{\mathrm{ref}} \\ C_n\, q_{\mathrm{dyn}}\, S_{\mathrm{ref}}\, b_{\mathrm{ref}} \end{pmatrix} \tag{3.15}$$

where b_{ref} and c_{ref} are the aerodynamic reference lengths for the roll and yaw rotations, and for the pitch rotation respectively. Also, in case the aerodynamic reference point, which is generally the suspension point of the model in the wind tunnel, does not coincide with the COM of the vehicle, the forces in Eq. (3.11) generate a moment around the latter that, with respect to the body frame B, can be expressed as:

$$\mathbf{M}^{\mathbf{F}}_{\mathrm{a},B} = \mathbf{r}_{\mathrm{cm}} \times \mathbf{C}_{B,AA}\mathbf{F}_{\mathrm{a},AA} \tag{3.16}$$

where $\mathbf{r}_{\mathrm{cm}} = (x_{\mathrm{cm}}, y_{\mathrm{cm}}, z_{\mathrm{cm}})^T$ is the position of the COM relative to the aerodynamic reference point. The total moment about the COM of the vehicle is the summation of these two characteristic moment contributions:

$$\mathbf{M}_{\mathrm{a},B} = \mathbf{M}^{\mathbf{M}}_{\mathrm{a},B} + \mathbf{M}^{\mathbf{F}}_{\mathrm{a},B} \tag{3.17}$$

It is remarked that when the aerodynamic moments or forces, that can be generated by each of the body elements of the spacecraft, are to be included in the EOM, a frame transformation is normally required.

Gravitational force

The second force contribution that is relevant for our study is the gravity force. This force is proportional to the gravitational acceleration and, with respect to the inertial frame I fixed to the surface of Mars defined earlier, is given by:

$$\mathbf{F}_{\mathrm{g},I} = m\mathbf{g}_I \tag{3.18}$$

in which $\mathbf{g}_I$ is given by Eq. (4.10). If the gravitational acceleration is not constant, and, in particular, proportional to the altitude, it causes a force gradient over the length of the spacecraft and, as a result, produces a gravitational moment acting on it. Nevertheless, this moment is much smaller with respect to the one produced by the aerodynamic and propulsive forces and can be neglected.

Propulsion forces

The last external force contribution we will take into account later on is the propulsion. In fact, as explained in Section 2, the propulsion force generated by the backshell thrusters is the one that the guidance system commands for controlling the trajectory of the spacecract during the descent. This force is normally defined with respect to the propulsion frame P or body fixed frame B. There exists extensive literature that explain the physical principles behind propulsion, but, since in the following we will exclusively consider the force generated by a generic engine, these are not discussed here. The interested reader is referred to Mooij [1998a] that dedicates some space to this topic. The performance of an engine can generally be characterized using the specific impulse:

$$I_{\mathrm{sp}} = \frac{T}{\dot{m}_e g_0} \tag{3.19}$$

in which $\dot{m}_e$ is the mass ejected from the exhaust per each second and g_0 the gravitational acceleration on the surface of the Earth. For EDL purposes hydrazine thrusters, with an I_{sp} around 240 s [Ley et al., 2009], represent a good solution because they ensure high performance with respect to the amount of thrust produced, robustness and responsiveness, at the cost of low consumption efficiency when compared with other types of engines. Also, the maximum thrust that hydrazine thrusters can generate varies between 1 N and 10 kN. The choice of an appropriate thrusters to use for guiding the spacecraft during the parachute descent, however, will be discussed in Chapter 8. The fuel consumption of an engine can be evaluated by rearranging Eq. (3.19):

$$m_f = \frac{T\Delta t}{I_{\mathrm{sp}} g_0} \tag{3.20}$$

in which Δt is the time fraction during which the thrust T remains constant.

3.2. RIGID BODY DYNAMICS

At this point we are ready for defining a model that can be used to derive analytical information about the main features of the dynamic behaviour of the system that has to be studied. This can be done by applying the theory introduced in Section 3.1.

Also, for the upcoming EOM derivation, Figure 3.5 can be used as a reference for the frames, system configuration and angle conventions. First, it has to be noticed that, while the I frame corresponds to the description given in Section 3.1.2, the AA frame depicted in this figure is different with respect to the one given in Figure 3.4. In particular, the Z_{AA}-axis is positive in the direction of the drag D and the lift force L is directed along the Y_{AA}-axis. The X_{AA}-axis, parallel to the side force S completes the right handed system. Also, as better explained later, the B frame is defined in such a way that the Z_B-axis corresponds to the rotational symmetry axis of the spacecraft. With this convention, in case of a nominal parachute descent flight, the X_{AA}-, X_B- and X_I-axes are all positive in the same direction and the Z-axes point upwards with respect to the surface of Mars. Finally, we will identify as pitching moment of the spacecraft, depending on the coefficient C_m, the moment around its X_B-axis. These choices are intended to make the frame situation easier to understand and more appropriate for the analysis of the flight dynamics of the parachute-payload system.

In addition to this, for a parachute descent in nominal conditions, i.e., a vertical flight in absence of wind, the drag D is directed upwards and the lift force L is almost parallel to the surface of Mars. For convenience thus we will refer to L as lateral force in the remainder of the study. Finally, it is remarked that for drawing clarity reasons the parachute COP and COM have been assumed to coincide and, also, for the purpose of showing the angle convention, the B and I frames have been translated in this point (their axes are dashed). The relative dimensions of the parachute backshell and payload elements are clearly unrealistic.

The first step in the derivation of the EOM is the introduction of some reasoned assumptions that are in agreement with the characteristics of the problem and the requirements for the analysis. The attitude motion of a parachute-payload system is characterized by two peculiar modes. The first is the pendulum-like mode while the second is the scissors-like mode. To start with the analysis of parachute-payload dynamics we only focus on the pendulum mode that can be fully described using a rigid body model. With this approach the EOM of the model greatly simplify but, on the other hand, the information about the relative motion of the elements of the spacecraft and, in turn, about the scissors motion mode that it determines, are lost. This aspect will be analysed later by means of a multibody model. The rigid body assumption, however, does not compromise the validity of the results obtained, in particular for the position-velocity trajectory of the system that is more significantly influenced by the pendulum motion. Finally, in steady-state flight conditions, when no external disturbances act on the body, the high descent velocity causes the aerodynamic force of the parachute to be very large in vertical direction. This, coupled with the weight of the payload, makes the structure of the system pretty stiff and limits the relative motion of the elements of the system.

Second, it is assumed that all the bodies of the spacecraft, i.e., the parachute, the backshell and the payload, are rotationally symmetric at least around one of their axes. Also, they are aligned in such a way that the resulting rigid body spacecraft is rotationally symmetric around the Z_B-axis, as Figure 3.5 shows. This configuration results in the fact that the characteristics of the motion of the body around the X_B- and Y_B-axes, and along the X_I- and Y_I-axes, are analogous. In addition, the rotation about the rotational symmetry axis Z_B does not have a significant impact on the trajectory of the spacecraft and is for the moment neglected. This aspect, however, has to be taken into account for the design of the scientific instrumentation and the navigation and control subsystems of the spacecraft. In fact, their use during the descent is critically influenced by the the rotational orientation of the vehicle with respect to the vertical direction. The resulting 2D 3DOF model, describing the translation along the Y_I- and Z_I-axes and the rotation around the X_B-axis, is sufficient for determining the critical information with respect to the dynamic stability of the system. This model is appropriate, because of its simplicity, to be used for analytical considerations. A similar 2D 3DOF model was indeed used also in Helmut and Lawrence Jr. [1965] for analogous studies.

The aerodynamic forces that the elements of the MPF reference spacecraft generate do not have the same magnitude and the relevance of their effect on the dynamics of the vehicle is not the same. In particular, we want to determine how the aerodynamic forces and moment generated by the parachute compare with respect to those due to the the payload body. While the data for the parachute are available from Cruz et al. [2003], the aerodynamic coefficients of the MPF capsule for the Mach number characterizing the descent phase (≈ 0.3), are not available. Nevertheless, as is proved by the comparison of Edquist et al. [2011], MPF capsule has the same geometry of the Phoenix capsule. This allows to assume that the aerodynamic properties of the latter, also available there, can be used for rough estimations of the dynamics of MPF. The drag forces are compared for $\alpha = 0^\circ$ while the lateral force and moment around the X_B-axis for $\alpha = 4^\circ$ (for other sample angles the situation

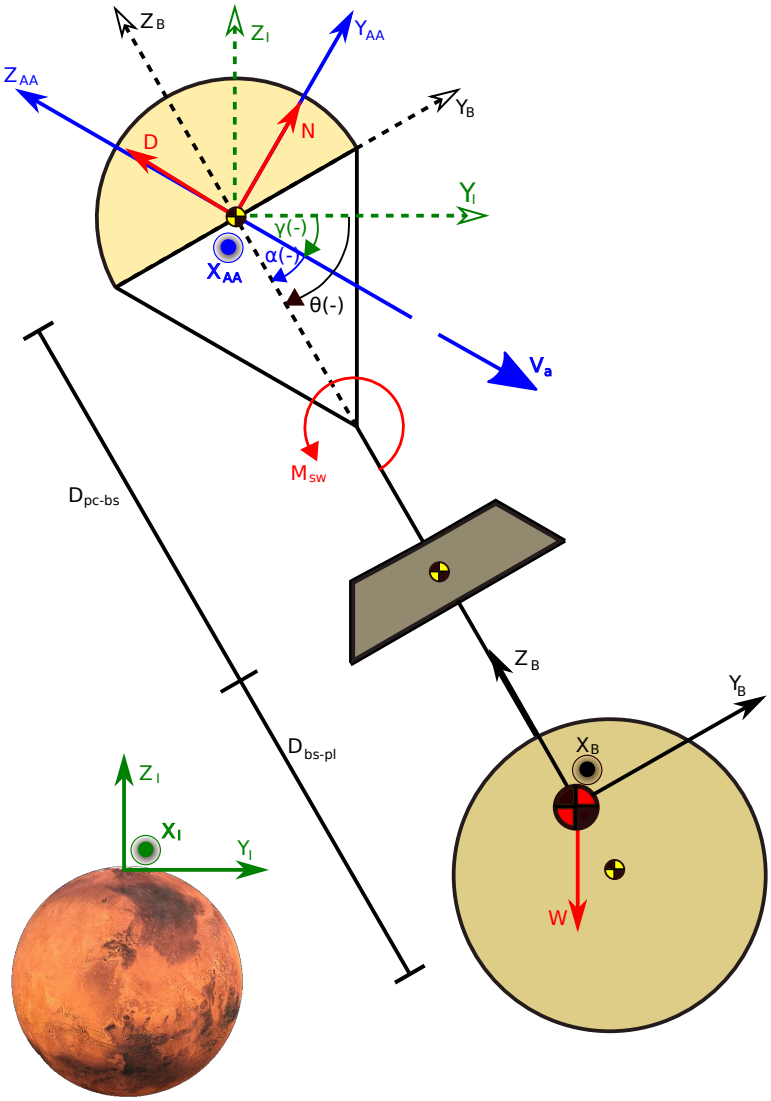

Figure 3.5: Parachute-backshell-payload spacecraft rigid body model dynamic analysis (dashed frames show the angle convention).

is analogous). We have:

$$\begin{aligned}
\frac{D_{\text{pc}}}{D_{\text{pl}}} &= \frac{C_{D,\text{pc}}(0°)S_{\text{ref,pc}}}{C_{D,\text{pl}}(0°)S_{\text{ref,pl}}} = \frac{0.345 \times 127.4}{1 \times 5.5} \approx 8 \\
\frac{L_{\text{pc}}}{L_{\text{pl}}} &= \frac{C_{L,\text{pc}}(4°)S_{\text{ref,pc}}}{C_{L,\text{pl}}(4°)S_{\text{ref,pl}}} = \frac{0.012 \times 127.4}{0.01 \times 5.5} \approx 28 \\
\frac{M_{\text{pc}}}{M_{\text{pl}}} &= \frac{C_{m,\text{pc}}(4°)S_{\text{ref,pc}}}{C_{m,\text{pl}}(4°)S_{\text{ref,pl}}} = \frac{-0.0224 \times 127.4}{-0.01 \times 5.5} \approx 52
\end{aligned} \tag{3.21}$$

Equation (3.21) clearly shows that the aerodynamics of the parachute dominates over the aerodynamic of the payload. This is valid also for the backshell whose contribution aerodynamic is comparable to that of the payload. This situation is typical of Mars EDL missions, where the low density of the atmosphere requests that the parachute is really large in comparison with the payload. The situation would be different on Earth. Another thing that has to be noticed is that the aerodynamic forces generated by the parachute have a much longer arm with respect to those of the other elements. In fact, the COM of the whole system is closer to the most massive body, i.e., the payload. Because of this, the parachute dominates the attitude behaviour of the spacecraft. With these considerations we can be sure that neglecting the aerodynamic effect of the payload and backshell on the dynamics of the system is a sustainable assumption that will greatly simplify the following analytical study.

3.2.1. TRANSLATIONAL EQUILIBRIUM

With these fundamental assumptions in mind it is now possible to start with the derivation of the EOM of the model. According to Newton, the translational equilibrium is expressed by the equation:

$$\mathbf{F}_{\text{ext}} = m_g \mathbf{a} \tag{3.22}$$

in which $\mathbf{F}_{\text{ext}}$ is the sum of all the external forces acting on the COM of the body, m_g is the body gravitational mass and $\mathbf{a}$ its acceleration vector. In this section all the vectors are 2D because we only consider the translation along the X_I- and Y_I-axes. The forces acting on the spacecraft are the aerodynamic forces generated by the parachute and the weight of the body itself. With respect to the inertial frame I, the latter is given by:

$$\mathbf{F}_{\text{g},I} = \mathbf{W} = m_g \mathbf{g}_I = \begin{pmatrix} 0 \\ m_g g \end{pmatrix} \tag{3.23}$$

in which the acceleration g is determined by the gravity model introduced in Section 4.2. The aerodynamic force vector acting on the parachute-payload system, defined with respect to the AA frame as given by Figure 3.5, is:

$$\mathbf{F}_{\text{a},AA} = \begin{pmatrix} L \\ D \end{pmatrix} \tag{3.24}$$

where the lateral force component L and the drag component D are still singularly defined as given by Eq. (3.11). Now we have all the forces that have to be included in the equilibrium expressed by Eq. (3.22). However, before to do so we need to express all of them with respect to the same reference frame that we choose to be the inertial reference frame I in Figure 3.5. While $\mathbf{F}_{g,I}$ is already expressed in the I frame, $\mathbf{F}_{a,AA}$ has to be appropriately transformed as:

$$\mathbf{F}_{\text{a},I} = \mathbf{C}_{I,AA} \mathbf{F}_{\text{a},AA} \tag{3.25}$$

where $\mathbf{C}_{I,AA}$ is the matrix expressing a clockwise rotation around the X_{AA}-axis that brings the Y_{AA}-axis on the Y_I-axis. The rotational angle is $\frac{\pi}{2} - (-\gamma)$ that, according to Figure 3.5, is the angle between the Y_I- and Y_{AA}-axes. We thus have:

$$\mathbf{F}_{\text{a},I} = \mathbf{C}_{I,AA} \mathbf{F}_{\text{a},AA} = \begin{bmatrix} \cos\left(\frac{\pi}{2}+\gamma\right) & -\sin\left(\frac{\pi}{2}+\gamma\right) \\ \sin\left(\frac{\pi}{2}+\gamma\right) & \cos\left(\frac{\pi}{2}+\gamma\right) \end{bmatrix} \begin{pmatrix} L \\ D \end{pmatrix} = \begin{pmatrix} -L\sin\gamma - D\cos\gamma \\ L\cos\gamma - D\sin\gamma \end{pmatrix} \tag{3.26}$$

By inserting Eq. (3.23) and (3.26) in Eq. (3.22) we get:

$$\mathbf{F}_{\text{g},I} + \mathbf{F}_{\text{a},I} = m_g \mathbf{a}_I \tag{3.27}$$

and, after rearrangement:

$$\mathbf{a}_I = \begin{pmatrix} \ddot{y} \\ \ddot{z} \end{pmatrix} = \begin{pmatrix} \frac{-L\sin\gamma - D\cos\gamma}{m_g} \\ g + \frac{L\cos\gamma - D\sin\gamma}{m_g} \end{pmatrix} \tag{3.28}$$

where the gravitational acceleration g, that pulls the spacecraft towards the surface of the planet, is negative in the inertial frame I.

3.2.2. ROTATIONAL EQUILIBRIUM

For the rotational equilibrium around the X_B-axis an Eq. similar to (3.22) holds. This corresponds to Eq. (3.9) for the case in which the the body rotates exclusively with respect to its X_B-axis:

$$\mathbf{M}_{\text{ext},X_B} = I_{X_B} \ddot{\boldsymbol{\theta}} \tag{3.29}$$

where θ is the parachute attitude angle between the Y_I-axis and the Z_B-axis, M_{ext,X_B} is the sum of the external moments acting on the body around its X_B-axis and I_{X_B} is the moment of inertia of the body also around X_B.

Differently from the previous section, the analysis of the rotational motion of the body requests that we deal with 3D vectors even if we are exclusively interested in the rotation about the X_B-axis. This is because rotation vectors are perpendicular to the rotational plane. Also, the side force S is assumed to be always null as well as the moments around the Y_B- and Z_B-axes.

The external moments acting on the body once more have aerodynamic and gravitational origin. The gravitational moment around the X_B-axis is given by:

$$\mathbf{M}_{g,X_B} = \mathbf{L}_{pc,B} \times \mathbf{F}_{g,pc,I} + \mathbf{L}_{bs,B} \times \mathbf{F}_{g,bs,I} + \mathbf{L}_{pl,B} \times \mathbf{F}_{g,pl,I} \tag{3.30}$$

in which the gravity force vectors, one per each element of the spacecraft, is defined according to Eq. (3.18) and Eq. (4.10), with h being the altitude of the corresponding spacecraft element. $\mathbf{L}_{pc}$, $\mathbf{L}_{bs}$ and $\mathbf{L}_{pl}$ are respectively the positions, in the B frame centred in the rigid body COM (red and black circle in Figure 3.5), of the the parachute, backshell and payload COM (yellow and black circles in Figure 3.5). These vectors are given by:

$$\mathbf{L}_{pc} = \begin{pmatrix} 0 \\ 0 \\ z_{pc} \end{pmatrix} \quad \mathbf{L}_{bs} = \begin{pmatrix} 0 \\ 0 \\ z_{bs} \end{pmatrix} \quad \mathbf{L}_{pl} = \begin{pmatrix} 0 \\ 0 \\ z_{pl} \end{pmatrix} \tag{3.31}$$

The rigid body COM position along the Z_B-axis with respect to the parachute COM can be determined as a function of the distances between the elements of the spacecraft and their masses:

$$z_{pc} = \frac{m_{bs} D_{pc\text{-}bs} + m_{pl}(D_{pc\text{-}bs} + D_{bs\text{-}pl})}{m_{pc} + m_{bs} + m_{pl}} \tag{3.32}$$

in which $D_{pc\text{-}bs}$ and $D_{bs\text{-}pl}$, as Figure 3.5 shows, are the distances between the COM of the parachute and the backshell and between the COM of the backshell and the payload and can be estimated if one knows the geometric properties of the parachute payload system, in particular the suspension lines length and their angle with respect to the Z_B-axis and the riser lengths, available in Section 3.2.3. The positions of the backshell and payload with respect to the body COM follow as:

$$z_{bs} = z_{pc} - D_{pc\text{-}bs} \tag{3.33}$$

$$z_{pl} = z_{pc} - D_{pc\text{-}bs} - D_{bs\text{-}pl} \tag{3.34}$$

The gravitational moment as given by Eq. (3.35) turns out to be almost null per every configuration of the system. In fact, the gravitational acceleration g varies as a function of the altitude and this generates a gravity force gradient on the body that depends on its attitude. The effect on the attitude behaviour of the spacecraft of the resulting gravity gradient torque, however, is negligible with respect to the aerodynamic contribution of the parachute. We thus can assume:

$$\mathbf{M}_{g,X_B} \approx 0 \tag{3.35}$$

The attitude of the parachute-payload system is completely governed by the aerodynamic forces. The moment they generate is defined as:

$$\mathbf{M}_{a,X_B} = \mathbf{M}_{sw} + \mathbf{L}_{COP} \times \mathbf{F}_{a,AA} \tag{3.36}$$

in which the aerodynamic moment generated around the swivel point of the parachute body, in agreement with Figure 3.5, is:

$$\mathbf{M}_{sw} = M_{sw} \hat{\mathbf{x}}_B \tag{3.37}$$

where $\hat{\mathbf{x}}_B$ is the X_B-axis unit vector and M_{sw}[2], defined as in Eq. (3.15), is a function of the parachute aerodynamic moment coefficient C_m defined later. The position of the center of pressure of the parachute $\mathbf{L}_{COP}$, with respect to the body frame B, is:

[2] Since we are dealing with a 2D model in the following we will also refer to M_{sw} as simply M

$$\mathbf{L}_{\text{COP}} = \begin{pmatrix} 0 \\ 0 \\ z_{\text{COP}} \end{pmatrix} \tag{3.38}$$

To simplify the computation of the cross product in Eq. (3.36) we choose to first express $\mathbf{F}_{\text{a},AA}$ with respect to the frame B. To do so frame AA has to be rotated clockwise of an angle $-\alpha$. This gives:

$$\mathbf{F}_{\text{a},B} = \mathbf{C}_{B,AA}\mathbf{F}_{\text{a},AA} \begin{bmatrix} 1 & 0 & 0 \\ 0 & \cos(-\alpha) & -\sin(-\alpha) \\ 0 & \sin(-\alpha) & \cos(-\alpha) \end{bmatrix} \begin{pmatrix} 0 \\ L \\ D \end{pmatrix} = \begin{pmatrix} 0 \\ L\cos\alpha + D\sin\alpha \\ -L\sin\alpha + D\cos\alpha \end{pmatrix} \tag{3.39}$$

By inserting Eq. (3.37), (3.48) and (3.39), we get:

$$\begin{aligned} \mathbf{M}_{\text{a},X_B} &= M_{\text{sw}}\hat{\mathbf{x}}_B + \begin{pmatrix} 0 \\ 0 \\ z_{\text{COP}} \end{pmatrix} \times \begin{pmatrix} 0 \\ L\cos\alpha + D\sin\alpha \\ -L\sin\alpha + D\cos\alpha \end{pmatrix} \\ &= (M_{\text{sw}} - z_{\text{COP}}(L\cos\alpha + D\sin\alpha))\hat{\mathbf{x}}_B \end{aligned} \tag{3.40}$$

The resulting rotational EOM is:

$$\ddot{\boldsymbol{\theta}} = \frac{M_{\text{sw}} - z_{\text{COP}}(L\cos\alpha + D\sin\alpha)}{I_{X_B}}\hat{\mathbf{x}}_B \tag{3.41}$$

3.2.3. MARS PATHFINDER MODEL CHARACTERISTICS

To completely define a dynamic model, determining its EOM, i.e., its structure, is not enough. In particular, the forces and inertia parameters that are in these EOM need to be specified as well. While the structure of the model generally defines the type of motion, its parameters give a 'dimension' to this motion. For example, if the EOM of a parachute-payload system characterize an oscillatory behaviour, then the mass of the payload and the size of the parachute will determine the frequency of the oscillations, the damping factor of the system and so on.

The present study, amongst others, has the aim of evaluating how the dynamic stability characteristics of the model are influenced by its parameters. Because of this, some of them will not be kept fixed during simulations. Nevertheless, it is fundamental to define a nominal configuration that can be used not only to understand the effect of parameter variation but also for model validation and verification purposes.

GEOMETRIC AND MASS PROPERTIES

The mass and geometric properties for our reference vehicle MPF have already been calculated by Abdulkadir [2011]. Its results, reported below, will be reused for completing the dynamic model presented earlier but their derivation is omitted.

The MPF spacecraft is equipped with a disk-gap-band parachute with a nominal diameter of D_0 of 12.74 m. Its reference surface can be found as the corresponding circular area:

$$S_{\text{ref}} = \pi\left(\frac{D_0}{2}\right)^2 = 127.48\ \text{m}^2 \tag{3.42}$$

Abdulkadir [2011] estimates the mass of the parachute by assuming that the canopy is half sphere with a certain surface density depending on its material and that the suspension lines are cylinders. The available geometric and density data yield respectively a canopy mass m_{can} of 13.8 kg and a suspension lines mass m_{sus} of 2.3 kg. The moment of inertia for the rotation around the $X_{B,\text{pc}}$-axis, that is parallel to X_B but passing through the parachute COM, once more assuming that it is an half sphere and that the suspension lines COM coincides with the one of the canopy, is given by:

$$I_{\text{pc},X_B} = \frac{5}{12}\left(\frac{D_0}{2}\right)^2 m_{\text{can}} + \frac{1}{12}L_{\text{sus}}\cos^2\Phi_{\text{sus}}\, m_{\text{sus}} = 276.16\ \text{kg m}^2 \tag{3.43}$$

Table 3.2 summarizes the values of the parameters that characterize the disk-gap-band parachute MPF was equipped with.

Table 3.2: Mars Pathfinder disk-gap-band parachute mass and geometry characteristics [Abdulkadir, 2011].

Nomenclature	Description	Value
D_0 [m]	Nominal parachute diameter	12.74
S_{ref} [m^2]	Reference canopy area	127.48
p_{can} [-]	Canopy porosity	0.2
ρ_{can} [kg/m^2]	Canopy surface density	0.054
R_{can} [m]	Canopy radius	6.37
L_{sus} [m]	Suspension lines length	21.65
ρ_{sus} [kg/m^3]	Suspension lines density	1470.0
d_{sus} [m]	Suspension lines diameter	0.0015
N_{sus} [-]	Suspension lines number	40
Φ_{sus} [°]	Suspension line half-cone angle	17.37
m_{sus} [kg]	Suspension lines mass	2.3
m_{can} [kg]	Canopy mass	13.8
m_{pc} [kg]	Parachute mass	16.1
I_{pc,X_B} [kg m^2]	Moment of inertia around the X_{pc}-axis	276.16

Table 3.3: Mars Pathfinder backshell mass and geometry characheristics [Abdulkadir, 2011].

Nomenclature	Description	Value
m_{wall} [kg]	Backshell wall mass	56.9
m_{plate} [kg]	Backshell upper plate mass	2.9
m_{bs} [kg]	Backshell mass	59.8
I_{bs,X_B} [kg m^2]	Moment of inertia around the X_{bs}-axis	28.7

Table 3.4: Mars Pathfinder payload mass and geometry characteristics [Abdulkadir, 2011].

Nomenclature	Description	Value
R_{pl} [m]	Payload radius	2
m_{pl} [kg]	Payload mass	287.8
ρ_{pl} [kg/m^3]	Payload density	8.59
I_{pl,X_B} [kg m^2]	Moment of inertia around the X_{pl}-axis	460.48

The backshell of MPF comprises the lateral wall, the upper plate and the heatshield. The latter is significantly massive and is ejected when the payload gets extracted, just after the main parachute depletion and stabilization, so that the spacecraft gets more decelerated. This is why its contribute to the mass and moment of inertia of this body is not taken into account. The mass and geometric properties of the backshell are reported in Table 3.3.

The payload mass corresponds to the weight of the MPF lander plus the airbag system that absorbs the residual kinetic energy at touchdown. By assuming that the payload is a sphere with radius R_{pl}, Abdulkadir [2011] estimates the payload density as:

$$\rho_{\text{pl}} = \frac{3}{4}\frac{m_{\text{pl}}}{\pi R_{\text{pl}}^3} = 8.59 \text{ kg/m}^3 \tag{3.44}$$

from which the payload moment of inertia, that for a sphere is the same with respect to each of its 3 symmetry axes, is:

$$I_{X_{\text{pl},B}} = \frac{8}{15}\pi\rho_{\text{pl}}R_{\text{pl}}^5 = 460.48 \text{ kg m}^2 \tag{3.45}$$

Finally, for the inertia properties of the body, it is important to determine how the parachute, the backshell and the payload are placed with respect to each other. In other words we want to define the distances between the parachute and the backshell $D_{\text{pc-bs}}$ and between the backshell and the payload $D_{\text{bs-pl}}$. By assuming that the swivel point of the parachute, where the suspension lines meet, corresponds to the backshell COM and that the parachute body COM is where the parachute canopy begins, then we have:

Table 3.5: Mars Pathfinder distances between elements COM [Abdulkadir, 2011].

Nomenclature	Description	Value
$D_{\text{pc-bs}}$ [m]	Parachute-backshell COM distance	20.66
$D_{\text{bs-pl}}$ [m]	Backshell-payload COM distance	5

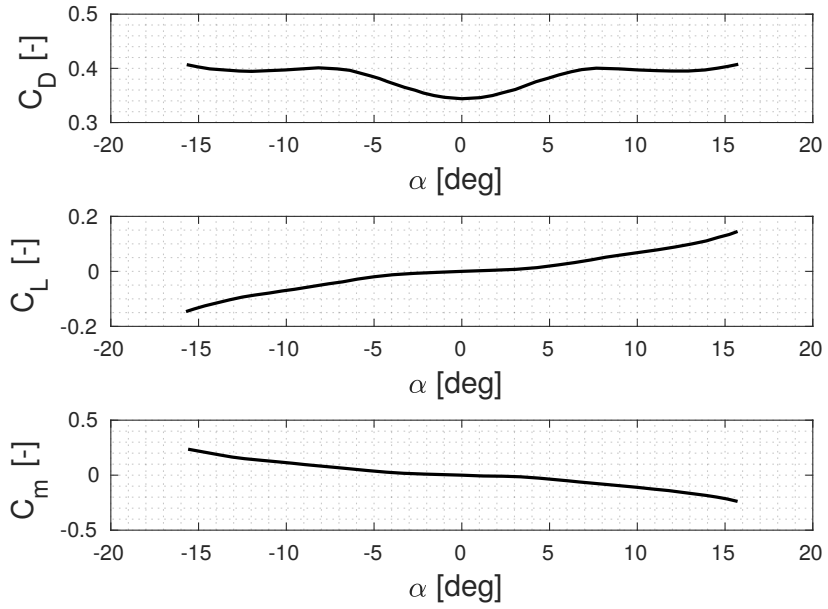

Figure 3.6: Mars Pathfinder parachute aerodynamic coefficients for $M = 0.29$ as a function of α. Adapted from Cruz et al. [2003].

$$D_{\text{pc-bs}} = L_{\text{sus}} \cos \Phi_{\text{sus}} = 20.66 \text{ m} \tag{3.46}$$

The riser between the backshell COM and the payload COM, corresponding to $D_{\text{bs-pl}}$, is instead assumed to be 5 m long, as already introduced in Section 2.5.

AERODYNAMIC PROPERTIES

The aerodynamic forces and moments the parachute generates depend on the aerodynamic coefficients. Its rotational symmetry around the Z_B-axis results in the fact that its aerodynamic properties are fully defined by only 3 coefficients, i.e., the drag coefficient C_D, the side force coefficient C_L and the aerodynamic moment coefficient C_m that are a function of the Mach number M and of the angle of attack α. This can be determined as a function of the state of the spacecraft as:

$$\alpha = \theta - \gamma \tag{3.47}$$

As already introduced, our reference vehicle is the MPF whose disk-gap-band aerodynamic data are available from Cruz et al. [2003], who determined experimentally the functions $C_D(\alpha)$, $C_L(\alpha)$ and $C_m(\alpha)$ for $M = 0.29$. It has been verified that in steady-state descent the Mach number that the MPF parachute experiences is between 0.2 and 0.3. Since this condition is realistic for the the nominal steady-state flight of MPF then the values from Cruz et al. [2003] are appropriate for our purpose. The aerodynamic coefficients as a function of α are given in Figure 3.6, that is consistent with the convention of Figure 3.7. It is important to notice that the C_D is symmetrical with respect to $\alpha = 0°$ and always positive, while C_L and C_m, according to the force convention in Figure 3.5, always result in moments that tend to decrease $\|\alpha\|$, thus contributing to making more stable the attitude oscillatory behaviour of the spacecraft.

The aerodynamic forces that the parachute generates are applied in its COP. This point, despite being always located on the Z_B-axis of the parachute thanks to its rotational symmetry, moves along it depending on

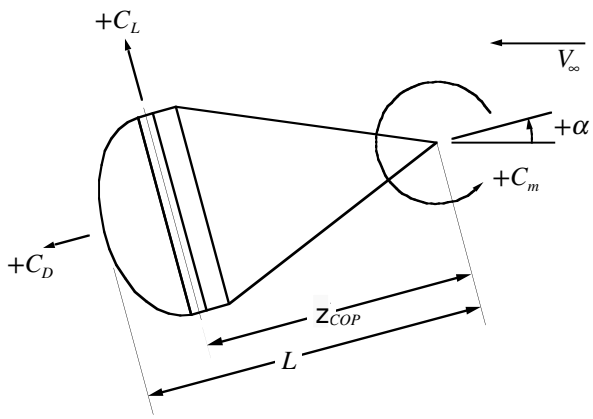

Figure 3.7: Mars Pathfinder parachute aerodynamic coefficients convention. Adapted from Cruz et al. [2003].

α and M. Its position with respect to the swivel point, still according to Cruz et al. [2003], can be determined as:

$$z_{\text{COP}} = -\frac{C_m}{C_L} D_0 \tag{3.48}$$

A final notice has to be made on the determination of the airspeed. In fact, the velocity of the spacecraft with respect to the atmosphere, is determined by the velocity of the spacecraft with respect to the inertial system and by the wind speed. However, since also the speed of the parachute with respect to the atmosphere due to its oscillatory motion has to be taken into account, we have:

$$\mathbf{V}_a = \mathbf{V}_I - \mathbf{V}_{\text{w},I} + \dot{\theta} \begin{pmatrix} -\sin\theta \\ \cos\theta \end{pmatrix} z_{\text{COP}} \tag{3.49}$$

PARACHUTE ADDED MASS

When dealing with parachute systems one has to take into account the added mass effect. The added mass of the parachute is the air mass that is contained inside its canopy. This air is not subjected to the gravitational force but, of course, when the parachute moves this air has to be moved as well. In other words the added mass cause an increase in the inertial mass and moment of inertia of the parachute.

There exist several ways to model the added mass effect. One of the most straightforward approaches, implemented by Guglieri [2012], consists of estimating the air mass of a hemispherical parachute as:

$$m_a = \frac{2}{3}\pi \left(\frac{D_0}{2}\right)^3 \rho k_a \tag{3.50}$$

in which ρ is the air density and k_a is a factor that depends on the porosity of the parachute p that is generally around 0.2:

$$k_a = 1.068\left(1 - 1.465p - 0.25975p^2 + 1.2626p^3\right) \tag{3.51}$$

The added mass moment of inertia is estimated once more as if the air mass has a hemispherical shape. Assuming that the COM of the air mass coincides with the COM of the parachute, with respect to the X_B-axis then we have:

$$I_{a,X_B} = \frac{2}{5} m_a \left(\frac{D_0}{2}\right)^2 + m_a z_{\text{pc}}^2 \tag{3.52}$$

In summary, according to this approach the added mass causes an increase in total inertial mass and moment of inertia of the parachute. The relevance of this effect, since ρ is a function of altitude, will vary along the descent trajectory.

3.3. MULTIBODY DYNAMICS

The rigid body model of the parachute-backshell-payload system, as discussed earlier, is appropriate for deriving analytical expressions that can describe its dynamic behaviour. However, it can only simulate the pendulum-like motion of the parachute. In fact, the relative motion of the elements of the descending spacecraft is inhibited and for the purpose of analysing it a multibody model is necessary.

As introduced in Section 2.4, a number of models of parachute-payload and parafoil-payload systems have been developed since the 1960s. The general trend in the evolution of these models consisted in a constant increase of DOF for the system and the addition and optimization of new features, such as the added mass inertial effect. One that is particularly interesting is the model developed by Abdulkadir [2011] and based on the Wittenburg [2008] formalism. A second option consists instead of implementing a multibody model based on the methodology of Neustadt et al. [1967]. The latter approach makes it possible to build a multibody model in a small amount of time, when compared to other methods, at the cost of a loss in robustness and numerical efficiency of the resulting simulator. With respect to the purpose of the present study, such a model would clearly ensure the capability to gather all the data relevant for the relative motion of the parachute, backshell and payload. In addition, it would give the possibility to easily integrate the thrust force on it without the need to significantly modify the existing EOM, that directly derive from those already defined for the rigid body model in Section 3.2.

In Section 3.3.1, the characteristics of the methodology of Neustadt et al. [1967] will be introduced and then, with the help of the physical double pendulum example, its advantages and disadvantages will be analysed in light of the objective of the present work, also in comparison the approach of Wittenburg [2008]. This analysis will lead to the choice of one of the options introduced in the previous paragraph. Section 3.3.2 finally introduces the multibody model describing the motion of the parachute-backshell-payload spacecraft.

3.3.1. THE NEUSTADT MULTIBODY METHODOLOGY

The interest of the space engineering community with respect to multibody mechanics started to grow in the 1960s, triggered by the desire to understand more about the motion of parachute-payload systems, considering that the parachute descent was a critical phase of missions such as Gemini, Mercury and, later, Apollo.

One of the earliest publications that applies multibody mechanics in the field of space engineering is Neustadt et al. [1967]. Its objective was to determine the optimal position for anchoring the parachute, through the riser, to the Apollo capsule. The concept at the base of the model they built for the study consisted of considering each body, the rigid parachute and the capsule, as moving independently with respect to each other, under the influence of their respective aerodynamic and gravitational forces and moments, and the tension generated by the riser connecting them, modelled as a massless spring. In this way it is possible to describe the dynamics of each element of the system as it is a stand-alone rigid body without the need to determine any constraint force between them. In fact, the force that one element exerts on another connected to it is not direct, but is instead the result of the lengthening of the pseudo spring. This lengthening is caused by the fact that during the propagation step each body moves exclusively under the influence of its own forces and the elastic force that remains constant during the step.

The paper of Neustadt et al. [1967], however, does not describe a multibody methodology in detail. This is why it is assumed to be useful and scientifically significant to analyse and develop the characteristics of the approach of Neustadt et al. [1967] in a more structured way. This will be done with the help of the physical double pendulum example, to give a preliminary overview of its advantages and disadvantages, also with the aim to determine whether it represents a good option for the purpose of the present study.

The mechanics of the double pendulum is a classical physics problem. In fact, there exist several models describing its dynamics and kinematics. In particular, it is very well suited for validating a multibody methodology and for determining its main properties. The physical double pendulum we will use, shown in Figure 3.8, consists of two equivalent rigid bars of mass m and length l interconnected through a pivot that inhibits the relative translation of two corresponding extremes of the bars. The COM of these bars is placed halfway between its extremes. The system of two bars is fixed to the ceiling also with a pivot that does not allow the translation of bar 1 with respect to an inertial reference frame.

According to the concept introduced in Neustadt et al. [1967], to obtain the EOM of the double pendulum system using this approach it is sufficient to describe the dynamics of each bar independently, subjected to the gravitational force and the elastic forces of the connections. In particular, bar 1 will be subjected to the gravitational force due to its mass and the elastic force $\mathbf{F}_{e,a}$ due to the pivot between the ceiling and bar 1 and the elastic force $\mathbf{F}_{e,b}$ due to the pivot between bar 1 and bar 2, while instead the dynamics of bar 2 will be deter-

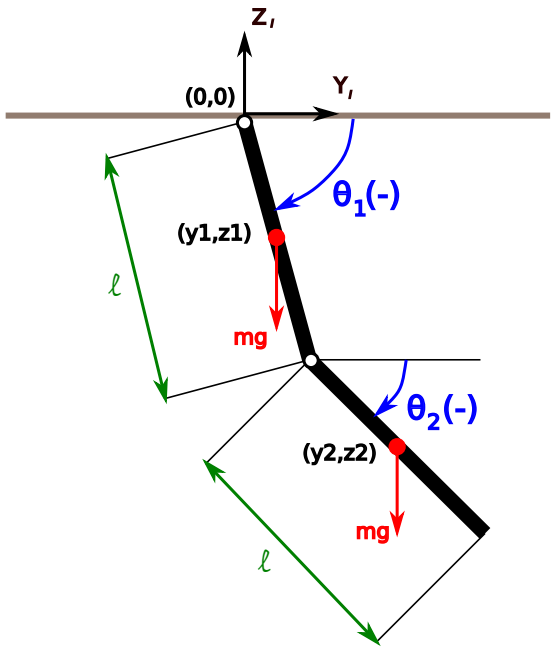

Figure 3.8: The physical double pendulum.

mined by its gravitational force and the elastic force $\mathbf{F}_{e,b}$ of the pivot between bar 1 and bar 2. It is remarked that the same pseudo spring exerts a force with opposite direction with respect to the two bars that it connects. The derivation of the EOM for the single bars is simple and the procedure is analogous to what already done for the rigid body parachute-payload system and will not be repeated here. By exclusively considering the translation and rotation of the system elements in the vertical plane, then the EOM for the two bars are:

$$\begin{aligned}
\ddot{y}_1 &= \frac{F_{e,a}\cos\theta_{c,a} - F_{e,b}\cos\theta_{c,b}}{m} \\
\ddot{z}_1 &= g_0 + \frac{F_{e,a}\sin\theta_{c,a} - F_{e,b}\sin\theta_{c,b}}{m} \\
\ddot{\theta}_1 &= \frac{-F_{e,a}\sin\left(\theta_{c,a}-\theta_1\right)l - F_{e,b}\sin(\theta_{c,b}-\theta_1)l}{2I} \\
\ddot{y}_2 &= \frac{F_{e,b}\cos\theta_{c,b}}{m} \\
\ddot{z}_2 &= g_0 + \frac{F_{e,b}\sin\theta_{c,b}}{m} \\
\ddot{\theta}_2 &= \frac{-F_{e,b}\sin(\theta_{c,b}-\theta_2)l}{2I}
\end{aligned} \tag{3.53}$$

in which I is the moment of inertia of the bars with respect to the axis passing through their COM and perpendicular to the YZ-plane. Also, $F_{e,a}$, $F_{e,b}$ and $\theta_{c,a}$, $\theta_{c,b}$ are, respectively, the magnitudes and directions of the elastic forces due to the lengthening of the connections and have to be determined externally.

The pivot connections are assumed to be massless springs of 0 nominal length that can only transfer force along their extension. At each integration step we can reconstruct the position of the hinges of the bars and from this calculate the distance between them and, thus, the elongation of the pseudo spring. This elongation in turn yields the magnitude of the elastic forces, proportional to the spring elastic constant k. In addition, once more using the hinge positions, we can also determine the orientation of the pseudo spring, i.e., $\theta_{c,a}$, $\theta_{c,b}$, that, as said, determine the directions along which the elastic forces are transmitted. Clearly, in case of no elongation and 0 nominal length of the connection, it is not possible to determine the force direction, but since in this case the force is null then this does not cause any singularity. The position of the hinges of connection a between the ceiling and bar 1 and of the hinges of connection b between bar 1 and bar 2 with respect to the rigid bodies they bond, labelled respectively with 0,1 and 2, are:

$$\begin{aligned}
\mathbf{h}_{0a} &= \begin{pmatrix} 0 \\ 0 \end{pmatrix} \\
\mathbf{h}_{1a} &= \begin{pmatrix} y_1 - \frac{l}{2}\cos\theta_1 \\ z_1 - \frac{l}{2}\sin\theta_1 \end{pmatrix} \\
\mathbf{h}_{2b} &= \begin{pmatrix} y_1 + \frac{l}{2}\cos\theta_1 \\ z_1 + \frac{l}{2}\sin\theta_1 \end{pmatrix} \\
\mathbf{h}_{2b} &= \begin{pmatrix} y_2 - \frac{l}{2}\cos\theta_2 \\ z_2 - \frac{l}{2}\sin\theta_2 \end{pmatrix}
\end{aligned} \tag{3.54}$$

From these positions it is possible to derive the polar coordinates of the vector connecting the hanging point in the ceiling and the upper extreme of bar 1, and the vector connecting the lower extreme of bar 1 with the upper extreme of bar 2. We have:

$$\begin{aligned}
\begin{pmatrix} \rho_a \\ \theta_{c,a} \end{pmatrix} &= \texttt{cart2pol}\,(\mathbf{h}_{1a} - \mathbf{h}_{0a}) \\
\begin{pmatrix} \rho_b \\ \theta_{c,b} \end{pmatrix} &= \texttt{cart2pol}\,(\mathbf{h}_{2b} - \mathbf{h}_{2a})
\end{aligned} \tag{3.55}$$

where the function `cart2pol`, used for transforming Cartesian coordinates to polar coordinates, is defined as:

$$\texttt{cart2pol}(\mathbf{v}) = \begin{pmatrix} \rho_\mathbf{v} \\ \theta_\mathbf{v} \end{pmatrix} = \begin{pmatrix} \sqrt{y^2 + z^2} \\ \text{atan}\left(\frac{z}{y}\right) \end{pmatrix}, \quad \mathbf{v} = \begin{pmatrix} y \\ z \end{pmatrix} \tag{3.56}$$

Finally, assuming that the hinges of the double pendulum have nominal length 0, the magnitude of the elastic forces, proportional to the elongation of the pseudo springs, is given by:

$$\begin{aligned}
F_{e,a} &= -k\rho_a \\
F_{e,b} &= -k\rho_b
\end{aligned} \tag{3.57}$$

The definition of the dynamics of the double pendulum is concluded and we can already highlight some aspects that characterize the methodology. First, it is clear that the procedure is really pragmatic since there is no need to define abstract elements such as the energy-like function we need for the derivation with the Lagrange method, or mathematical entities such as the topology matrix, that instead we use when applying the Wittenburg [2008] formalism. The constraint forces or the analysis of the dynamic equilibrium in the confluence point are also not required. In principle, one could add an infinite number of other rigid elements to the system without the need to modify the EOM for those that are not not directly connected with it. This is because they are all independent and the only influence between them is the pseudo springs connecting them. This simplicity, however, comes at the price that, since the dynamics of each body is considered independently, the connections between them do not result in a reduction of DOF for the total multibody system with respect to the total number of DOF of all the single elements.

The physical double pendulum has rigid connections. This means that the rigidity of the pseudo springs should be infinite. Nevertheless, this is mathematically impossible because in such a situation, even for a very small elongation, the resulting elastic forces in Eq. (3.64) would be infinite as well. The only way to model a system with rigid connections, and in particular the double pendulum of Figure 3.8, with the methodology of Neustadt et al. [1967] is to assume that the elastic constant k is really large. This, as we will see in the following, can cause numerical issues.

The properties of the pseudo springs, together with the mass and geometric properties of the elements of the multibody, will determine vibrations during the propagation of its trajectory. While this represents an unwanted effect for the case of systems with rigid connections, if some elements of the multibody are connected

Table 3.6: Characteristics of the double pendulum for the simulation of Figure 3.9.

Parameter	Value
k_1 [N/m]	10000
k_2 [N/m]	10000
m [kg]	2
l [m]	40
g_0 [m/s^2]	−9.81

Table 3.7: Initial conditions of the double pendulum for the simulation of Figure 3.9.

Parameter	Value
$\theta_{1,0}$ [deg]	−75
$\theta_{2,0}$ [deg]	−20
$\dot{\theta}_{1,0}$ [deg/s]	0
$\dot{\theta}_{2,0}$ [deg/s]	0

through ropes or similar, the possibility to simulate their elasticity represents a value added for this methodology. However, as we will see later, by using very rigid pseudo springs in relation to the involved masses of the multibody elements, the vibration effect can be made negligible for the attitude and trajectory of the system.

To verify that the concept of Neustadt et al. [1967] is valid and to understand how the vibrations influence the simulation of the motion of the physical double pendulum it is possible to compare the model derived in the previous paragraphs with a model obtained by Abdulkadir [2011] using Lagrangian mechanics. With this model, the dynamics of the system can be fully described by means of the attitude angles θ_1^* and θ_2^*, whose relation with the attitude angles θ_1 and θ_2 in Figure 3.8 is:

$$\theta_1^* = \frac{\pi}{2} - \theta_1, \quad \theta_2^* = \frac{\pi}{2} - \theta_2 \tag{3.58}$$

The EOM for this Lagrange model are:

$$\begin{aligned} \dot{\theta}_1^* &= \frac{6}{ml^2} \frac{2p_{\theta_1^*} - 3\cos\left(\theta_1^* - \theta_2^*\right) p_{\theta_2^*}}{16 - 9\cos^2\left(\theta_1^* - \theta_2^*\right)} \\ \dot{\theta}_2^* &= \frac{6}{ml^2} \frac{8p_{\theta_2^*} - 3\cos\left(\theta_1^* - \theta_2^*\right) p_{\theta_1^*}}{16 - 9\cos^2\left(\theta_1^* - \theta_2^*\right)} \end{aligned} \tag{3.59}$$

in which the time derivative of the two momenta $p_{\theta_1^*}$ and $p_{\theta_2^*}$, that correspond to the derivative of the Lagrangian function associated to the physical double pendulum, with respect to $\dot{\theta}_1^*$ and $\dot{\theta}_2^*$, are defined as:

$$\begin{aligned} \dot{p}_{\theta_1^*} &= -\frac{1}{2} ml^2 \left[\dot{\theta}_1^* \dot{\theta}_2^* \sin\left(\theta_1^* - \theta_2^*\right) + 3\frac{g}{l} \sin\theta_1^*\right] \\ \dot{p}_{\theta_2^*} &= -\frac{1}{2} ml^2 \left[-\dot{\theta}_1^* \dot{\theta}_2^* \sin\left(\theta_1^* - \theta_2^*\right) + 3\frac{g}{l} \sin\theta_2^*\right] \end{aligned} \tag{3.60}$$

Figure 3.9 shows a comparison between the simulated motion of the double physical pendulum using either the model derived using the Lagrange formalism and the one obtained using the Neustadt method. The pendulum characteristics and sample IC are given respectively in Table 3.6 and Table 3.7. The correspondance of the two trajectories proves that the concept of Neustadt et al. [1967] is valid for building multibody models.

The good correspondence between the simulation results of the two models has been obtained using a stringent integrator[3] tolerance for both models, i.e., `RelTol` = 10^{-5} and `AbsTol` = 10^{-8}, so that also the 50 s propagation has required a significant amount of computational time. With lower tolerances, however, already at around 50 s it is possible to notice that the trajectories of the two simulated pendula do not coincide. In fact,

[3] For the integration, the `Matlab` function `ode45` implementing a Runge-Kutta routine has been used.

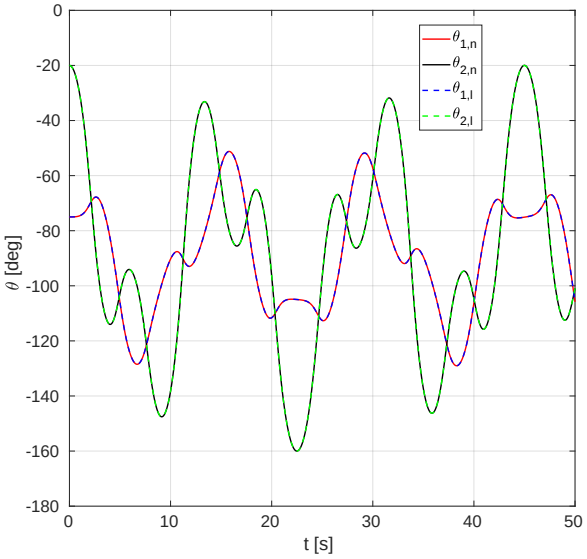

Figure 3.9: Simulation of the double pendulum (Table 3.6) oscillation using the models derived with Lagrange method (l) and with Neustadt method (n) (IC from 3.7).

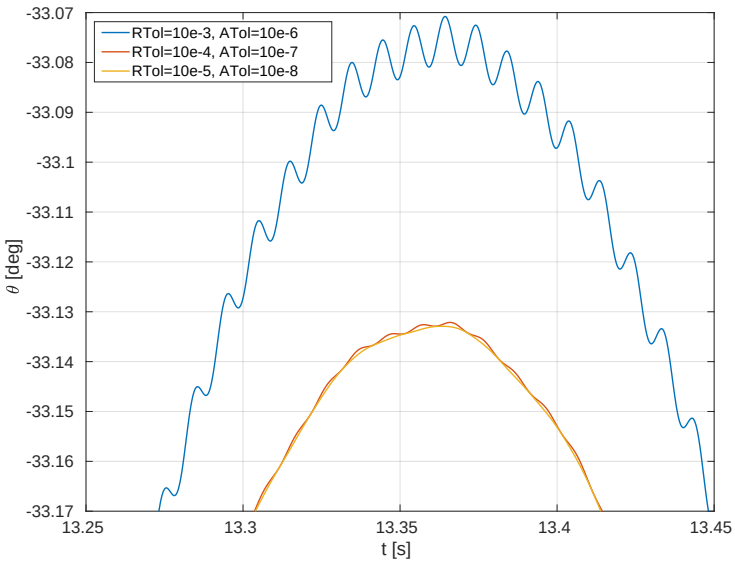

Figure 3.10: Influence of different tolerances on the result of the propagation of the Neustadt double pendulum model (zoom for the same simulation as in Figure 3.9).

when propagating the trajectory of the Neustadt model, each bar of the pendulum moves independently so that, if the propagation stepsize is too large, then the two elements move apart too much during one step and the resulting elastic force, that is assumed to be constant during the integration step, will be really large and will exert on the bars a force that does not correspond at all to the reality. Indeed, depending on the rigidity of the spring and on the mass and geometric properties of the rigid elements of the system, there exists a minimum optimal stepsize that can reproduce the real vibrations of the system caused by the elastic connection. In general, if the pseudo spring is very rigid and the elements have low mass, the reproduction of the resulting small vibrations of the system is only possible with stringent tolerances. Figure 3.10 shows how the propagator tolerances influence the trajectory of the bars and the amplitude of vibrations due to the presence of the pseudo springs.

Another drawback of the Neustadt methodology is that the initial conditions need to be specified for each state vector element of each body in the system. This is because with Neustadt each component of the multi-body moves independently and the constraint forces are determined indirectly through the elongation of the

pseudo springs caused by the bodies moving apart one with respect to the others. In addition to this, the initial conditions have to be really accurate, especially for the case of pseudo springs with very large elastic constant k, because otherwise the elastic force at the beginning of the propagation is so large that it causes it to diverge.

From the discussion above, it clearly emerges that the Neustadt methodology is outperformed by the other classical multibody mechanics approaches when computational efficiency, accuracy and robustness represent a main requirement. Also, the presence of the vibrations caused by the pseudo spring approximation, especially for the case in which rigid connections have to be modelled, causes a loss in accuracy and robustness of the model because an unexpected disturbance could cause an excessive elongation and, in turn, large inaccuracies in the propagation. Finally, the facts that for each propagation step the evolution of every single state vector component has to be evaluated, and that for achieving good accuracy this step needs to be very small, are responsible for a significant decrease in numerical efficiency.

On the other hand, there are cases in which the Neustadt approach represents a convenient choice. Indeed, the fact that one does not need to deal with energy functions, constraint forces or matrix operations, but only rigid body mechanics, is a significant advantage when time constraints are stringent and accuracy, robustness and computational efficiency are not the main concern. This is the case, for example, during feasibility studies, where the designer is requested to quickly evaluate the influence of multiple parameters on a certain aspect of the mission that has not been explored yet, and decide whether to invest time and money to study that aspect in more detail. This is the case of the present research, where the aim is to evaluate whether the use of thrust for controlling the horizontal position of the spacecraft during the parachute descent can significantly contribute to the size reduction of the final landing ellipse on Mars in an efficient way, with particular attention for the dynamic stability properties of the system. Another advantage of using the Neustadt approach is that it allows one to use the same framework already developed for the rigid body model introduced in Section 3.2. This will thus represent the starting point for realizing the following parachute-backshell-payload multibody model. Also, integrating this model with the GNC system that will be developed in Chapter 7 is straightforward. These aspects, together with the possibility to add something innovative to the present work, are the main reasons that make the development of a new multibody system based on the methodology of Neustadt more appropriate with respect to other choices, in particular the use of the model of Abdulkadir [2011] based on the Wittenburg [2008] formalism, for the purpose of this study.

3.3.2. DESCENT SPACECRAFT MULTIBODY DYNAMICS

In this section the characteristics of the multibody model derived using the method of Neustadt for simulating the dynamics of a parachute-backshell-payload spacecraft descending through the atmosphere of Mars and the resulting EOM will be introduced and briefly discussed.

As for the rigid body model, also the multibody model will exclusively reproduce the motion of the spacecraft in a single plane perpendicular to the surface of Mars. In fact, for dynamic stability study purposes, the rotational symmetry of the system allows to introduce this simplification without loss of relevant information. The model will thus be 2D and, considering that the rotation about the symmetry axis is neglected and that the Neustadt approach does not imply a reduction of DOF for the multibody system, it will have 9 DOF.

The aerodynamics of the backshell and payload, analogously to Section 3.2, are neglected also in this case. In fact, the weight of the payload and the aerodynamic forces of the parachute dominate the dynamics of each single body element. This is because even if they do not act directly on a certain element, they are transmitted through the risers and are present in the form of elastic force.

The risers, connecting the parachute with the backshell and the backshell to the payload, are each modelled as massless springs. Also, the parachute, backshell and the payload are assumed to be rigid bodies. Each of them features its own body frame B centred in the respective COM. The parachute is assigned subscript 1, the backshell subscript 2 and the payload subscript 3. For simplicity reasons, this notation will be used in the following for indicating the gravitational masses and moments of inertia around the respective X_B-axes and other parameters related to the specific elements of the spacecraft.

To write the EOM for the multibody model we can refer to Figure 3.11 while the angle convention, also for the attitude angles of the risers, and all the X-axes are analogous to those for the rigid body system in Figure 3.5. The only differences between the rigid and multibody models are the fact that for the latter each of the spacecraft elements has its own state vector components y, z and θ, and that it is characterized by the presence of the elastic forces. Considering these, the EOM in the inertial reference frame I for each of the body elements are:

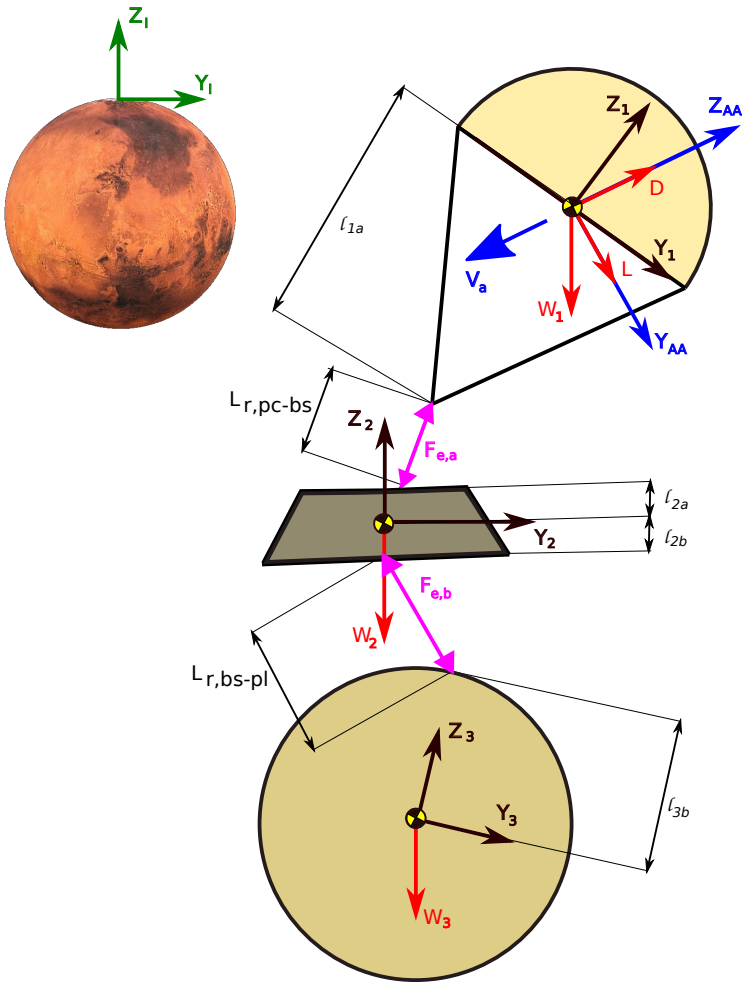

Figure 3.11: Parachute-backshell-payload spacecraft multibody model dynamic analysis.

$$
\begin{aligned}
\ddot{y}_1 &= \frac{-D\cos\gamma - L\sin\gamma - F_{e,a}\cos\theta_{r,a}}{m_1 + m_a} \\
\ddot{z}_1 &= \frac{g m_1 - D\sin\gamma + L\cos\gamma - F_{e,a}\sin\theta_{r,a}}{m_1 + m_a} \\
\ddot{\theta}_1 &= \frac{-D\sin\alpha z_{\mathrm{COP}} - L\cos\alpha z_{\mathrm{COP}} + M - F_{e,a}\sin\left(\theta_{r,a} - \theta_1\right) l_{1a}}{I_1 + I_a}
\end{aligned}
$$

$$
\begin{aligned}
\ddot{y}_2 &= \frac{F_{e,a}\cos\theta_{r,a} - F_{e,b}\cos\theta_{r,b}}{m_2} \\
\ddot{z}_2 &= \frac{g m_2 + F_{e,a}\sin\theta_{r,a} - F_{e,b}\sin\theta_{r,b}}{m_2} \\
\ddot{\theta}_2 &= \frac{-F_{e,a}\sin\left(\theta_{r,a} - \theta_2\right) l_{2a} - F_{e,b}\sin\left(\theta_{r,b} - \theta_2\right) l_{2b}}{I_2}
\end{aligned}
\tag{3.61}
$$

$$
\begin{aligned}
\ddot{y}_3 &= \frac{F_{e,b}\cos\theta_{r,b}}{m_3} \\
\ddot{z}_3 &= \frac{g m_3 + F_{e,b}\sin\theta_{r,b}}{m_3} \\
\ddot{\theta}_3 &= \frac{-F_{e,b}\sin\left(\theta_{r,b} - \theta_3\right) l_{3b}}{I_3}
\end{aligned}
$$

In Eq. (3.61), $F_{e,a}$ is the magnitude of the elastic force generated by the pseudo spring between the parachute and the backshell, $F_{e,b}$ the magnitude of the elastic force generated by the pseudo spring between the backshell and the payload, $\theta_{r,a}$ and $\theta_{r,b}$ their respective attitude angles (defined with resect to the the I-frame) and l_{1a}, l_{2a}, l_{2b}, l_{3b} the distances between the anchorage point of the connection (a or b) on the body and the COM of the body (1, 2 or 3). Also in this case, following the Neustadt approach, the magnitude and direction of the forces generated by the pseudo springs can be determined by calculating the inertial position of the hinges at each integration step. The position vectors for the hinges a and b connecting bodies 1,2 and 3 are:

$$\begin{aligned}
\mathbf{h}_{1a} &= \begin{pmatrix} y_1 + l_{1a}\cos\theta_1 \\ z_1 + l_{1a}\sin\theta_1 \end{pmatrix} \\
\mathbf{h}_{2a} &= \begin{pmatrix} y_2 - l_{2a}\cos\theta_2 \\ z_2 - l_{2a}\sin\theta_2 \end{pmatrix} \\
\mathbf{h}_{2b} &= \begin{pmatrix} y_2 + l_{2b}\cos\theta_2 \\ z_2 + l_{2b}\sin\theta_2 \end{pmatrix} \\
\mathbf{h}_{3b} &= \begin{pmatrix} y_3 - l_{3b}\cos\theta_1 \\ z_3 - l_{3b}\sin\theta_1 \end{pmatrix}
\end{aligned} \tag{3.62}$$

The elongation of the elastic connections and their orientation, determining respectively the magnitude of the force and its direction, are:

$$\begin{aligned}
\begin{pmatrix} \rho_a \\ \theta_{r,a} \end{pmatrix} &= \texttt{cart2pol}(\mathbf{h}_{2a} - \mathbf{h}_{1a}) \\
\begin{pmatrix} \rho_b \\ \theta_{r,b} \end{pmatrix} &= \texttt{cart2pol}(\mathbf{h}_{3b} - \mathbf{h}_{2b})
\end{aligned} \tag{3.63}$$

so that:

$$\begin{aligned}
F_{e,a} &= -k_a\left(\rho_a - L_{\text{r,pc-bs}}\right) \\
F_{e,b} &= -k_b\left(\rho_b - L_{\text{r,pc-bs}}\right)
\end{aligned} \tag{3.64}$$

in which $L_{\text{r,pc-bs}}$ and $L_{\text{r,bs-pl}}$ are the nominal lengths of the risers and k_a and k_b the corresponding pseudo springs elastic constants. While for most of the vehicle parameters in Eq. (3.61) it is possible to reuse the values defined for the MPF reference case already introduced in Section 3.2.3 for the rigid body model, some others need to be specifically defined for the multibody model.

The elastic constants of the risers k_a and k_b can be chosen according to an accurate literature research, aimed at determining their material and geometric properties. However, by running some sample simulations with realistic values for these parameters it has been verified that the elasticity of the riser has a negligible effect on the attitude and position of the spacecraft. This aspect is indeed more relevant for the study of the vibrations that affect the system during the flight. Because of this, for the purpose of the present study it is more straightforward to choose a value for k_a and k_b that is simply consistent with the physical expectations. In particular, we assume very rigid risers with $k_a = k_b = 200000$ N/m.

By studying the behaviour of the rigid body model it has been verified that the variation of the parachute COP position does not really influence the dynamics of the system. This is why for the multibody model z_{COP} is assumed to be fixed and equal to the projection of the suspension lines on the parachute rotational symmetry axis. Also, the riser nominal lengths, in agreement with the data given in Section 2.5, are set to $d_{n,a} = 0$ m and $d_{n,b} = 5$ m.

Finally, we need to determine the distance of the hinges with respect to the COM of the elements of the spacecraft. In particular, the hinge of the upper riser with respect to the parachute COM also corresponds to the projection of the suspension lines on the parachute rotational symmetry axis. The COM of the backshell is instead 0.5 m distant from the upper hinge and 1 m distant from the lower hinge. Finally, the payload COM is 2 m distant from its upper hinge. It is remarked that the y-coordinate of the hinges positions in the respective body frames is always 0 (the hinges are along the Z_B-axes of the spacecraft elements). These distances are not exact but are reasonable and consistent with the geometric data available.

4

MARS ENVIRONMENT

Mars is the last terrestrial planet in our Solar System per distance from the Sun. It has a mean radius of 3389.5 km and a mass of 6.4185×10^{23} kg. Some of the features of this planet include the presence of water-ice and a thin atmosphere, as well as the fact that it is in the habitable zone of the Sun. Because of this, the first missions to the Red Planet were designed, amongst others, to search for evidence of life on its surface, but they had no success in this. Still, it is possible that Mars can support life, reason why a lot of research effort is being done to land the first man on it. This chapter summarizes all the information for characterizing and modelling the environment of Mars. However, some more detailed information can be found in Lissauer and de Pater [2013], that discusses all the physical aspects of the planet, and Haberle et al. [2017], that focuses on describing the processes taking place in its atmosphere.

The color of Mars is due to the presence of rust, Fe_2O_3, in the rocks of the surface. Its hemispheres are not equal: the north is smoother, while the south is characterized by craters and is, in part, 3 to 4 km high over the nominal surface level. Mars is characterized by the presence of water geological formations, indicating that in the past liquid water was present on it, and of the highest mountain of the Solar System, the Olympus Mons, extending 27 km over the geoid, this being possible thanks to the low gravity and low lithosphere temperature.

Mars' magnetic field is really tenuous and is caused by residual magnetism of the rocks of the crust. This magnetic field, coupled with the ionospheric pressure, is sufficient to protect the planet from the solar wind. However, these two effects are negligible in flight dynamics applications. In fact, the motion of the spacecraft during the parachute descent is dominated by the aerodynamic and gravity forces and moments. The aerodynamic forces depend, amongst others, on the atmospheric density ρ and on the airspeed of the vehicle that is influenced by the wind conditions on the planet. These topics are discussed in Section 4.1. The gravitational acceleration g, determining the gravity force, changes as a function of the position of the spacecraft in the sphere of influence of Mars. A model describing this variation that is appropriate for the purpose of the present study will be discussed in Section 4.2.

4.1. MARS ATMOSPHERE

The atmosphere of Mars is very thin with respect to the atmosphere of the Earth. It is a mixture of 95% CO_2, 3%N_2, Ar, CO and H_2O. At the surface the mean pressure is 6 mbar, about the 0.6% of the corresponding value on Earth. This pressure is below the saturation pressure for liquid water at 215 K, that is the mean surface temperature, so that water can be present either as vapour or ice. Over the equatorial regions, at about 10 km of altitude, formation of water-ice clouds is possible, while at 50 km, where the temperature is about 150 K, CO_2-ice clouds take shape.

During the parachute descent phase, the spacecraft is subjected to the winds taking place in the so called planetary boundary layer, corresponding to the atmosphere band between the surface and an altitude of 10 km. In here, the pressure gradients originating winds depend on a number of factors. The temperature gradients are the most relevant. The fact that the atmosphere of Mars is tenuous implies that it is really sensitive to solar heating and so the day-night thermal excursion is large. Temperature ranges from 130 K in the night to 300 K during daytime. This causes the thermal tide winds, strong winds across the day-night line. Other factors include the friction of the atmosphere with the surface of the planet and the Coriolis force due to its rotation. Depending on how these contributions influence each other, however, it is possible to have different types of

wind phenomena that cause the vehicle to drift away from its nominal trajectory. Because of this, they need to be taken into account when designing a Mars landing spacecraft. For example, the deployment conditions for the parachute, representing the target for the hypersonic entry phase, are chosen according to the available estimation of the wind profile in the landing zone. In fact, if the parachute descent is passive, then from the deployment to the ignition of the terminal descent thrusters there is no possibility to counteract the wind drift effect. For the Phoenix mission, about 2000 atmosphere situations for the landing site area were modelled and simulated before to choose an appropriate landing target.

According to Prince et al. [2008], for the stripe between latitudes 65° and 72°, vertical winds have an average speed of 10 m/s up to an altitude of 7 km and 5 m/s between 7 and 25 km, but can eventually reach values as high as 20 m/s after this point. These winds can cause shifts in mission schedule as well as an increase in fuel consumption for the terminal descent. The horizontal winds are instead more homogeneous all over the considered altitude range, with a mean value between 5 and 10 m/s but can reach peaks of 40 m/s over the whole altitude range of interest 0-25 km. They contribute significantly to the landing position error and disturb the attitude behavior of the parachute-payload system. In general, winds from the surface to ≈10 km are really variable in direction as well as in magnitude. Kaas et al. [2003] estimated the 1σ wind velocities over the entire planet to be around 20-30 m/s. Another example is wind data from the Mars Exploration Rover Gusev landing site (14.5°S, 175.4°E) reporting a mean wind velocity of 15 m/s with a 1σ uncertainty of 12 m/s.

The factors described earlier influencing the mechanics of the atmosphere of Mars can also result in the atmospheric turbulence phenomenon. Turbulence is by definition a flow regime characterized by chaotic changes in pressure and flow velocity. It is in contrast to a laminar flow regime, which occurs when a fluid flows in parallel layers, with no disruption between those layers. Despite being always governed by the same equations, turbulence on Mars can take place at different scales, depending on the size of the vortexes, called eddies, that determine it. The eddies exchange between each other viscous energy according to the mechanics of the energy cascade.

If the turbulence phenomenon takes place on a planetary scale it is referred to as atmospheric turbulence and causes chaotic movements of large air masses within the atmosphere of a planet that are analogous, from the point of view of the influence they have on the descent trajectory, to the other wind phenomena described earlier.

By progressively considering smaller scales of atmospheric turbulence vortexes, we have the gusts. Gusts are indeed unpredictable flows of air that invest the vehicle in a specific and limited altitude band and can be caused by the turbulence phenomenon. When instead the scale of the eddy is more or less comparable to the characteristic length of the spacecraft then we speak about turbulent wind. In this case the wind speed profile is irregular. Gusts and turbulent winds are mainly relevant for the dynamic stability of the vehicle, because they cause dangerous oscillations that have to be damped.

These considerations and data have served to give an idea of what the descent spacecraft has to face during an EDL mission on Mars. They will be taken into account in the following for the definition of a model that can simulate the aspects of the atmosphere of the Red Planet that are relevant for our study.

4.1.1. MARS ATMOSPHERE MODEL

For modelling the atmosphere of Mars several options are available. One of these consists of using the European Mars Climate Database (EMCD) Version 5.2 introduced by Millour et al. [2015], available from March 2015. This database has been realized according to the General Circulation Models (GCM) developed by Forget et al. [1999] and has been validated using both orbiter and lander measurements. It is mainly employed in EDL studies for future missions, investigation of specific Martian issues and analysis of observations. The model yields many meteorological variables, including temperature, density, pressure, winds, atmospheric composition and others, for different altitudes, epochs and coordinates. The second option consists instead of using tables that give the values of the relevant atmospheric variables, namely the wind speed, density, pressure and temperature, according to a precise altitude grid. The value of a certain atmospheric variable for an arbitrary altitude can then be determined by interpolation. The values in the table can be specific for a mission epoch and location or could be derived by averaging measurement data from different missions. Finally, the third option consists of using a simpler model for determining sample temperature and density profiles as a function of the altitude over Mars and model the wind phenomena we need for the study, i.e., constant wind, gusts and turbulence, independently.

The use of the EMCD or tables gives the possibility to accurately simulate different atmospheric conditions that the spacecraft could face on Mars. On the other hand, using a model that gives the atmospheric variables

as simple functions of the altitude is more computationally efficient. This option is also more appropriate if analytical consideration about the dynamics of the system have to be made, considering that the analytical formulas can eventually be included in the EOM. In addition, we not need to simulate the exact atmospheric conditions that the spacecraft will encounter on Mars. In fact, by analysing the response of the system to each atmospheric perturbation separately, we can evaluate the performance of the guided descent system and its dynamic stability properties much more effectively. Considering these, the third option is assumed to outperform the others with respect to the purpose of the present project.

The temperature and density profiles can be described with the model[1] that NASA uses for preliminary studies and in particular for aerodynamics and thermodynamics simulations. It was developed according to the atmospheric data gathered by the orbiter Mars Global Surveyor in April 1996 and is the model that is also used in the `FoilSim` [2] simulator. According to this model we have:

$$\begin{aligned} p &= 0.699 - \exp(-0.00009h) \\ T &= \begin{cases} -23.4 - 0.00222h & \text{for } h > 7000 \text{ m} \\ -31 - 0.000998h & \text{for } h < 7000 \text{ m} \end{cases} \\ \rho &= \frac{p}{0.1921\,(T + 273.1)} \end{aligned} \tag{4.1}$$

in which the altitude h is in m, the temperature T in C°, the pressure p in KPa and the density ρ in $\frac{\text{kg}}{\text{m}^3}$. To include the effect of wind speed in the dynamic description of the system, it is sufficient to calculate the airspeed of the vehicle $\mathbf{V}_a$, that in turn determines its angle of attack α, as:

$$\mathbf{V}_a = \mathbf{V}_g - \mathbf{V}_w \tag{4.2}$$

where $\mathbf{V}_g$ and $\mathbf{V}_w$ are, respectively, the ground speed and wind speed vectors in the chosen reference frame. While for a simple wind the wind speed vector has constant components, the profiles for gusts and turbulences are modelled as described respectively in Sections 4.1.2 and 4.1.3.

For using the atmosphere model described here in a simulation environment, at each propagation step the state of the vehicle is given in input to the function implementing it. The relevant state vector elements are then used to calculate the corresponding density, temperature and pressure using Eq. (4.1) and the wind speed according to the corresponding perturbation wind speed profile.

4.1.2. WIND GUSTS

While descending through the atmosphere of Mars it is possible that the spacecraft encounters a wind gust. Wind gusts are critical, particularly at low altitude, because they may cause dangerous oscillations of the elements of the parachute-payload system that require time to damp out. The response to a wind gust can yield valuable information with respect to the stability of the parachute-payload system. As introduced earlier, wind gusts are present in the atmosphere of Mars in the altitude range 0-10 km. A wind gust phenomenon consists of an increase of wind velocity, up to 30 m/s for Mars, having short duration, typically lower than 10 s. The gust causes the wind speed to vary. With respect to the inertial frame I fixed to Mars defined in Section 3.1, the wind speed vector is defined as:

$$\mathbf{V}_{w,I} = \begin{pmatrix} V_{w,I,1} \\ V_{w,I,2} \\ V_{w,I,3} \end{pmatrix} \tag{4.3}$$

where each component $V_{w,I,i}$ for $i = 1,...,3$ can be modelled as a function of the altitude h. To do so we need to define some parameters. These are the altitudes where the gust begins, h_i, and where it ends, h_e, the transient size Δh_t and the wind gust vector:

$$\mathbf{V}_{gu} = \begin{pmatrix} V_{gu,1} \\ V_{gu,2} \\ V_{gu,3} \end{pmatrix} \tag{4.4}$$

[1] More info about this model can be found at https://www.grc.nasa.gov/www/k-12/airplane/atmosmrm.html. Last accessed: 28/01/2018.

[2] More details about about `Foilsim` are available from https://www.grc.nasa.gov/www/k-12/airplane/foil3.html. Last accessed: 28/01/2018

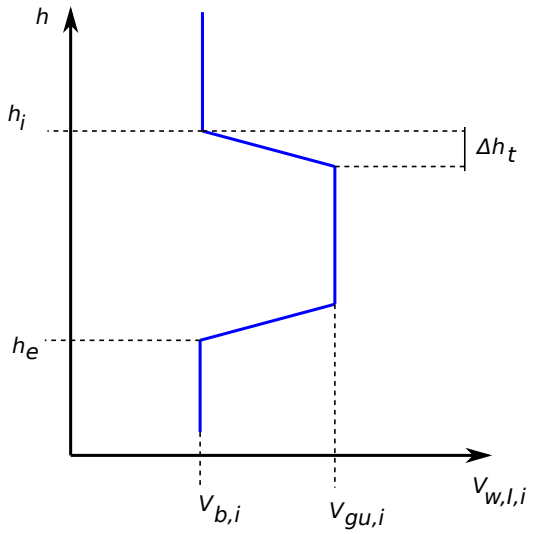

Figure 4.1: Sample gust profile.

that represents the difference between the maximum velocity of the air in the gust band and the background wind speed, that is:

$$\mathbf{V}_b = \begin{pmatrix} V_{b,1} \\ V_{b,2} \\ V_{b,3} \end{pmatrix} \tag{4.5}$$

To model the gust profile as shown in Figure 4.1, the atmosphere can be ideally divided in five different regions. Considering a descending spacecraft, the first region it finds is the one before the gust where there is only the constant background wind (that clearly can eventually be null). At a certain altitude the vehicle encounters the gust. At this point the speed of the air does not suddenly assume the maximum gust speed. It is possible to model this interface, that is the transient, as the velocity of the air increases linearly at a constant rate. For the component i of the gust speed this rate is given by $\frac{V_{gu,i}}{\Delta h_t}$. At the end of the transient region the air velocity is constant and equal to $V_{gu,i}+V_{b,i}$. A second transient phase is experienced at the end of the gust band and here the air velocity decreases at a constant rate $\frac{V_{g,i}}{\Delta h_t}$. After this second transient the air speed is once more equal to the background wind speed. For a single component of the wind speed, mathematically we have:

$$V_{w,I,i} = \begin{cases} V_{b,i} & \text{for } h > h_i \\ V_{b,i} + \dfrac{V_{gu,i}}{\Delta h_t}(h_i - h) & \text{for } h_i - \Delta h_t < h < h_i \\ V_{b,i} + V_{gu,i} & \text{for } h_e + \Delta h_t < h < h_i - \Delta h_t \\ V_{b,i} + V_{gu,i} - \dfrac{V_{g,i}}{\Delta h_t}(h_e + \Delta h_t - h) & \text{for } h_e < h < h_e + \Delta h_t \\ V_{b,i} & \text{for } h < h_e \end{cases} \tag{4.6}$$

While short horizontal wind gusts are particularly dangerous for the attitude of a parachute-payload system descending vertically in the atmosphere, a vertical gust is not critical from this point of view because the relative motion of the elements of the spacecraft is constrained along this direction. Oblique gusts can be seen as the composition of an horizontal and a vertical gust and do not give yield any additional information with respect to the dynamic properties of the system. This is why in Chapter 8 the stability of the system will be tested with horizontal gusts. According to the wind data introduced earlier, the reference gust is assumed to happen between the altitudes 4000 m and 3900 m and have a speed of 20 m/s with a transient of 10 m. This short gust is particularly appropriate for flight dynamics analysis since the attitude of the spacecraft is sensitive to the impact of the gust and not really to its duration. Also, a larger transient size causes the impact of the gust on the system to be less critical so that the smaller this parameter is the more conservative the results will be.

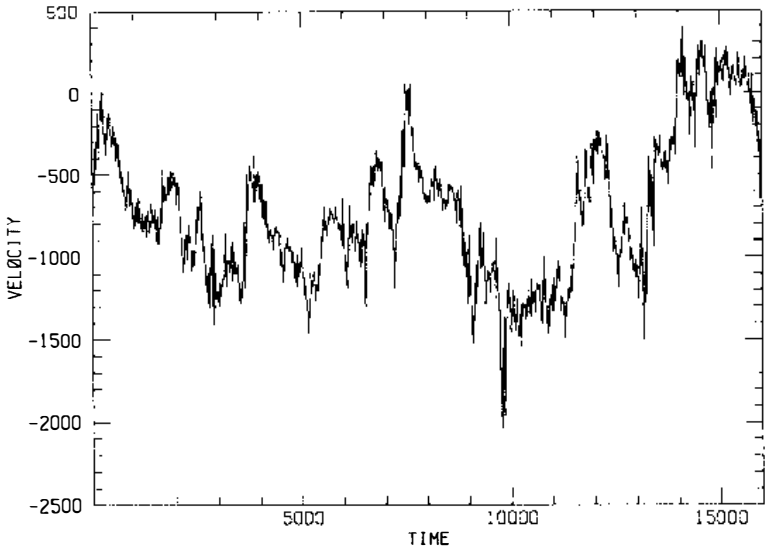

Figure 4.2: Turbulent velocity signal measured using standard hot-wire anemometry 18 m above the ground in an atmospheric surface layer plotted in arbitrary units of time and velocity [Sreenivasan, 1991].

4.1.3. ATMOSPHERIC TURBULENCE

The most commonly used models for simulating turbulence in flight dynamics applications are the von Karman and Dryden models, that have been specifically designed for simulating turbulence on Earth. A model developed for engineering applications simulating the turbulence in the atmosphere of Mars is unfortunately not available. However, for testing the stability properties of our spacecraft, it is sufficient to simply reproduce the characteristics of the turbulent flow that are relevant for the study of this aspect.

A turbulent flow is characterized by an irregular velocity profile. By looking at the sample profile depicted in Figure 4.2, one notices that it is characterized by several superimposed pseudo-oscillating trends. Each of these trends, that represent the different scales of the turbulence, features a certain frequency. The dynamic response of the spacecraft will be different per each of these frequencies. Considering this, a straightforward approach for evaluating how the spacecraft behaves in case of turbulence consists of testing its response using sinusoidal turbulent wind speed profiles with different frequencies. A single wind speed component in the I frame will thus be defined as:

$$V_{w,I,i} = A\sin(\omega t) \tag{4.7}$$

where A is the amplitude of the turbulence wind speed profile and ω its frequency.

The turbulent profile given by Eq. (4.7) expresses the variation of the wind speed as a function of time and not of the altitude, as one could expect. In fact, as explained earlier, the turbulence is due to the eddies that have a precise spacial dimension. With this approach, however, ω is the input frequency that the spacecraft senses independent of its velocity while it passes through the perturbation. In this way the results that we will get from the turbulence response analysis will be less dependent on the state of the vehicle and will have a more general validity.

Now we need to determine the amplitude, A, and frequency, ω, of the sinusoidal signal. These depend to the characteristics of the atmosphere of Mars. According to Haberle et al. [2017] the standard deviation σ for the turbulence in the planetary boundary layer is 2.4 m/s for both the horizontal and vertical velocity components. This value can be used as amplitude A of the periodic signal.

The turbulence frequency ω, for the reasons introduced earlier, is not a unique value. It varies within a frequency spectrum whose extremes need to be defined. The smallest scale of the vortices that can be found in a turbulent flow is determined by the constant η, called Kolmogorov length scale, that for Mars varies between 7 mm and 2 cm. This value can be used to determine the maximum frequency that the turbulent velocity profile signal can have, that is the inverse of the Kolmogorov time scale τ_η defined by Pope [2000] as:

$$\tau_\eta = \left(\frac{\nu}{\epsilon}\right)^{\frac{1}{2}} \tag{4.8}$$

in which the kinematic viscosity the atmosphere of Mars ν, according to Petrosyan et al. [2011], is 10^{-3} m^2/s and the average rate of dissipation of turbulence kinetic energy per unit mass ϵ can be determined by inverting the equation for the Kolmogorov length scale that, once more according to Pope [2000], is:

$$\eta = \left(\frac{\nu^3}{\epsilon}\right)^{\frac{1}{4}} \tag{4.9}$$

The resulting maximum turbulence velocity profile signal frequency, corresponding to the smaller possible size of the eddies 7 mm, is thus 40.82 Hz. The lower extreme for the desired frequency spectra, instead, cannot be derived from physical considerations. Because of this the response of the system will be tested with decreasing frequencies until the point in which the effect of turbulence is negligible with respect to its attitude dynamics.

Also in this case, for reasons analogous to those introduced for the gust, only the response of the system to the horizontal component of the turbulence will be tested. This is in fact the most critical for the attitude stability of the system.

4.2. MARS GRAVITY FIELD

The Mars gravity field is much less strong than that of the Earth. At surface level it has an acceleration of about 3.7 m/s^2, less than half of the corresponding value on Earth. For modelling it, several possibilities are available. The most accurate option is to use the gravity potential model. According to Mooij [2015], in this case the gravitational potential U, from which the gravitational acceleration vector can be derived, may be expressed as the summation of a central field term, that is a mass-symmetric body, and a correction term for the Mars' non-symmetric mass distribution. In particular, this correction term depends on a series of coefficients describing each a particular feature of the distribution of the mass of Mars.

The gravity potential model yields a very accurate description of the gravity field of Mars and represents the most appropriate choice in case of accurate EDL simulations aimed, for example, at the prediction of the landing site. On the other hand, however, the effect of the force variation due to the correction term on the dynamic stability of the spacecraft is absolutely negligible with respect to the aerodynamic forces of the parachute, the weight of the payload due to the central field term and the propulsion force generated by the backshell thrusters. With respect to the purpose of the present study, the inclusion of the correction term would cause a increase in complexity and average CPU time of the software package without improving the validity of the results. Also, keeping only the central field term still gives the possibility to take into account the variation of the gravitational acceleration with the altitude with respect to the surface. Finally, the resulting formula for the gravitational acceleration, that is the classical inverse square law, is simple enough to be used for analytical investigation. With respect to the inertial frame I fixed to Mars defined in Section 3.1.2, the gravitational acceleration vector can be defined as:

$$\mathbf{g}_I = \begin{pmatrix} 0 \\ 0 \\ -\frac{\mu_M}{(R_M+z)^2} \end{pmatrix} = \begin{pmatrix} 0 \\ 0 \\ g \end{pmatrix} \tag{4.10}$$

where z is the altitude over the surface of Mars, μ_M=4.282837×10^{13} m^3/s^2 and R_M=3389500 m. For convenience, g can be used to indicates the vertical component of the gravitational acceleration vector.

5

SOFTWARE VERIFICATION AND VALIDATION

The dynamic models developed in Chapter 3 need to be implemented in a software package and integrated with the Mars environment and GNC system models. The software architecture and the tools to realize a working parachute descent simulator are discussed in Section 5.1. In Section 5.2, instead, the functions of the software and the the rigid body and multibody dynamic models introduced earlier will be verified.

5.1. SOFTWARE ARCHITECTURE AND TOOLS

Figure 5.1 shows the architecture of the Matlab software used for simulating the parachute descent of the parachute-backshell-payload spacecraft modelled as a multibody system. By looking at it, it is easy to notice four main blocks that are the *environment*, *vehicle dynamics*, *GNC* and *output*. The *environment* block, according to the characteristics of the atmosphere and gravity field described in Chapter 4, determines the wind speed, air density and gravitational acceleration as a function of the state of the vehicle. It this way its response can be tested with different atmospheric perturbations depending on the input from the *simulation manager*. The *environment* block is recalled after every step of the *integrator* function that integrates the *equations of motion* defined inside the *vehicle dynamics* block. The dynamic contributions determining the balance expressed by the *equations of motion* are the *aerodynamic forces*, that depend on the *airspeed* vector and the *parachute aerodynamics*, the *gravity forces*, the *elastic forces* due to the *elongation* of the risers connecting the spacecraft elements and the thrust force generated by the *GNC* system. Also, the added mass effect influences the inertia properties of the vehicle. The *GNC* block takes in input the state, simulates the estimation inaccuracy of the *navigation* by adding to it a random error (calculated according to a certain standard deviation), and computes the thrust command according to its *position-velocity target* and to the characteristics of the *guidance* algorithm. The trajectory resulting from the propagation is then taken in input by the *output* block that, after *post processing* operations, produces significant *data* and *graphs*. The software based on the rigid body model is analogous, the only difference being that no elastic forces appear in its dynamics.

The software environment chosen for the development of the simulator is `Matlab R2017a`. In fact, if the software is implemented in `Matlab` a number of useful built-in functions and toolboxes, such as the Aerospace and Control Systems Toolboxes, can be exploited to increase the productivity and save time. One example is the `ode45` integrator implementing a Runge-Kutta integration routine. This function is built-in in `Matlab` and has been used in the simulator for propagating the spacecraft dynamics. In addition to this, the `Matlab` proprietary language is simple and appropriate for engineering research purposes. The debug features of `Matlab`, also, are very well performing and versatile. The only drawback is that, in general, a `Matlab` software is less efficient than, for example, a `C++` or `Fortran` software, but the development time in the first case is significantly lower and for the present study the advantage of a more efficient code is not a key requirement.

The process to develop the software has followed the *Waterfall* model. The requirement definition and software design phases, completed during the literature study period, have been followed by the coding, debugging and verification of the several functions, that, afterwards, have been integrated. The final phase consisted of the system tests in Sections 5.2.2 and 5.2.3. Clearly, the first software to be developed was the one based on rigid body mechanics. To implement the multibody model, as already mentioned, only minor changes had to be applied to the whole code. This represents a direct advantage of using the Neustadt approach, because the dynamics of the multibody model is an extension of the dynamics of the rigid body system.

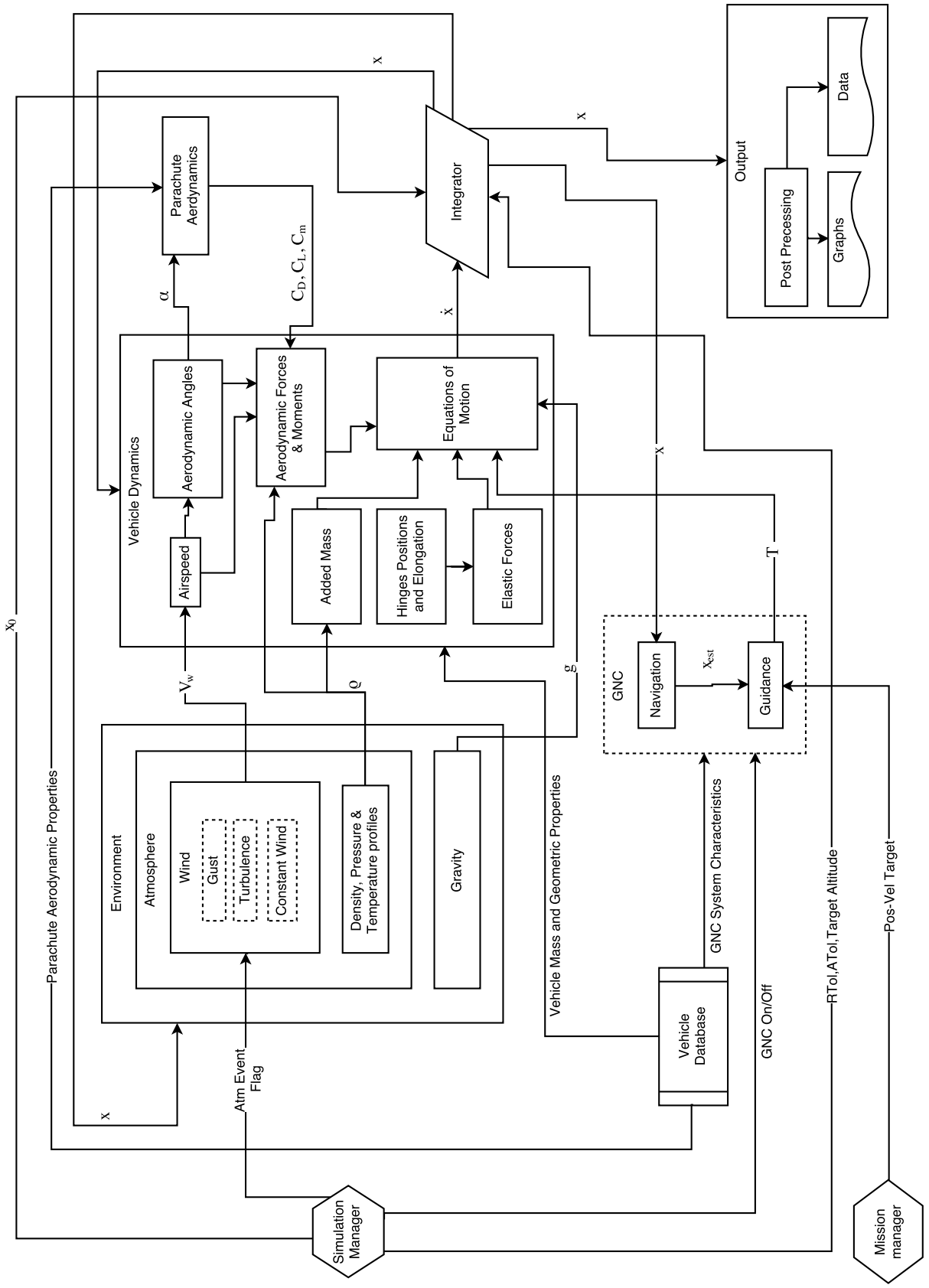

Figure 5.1: Parachute-backshell-payload descent simulator software architecture.

5.2. VERIFICATION

At this point of the research project we need to be sure that the models developed in Chapter 3 are valid and yield consistent results. In the following the verification of the units of software package are reported. Also, some reasoned system tests related to different aspects of the dynamics of parachute descent will be carried out. Their results will be discussed to determine whether they are consistent with the expectations. It is remarked that the results of Chapter 8 also prove the validity of the software since in any case they can be explained with physical considerations.

5.2.1. UNITS VERIFICATION

The dynamics of the spacecraft represents the core of the model and will be verified in the following sections. However, the physical consistency of the results that are produced by the software package also depend on the other units that it contains. In particular, the following unit tests were conducted and resulted to be successful:

Gust: this function, described in Section 4.1.2, was tested by checking that for a vertical sample flight subjected to a gust with chosen parameters, the wind speed profile as a function of the altitude showed the expected gust characteristics in agreement with Figure 4.1. The test was repeated using gusts with different parameters.

Turbulence: this function, described in Section 4.1.3, was tested by checking that, for a vertical sample flight subjected to a turbulent perturbation with precise amplitude and frequency, the wind speed profile as a function of the flight time was a sinusoid with the expected characteristics. The test was repeated with different turbulent signal amplitudes and frequencies.

Constant wind: this function was tested by checking that the horizontal wind causes the vehicle to drift away with respect to the vertical trajectory in the direction of the wind. The vertical wind has instead been tested by checking that a wind directed positively with respect to the Z_I-axis causes the descent time to increase, while the opposite happens for a vertical wind in the opposite direction.

Density (pressure, temperature) profile: this function was verified by checking that the values of the atmosphere density for certain sample points along a vertical descent trajectory, correspond to the values that can be calculated manually using Eq. (4.1).

Gravity field: this function was verified by checking that the values of the gravitational acceleration for certain sample points along a vertical descent trajectory, correspond to the values that can be calculated manually using Eq. (4.10).

Guidance unit: this function was verified by checking that the values of the thrust command for certain sample points along an arbitrary descent trajectory, corresponds to the values that can be calculated manually, for a certain state vector error and controller gains, using Eq. (7.16).

Added mass effect: this function was verified by checking that the added mass has a stabilizing effect on the dynamics of the system and that this effect, due to an increase in the inertial mass and moment of inertia of the parachute, is more significant as the altitude of the spacecraft decreases.

Parachute aerodynamics: this function was verified by checking that the coefficients given in output for a certain α correspond to the values that can be graphically obtained using Figure 3.6.

5.2.2. RIGID BODY MODEL VERIFICATION

The purpose of the present section is to validate the rigid body parachute-payload system mechanics introduced in Section 3.2. To do so we will design some tests and then verify that these are successful for the model to validate.

SYSTEM MECHANICS ANALYSIS IN VACUUM

This test will determine whether the dynamic evolution in vacuum of the system, modelled as a 3DOF rigid body, corresponds to the expectation. For this test we will assume that the atmosphere is absent, so that the spacecraft is exclusively subjected to the influence of the gravity force of Mars.

Consider now the translational motion of our rigid body. If no forces other than the gravity act on it, then the accelerations of the COM in horizontal and vertical directions, with respect to the inertial frame I, are:

$$\begin{cases} a_y = 0; \\ a_z = g_0; \end{cases} \tag{5.1}$$

where g_0 is the gravitational acceleration at the surface of Mars, and is constant and negative. The accelerations in Eq. (5.1) are constant and can easily be integrated to get the resulting $y-$ and $z-$velocities and position components as a function of time. We have:

$$\begin{cases} v_y = v_{y,0}; \\ v_z = v_{z,0} + g_0 t; \end{cases} \tag{5.2}$$

$$\begin{cases} y = y_0 + v_{y,0} t; \\ z = z_0 + v_{z,0} t + \frac{g_0 t^2}{2}; \end{cases} \tag{5.3}$$

Equations (5.2) and (5.3) represent the analytical solution for the trajectory of the spacecraft in vacuum with constant gravitational acceleration. This analytical trajectory has been compared to the numerically simulated one for different IC. The percentual error between the state variables is always smaller than $O(10^{-9})$. The two trajectories thus perfectly correspond.

If the spacecraft is not subjected to any force other than gravity, then there is no dissipative effect acting on the system and the total mechanical energy of the system E_{tot}, that is the sum of the kinetic translational energy $E_{k,t}$, the kinetic rotational energy $E_{k,r}$ and the potential energy $E_{p,g}$, where these terms are given by:

$$\begin{aligned} E_{k,t} &= \frac{m_g \, ||\mathbf{V}||^2}{2} \\ E_{k,r} &= \frac{I_{X_B} \dot{\theta}^2}{2} \\ E_{p,g} &= m_g g z \\ E_{\text{tot}} &= E_{k,t} + E_{k,r} + E_p \end{aligned} \tag{5.4}$$

must remain constant. This has been proven to be true for different numerically simulated trajectories. With respect to the rotational motion in vacuum an additional remark has to be made. In fact, if the system is exclusively subjected to gravity force, then there in no torque acting on it and the body keeps rotating at the same velocity it had at instant t_0. This is true only if one assumes that the gravitational acceleration is constant. If this is not true, then the gravitational acceleration gradient along the body generates a torque on it. However, the gravity gradient torque is is very small with respect to the aerodynamic forces that in the real case dominate the rotational equilibrium of the body and can be neglected.

EQUILIBRIUM CONDITION CONVERGENCE

Now that the motion in vacuum has been proved to be valid, we want to demonstrate that the system behaves as expected also in the real case, i.e., when the atmosphere is present. In particular, it is known by experience that the equilibrium condition for a parachute-payload system corresponds to the vertical flight, with a vertical velocity equal to the equilibrium velocity V_e. In this case, also, the system is oriented perpendicular to the ground with the payload below the parachute. So, we want to verify that, irrespective of the IC of the simulated trajectory, the following is true:

$$V_z \to V_e, \quad \theta \to -90^\circ, \quad \dot{\theta} \to 0, \quad \alpha \to 0 \tag{5.5}$$

where:

$$V_e = \frac{m_g g}{\sqrt{\frac{S_{\text{ref}}}{2} \rho C_{D,0}}} \tag{5.6}$$

Figure 5.2 shows that this test is successful because the system converges to its equilibrium position for different IC sets. Also, the delay time of the vertical velocity for the three cases is comparable, in the order of

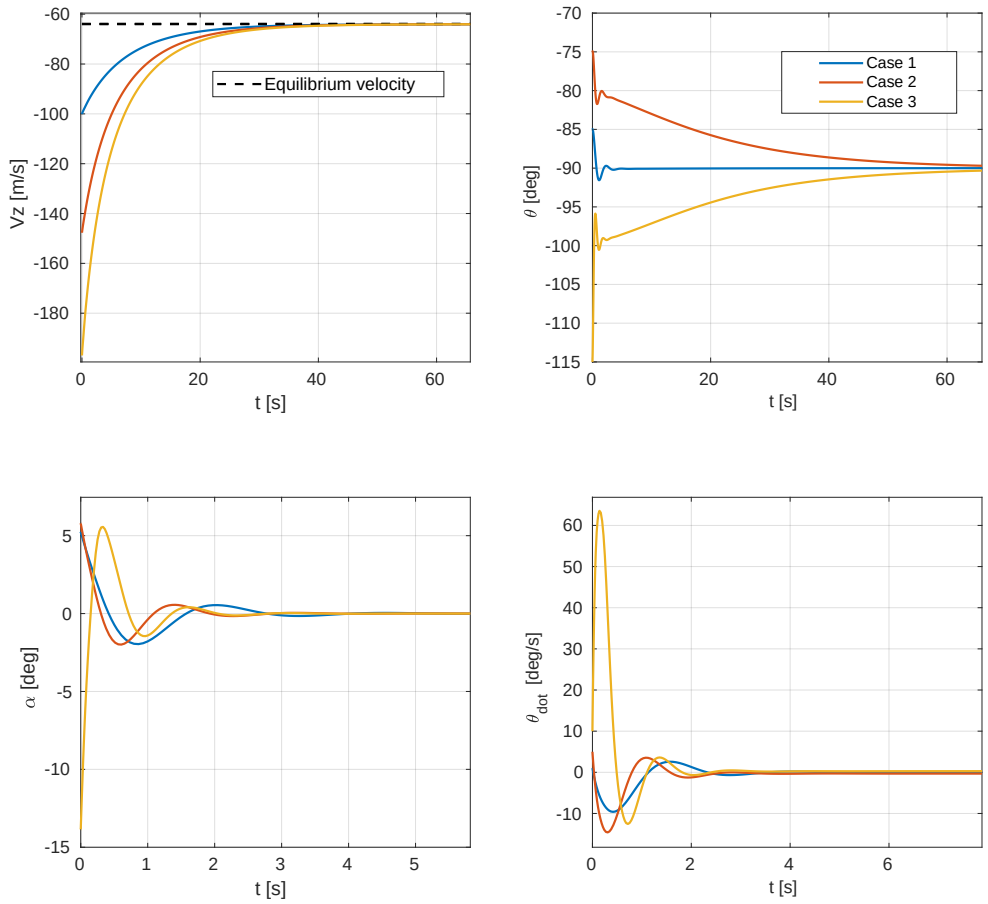

Figure 5.2: Convergence of the system to the equilibrium condition for different IC sets (from Table 5.1).

Table 5.1: IC for the test cases in Figure 5.2.

Parameter	Case 1	Case 2	Case 3
γ_0 [deg]	-90	-80	-100
θ_0 [deg]	-85	-75	-115
$\dot{\theta}_0$ [deg/s]	1	5	10
V_0 [m/s]	100	150	200

3 s, but not equal. The differences are due to the non-linearities of the system. Also, the monotonous decrease of the vertical velocity is a result that was expected from a physical point of view. It is remarked that for this test both the gravitational acceleration and atmospheric density are kept constant and equal to their surface values, this for showing better the convergence to the equilibrium velocity, that otherwise would vary as a function of the altitude.

Other tests have also been conducted by giving as IC a positive flight path angle. These were also successful but are not shown to keep Figure 5.2 as clear as possible.

ENERGY DISSIPATION ANALYSIS

The main objective of a parachute system is to decelerate a payload descending through an atmosphere, or, in other words, to dissipate the energy that the spacecraft has accumulated during the previous flight phases. The major responsible for energy dissipation is the drag force that the parachute generates. In fact, as already shown in the previous validation step, the system always converges to the vertical flight condition, where $\theta \approx -90°$ and $\dot{\theta} \approx 0$. In this situation the rotational kinetic energy is 0. In this case the total energy of the system is given by:

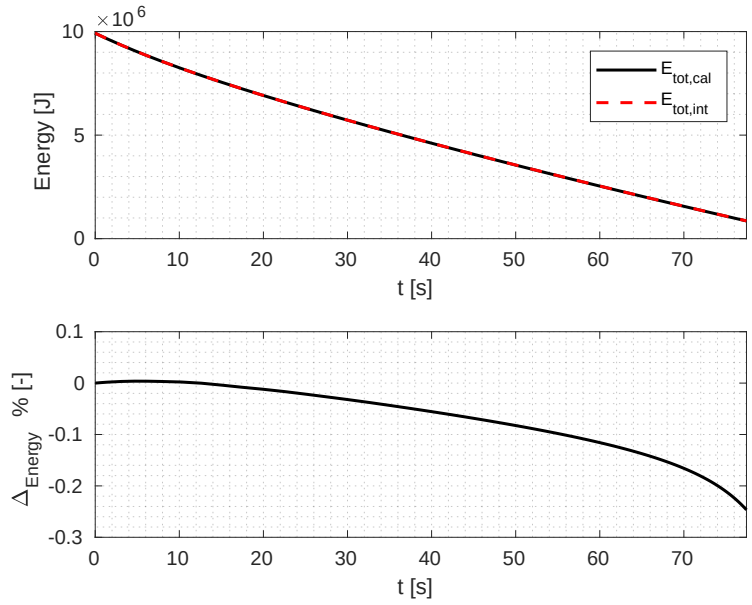

Figure 5.3: Total energy of the parachute-payload system along a vertical trajectory (IC: $\gamma_0 = -90°$, $\theta_0 = -90°$, $\dot{\theta}_0 = -90°$, $V_0 = 100\ \frac{\text{m}}{\text{s}}$, $z_0 = 6000$ m, $y_0 = 0$ m).

$$E_{\text{tot}} = \frac{m_g \dot{z}^2}{2} + m_g g z \tag{5.7}$$

By deriving E_{tot} with respect to time and inserting in it the EOM for $\ddot{z}$, simplified for the equilibrium condition, we get:

$$\dot{E}_{\text{tot}} = m_g \dot{z}\left(-g + \frac{D}{m}\right) + m_g g \dot{z} = D\dot{z} \tag{5.8}$$

Figure 5.3 shows that the total energy of the system during the descent flight reduces as a result of the drag dissipation. The correspondence of the total energy, calculated using Eq. (5.4) and Eq. (5.8) along the trajectory, shows that this validation test is successful.

OSCILLATORY BEHAVIOUR ANALYSIS

With this validation test we want to be demonstrate that the oscillatory motion of the parachute is influenced as expected by the aerodynamic forces and moment. For a certain Mach number, the aerodynamic coefficients, determining the sign of the corresponding forces and moment, are, according to the model in Section 3.2.3, an exclusive function of the angle of attack α of the parachute. In particular, C_D is positive per every α, C_L is positive for $\alpha > 0$ and negative for $\alpha < 0$ while C_m is negative for $\alpha > 0$ and positive for $\alpha < 0$.

We now consider a sample case for our parachute payload system, in which $\theta = -80°$ and $\gamma = -90°$ so that $\alpha = \theta - \gamma = 10°$. In this situation, according to the balance expressed by Eq. (3.41), the terms due to D, L and M should all generate a negative stabilizing contribution to $\ddot{\theta}$. If we assume that the initial $\dot{\theta} = 0$, it means that if all contributions from D, L and M are considered, then θ will reach its equilibrium value faster with respect to the case in which either L or M are neglected. In addition to this, as soon as θ goes past its equilibrium point, if D, L and M are all considered, then a moment triggering a rotation in the opposite direction will grow faster in magnitude and the overshoot of θ will be lower with respect to the case in which L or M are not considered. This situation is shown in Figure 5.4.

MPF PARACHUTE DESCENT DATA REPRODUCTION

This final test aims at determining if the 3DOF model can reproduce the real MPF trajectory with some accuracy. To do so the data derived from the EDL mission analysis in Spencer and Braun [1996] have been compared to the results obtained by simulating the same descent using the 3DOF MPF reference vehicle model.

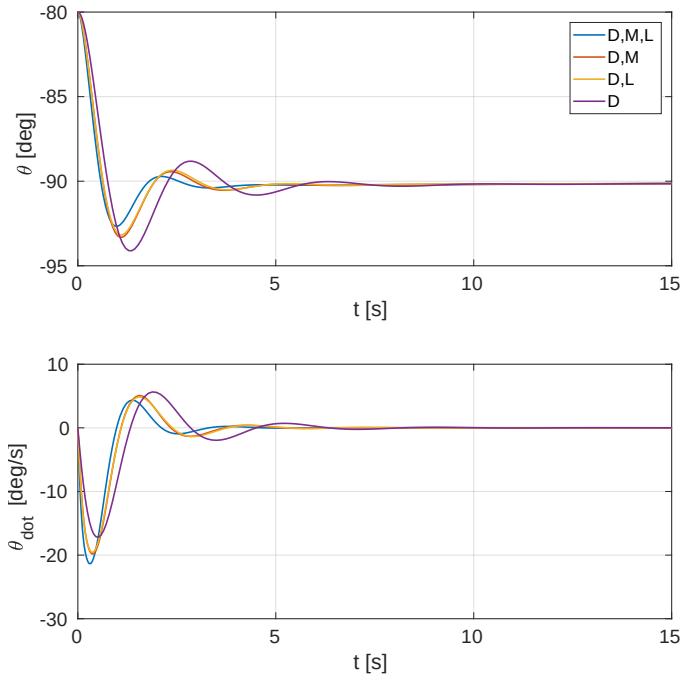

Figure 5.4: Oscillatory behaviour of the system with and without L force and/or aerodynamic moment (IC: $\gamma_0 = -90°$, $\theta_0 = -80°$, $V_0 = 100\ \frac{\text{m}}{\text{s}}$, $z_0 = 6000$ m, $y_0 = 0$ m).

Table 5.2: Descent trajectory comparison: simulation by Trovarelli *vs* data derived from Spencer and Braun [1996] (IC: $\gamma_0 = -25.83°$, $\theta_0 = -25.83°$, $\dot{\theta}_0 = 0°/\text{s}$, $V_0 = 386\ \frac{\text{m}}{\text{s}}$, $z_0 = 8600$ m, $y_0 = 0$ m).

	Spencer and Braun [1996]		Trovarelli		| Δ% |	
h [m]	**t** [s]	$\mathbf{V}_z$ [m/s]	**t** [s]	$\mathbf{V}_z$ [m/s]	| Δ**t**% |	| Δ$\mathbf{V}_z$% |
8600	0	-175.3	0	-175.3	0	0
6500	20.0	-71.7	22.4	-75.1	12.0	4.7
4700	45.0	-72.4	46.0	-77.2	2.2	6.6
1500	92.0	-65.0	89.0	-70.2	3.3	9.0
300	111.0	-62.0	106.6	-66.5	4.0	7.3
50	115.0	-60.0	110.4	-65.8	4.0	9.7

The first part of the simulated trajectory, between the altitudes of 8600 m and 4700 m, corresponds to the transient phase. In here, after the deployment the parachute stabilizes the payload until the vertical flight condition is reached. In this case the simulated trajectory shows a delay with respect to the reference data. This delay is due to the fact that the model does not consider the inflation of the parachute. In other words, in the real case the parachute does not generate immediately the maximum drag because it needs time to reach its nominal dimension.

After 4700 m the vertical velocity stabilizes around its equilibrium value. In this case the situation is opposite with respect to the transient phase because the simulated spacecraft decelerates less than in the real case and stabilizes on a larger vertical equilibrium velocity. This can be explained by considering that the dynamic model neglects the drag force generated by the elements other than the parachute. These would clearly contribute to further decelerating the vehicle. Also, it has to be noticed that the effect of neglecting the drag generated by the payload and backshell on the descent trajectory, is partially compensated by the fact that also the wake effect that these bodies cause is not taken into account. The latter is indeed responsible for a decrease in the aerodynamic force of the parachute.

In general, however, Table 5.2 shows that the error between the two trajectories is not larger than 10% for the vertical velocity and descent time. These data, together with the consideration above allow us to state that this test is successful.

5.2.3. MULTIBODY MODEL VERIFICATION

While the analysis of the physical double pendulum mechanics in Section 3.3.1 has served for proving the validity of the multibody apporach based on the concept of Neustadt et al. [1967], in this section it will be demonstrated that the resulting parachute-backshell-payload model, introduced in Section 3.3.2, behaves as expected. To do so we will first analyse how the energy of the system varies in different sample situations and then we will verify that the system converges to a predetermined equilibrium condition. These two tests, together with the double pendulum analysis, are assumed to be sufficient for verifying the multibody model introduced earlier since it can also be considered as an extension of the rigid body model validated in Section 5.2.2. It is remarked that the validation tests use the MPF nominal configuration whose details are discussed in Sections 3.2.3 and 3.3.2.

ENERGY DISSIPATION ANALYSIS

One of the aspects to analyse for understanding whether a model is consistent is its total energy. The total energy of the multibody parachute-backshell-payload system, derived using the Neustadt approach, shall consider, in addition to the contributions of the translational kinetic(k,t), rotational kinetic (k,r) and gravitational potential energies (p,g) of each element of the system, also the elastic potential energy (p,e) that is stored in the risers when these are lengthened, either positively or negatively. By assuming that the gravity on Mars is constant and equal to its surface value, the total energy E_{tot} of the whole spacecraft can be written as:

$$\begin{aligned} E_{\text{tot}} &= E_{k,t,1} + E_{k,t,2} + E_{k,t,3} + E_{k,r,1} + E_{k,r,2} + E_{k,r,3} \\ &\quad + E_{p,g,1} + E_{p,g,2} + E_{p,g,3} + E_{p,e,a} + E_{p,e,b} \\ &= \frac{1}{2}\left(m_1||\mathbf{V}_1||^2 + m_2||\mathbf{V}_2||^2 + m_3||\mathbf{V}_3||^2\right) \\ &\quad + \frac{1}{2}\left(I_1{\theta_1}^2 + I_2{\theta_1}^2 + I_3{\theta_1}^2\right) + g_0\left(m_1 z_1 + m_2 z_2 + m_3 z_3\right) \\ &\quad + \frac{1}{2}k_{r,a}\Delta l_a^2 + \frac{1}{2}k_{r,b}\Delta l_b^2 \end{aligned} \tag{5.9}$$

in which the subscripts 1,2 and 3 indicate, in this order, the parachute, backshell and payload elements. If we further assume that the spacecraft is flying in vacuum, then the energy should remain constant, because no dissipation mechanism acts on the system. This has been verified for several sets of sample IC and, for stringent propagator tolerances (`RelTol` = 10^{-8}, `AbsTol` = 10^{-10}) the relative error of the total energy with respect to its initial value was always in the order of 10^{-13}[1]. In these conditions the elastic energy is 0 because each of the multibody elements moves exclusively under the influence of the constant gravitational acceleration, so that in each point of the trajectory they are characterized by the same velocity and no riser elongation takes place. The situation is different if the gravity is assumed to vary with altitude. In this case the parachute, backshell and payload, whose COM are at different altitudes, do not feel the same exact gravitational acceleration. This in fact varies along the body in vertical direction. The resulting gradient, amongst others, causes that the velocities of the bodies per each instant are not exactly the same. This causes a small elongation of the risers, whose elastic force counteracts the gradient. This elongation, that causes the elastic potential energy to be different from 0 and to increase, grows until the external and internal forces balance.

The second test series related to energy analysis consisted, analogously to what already done for validating the rigid body model, of proving that the variation of the total energy of the system during a vertical flight in the atmosphere of Mars can either be obtained calculating Eq. (5.9) at each trajectory point, or by integrating Eq. (5.8), expressing the energy dissipation due to the drag, along the trajectory itself. In this case, for different sets of initial conditions, the relative error during the propagation was always lower than 1%. In addition to this it was verified that, along the vertical flight trajectory, the elastic potential energy is characterized by a first phase in which it oscillates. These oscillations, however, are damped and in the second phase this energy contribution tends to a stable condition. This expected behaviour is due to the fact that, as for the vacuum case, the forces acting on the vehicle, after a transient period, reach an equilibrium with the internal elastic forces generated by the risers lengthening.

[1] This relative error increases in case the tolerances of the integrator are larger. This is a characteristic of the multibody approach of Neustadt that, as explained earlier, is less accurate with respect to other multibody formulations due to the presence of the pseudo-spring approximation.

Table 5.3: IC for the multibody simulation of Figure 5.5.

Parameter	Value	Parameter	Value	Parameter	Value
γ_{10} [deg]	-85	γ_{20} [deg]	-95	γ_{30} [deg]	-90
θ_{10} [deg]	-80	θ_{20} [deg]	-100	θ_{30} [deg]	-90
$\dot{\theta}_{10}$ [deg/s]	1	$\dot{\theta}_{20}$ [deg/s]	-1	$\dot{\theta}_{30}$ [deg/s]	0
V_{10} [m/s]	100	V_{20} [m/s]	100	V_{30} [m/s]	100
z_{10} [m]	6000	$\theta_{r,1}$ [deg]	-90	$\theta_{r,2}$ [deg]	-90
y_{10} [m]	0	y_{20} [m]	0	y_{30} [m]	0

EQUILIBRIUM CONVERGENCE

The second test campaign for proving the validity of the multibody model based on the Neustadt approach consists of evaluating whether the system, irrespective of the IC, always converges to the steady-state flight condition and whether this condition is the one expected from a physical point of view. In particular, we expect that in absence of winds the drag generated by the parachute and the gravitational forces due to the masses of the system elements cause the vehicle to end up flying vertically, both with respect to the attitude of the spacecraft itself and the direction of the velocity vectors. This is clearly shown in Figure 5.5 from which we get that the attitude oscillations are damped and that the vertical velocity of the vehicle tends to its equilibrium condition, expressed by Eq. (5.6), that in this case is computed using varying atmospheric density and gravity. Also, the plots at the bottom demonstrate that the vertical distances between the COM of the multibody elements stabilize on the sum of the position of the hinges and the riser lengths (corresponding to the initial value for Δ_z), plus a small offset of some mm that is due to the equilibrium elongation of the risers. This is the condition in which the external forces acting on the system balance with the internal elastic contributions.

The plot for the vertical velocity of the system shows that the vertical velocity of the system remains always a little bit larger in magnitude than the equilibrium velocity. This delay is due to the fact that the equilibrium velocity decreases with altitude and, as a result, the system is always in deceleration. In fact, since the system has a certain inertia, the deceleration takes time and by the moment the system has decelerated to reach a certain equilibrium velocity, this has already became smaller and the system has to decelerate further. The offset between the equilibrium velocity and the vertical velocity of the system, that is in the order of 1 m/s, will never go to 0 but is smaller if the drag force of the parachute is more dominant with respect to the mass of the system.

Even if Figure 5.5 shows only one test case for clarity reasons, the same test has been run with other sample IC and the results were always satisfactory. It is finally remarked that the missing z coordinates for bodies 2 and 3 in the IC of Table 5.3 for Figure 5.5 are substituted in this case by the initial orientation of the risers. This is just an alternative way for determining the system IC.

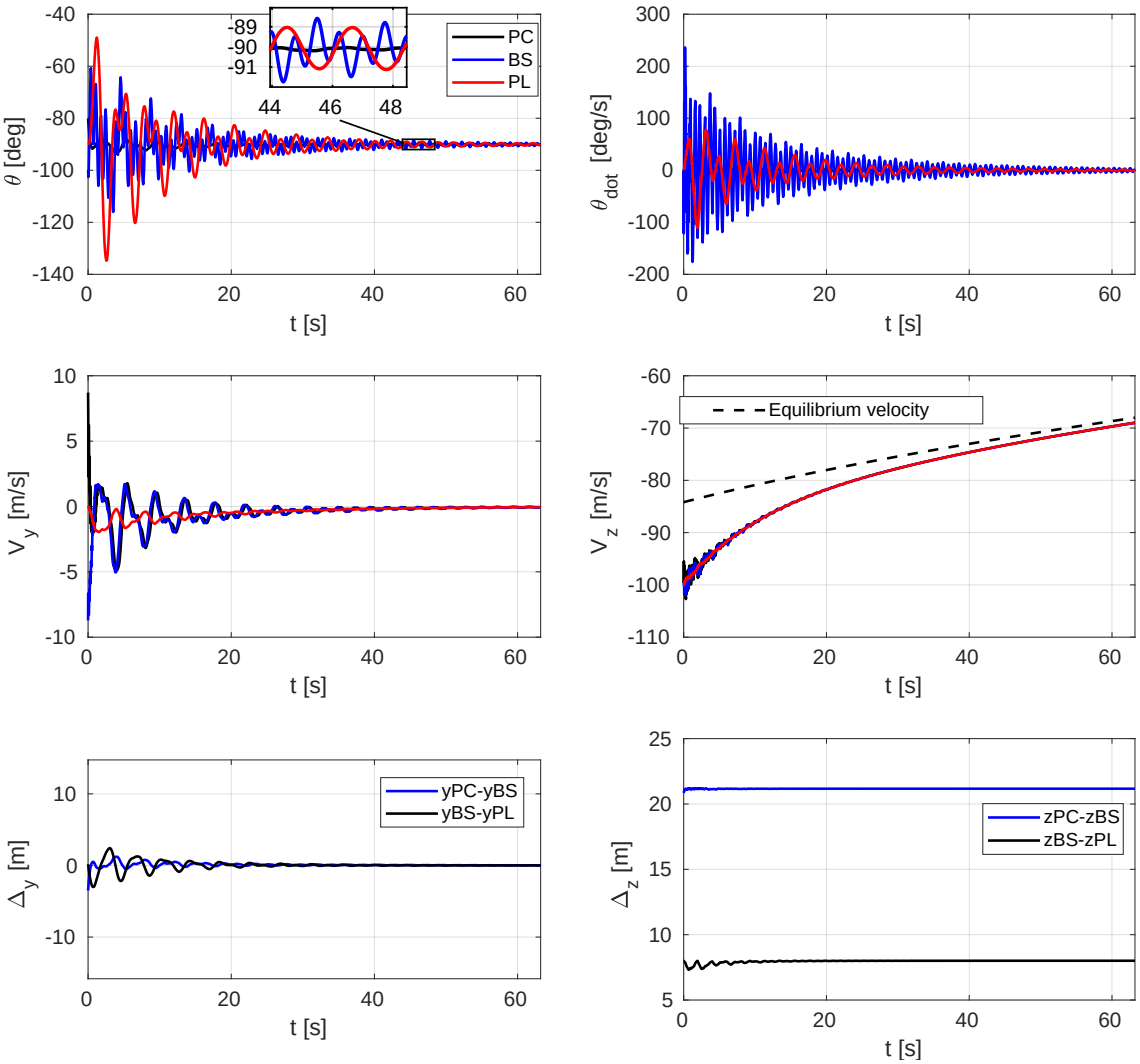

Figure 5.5: Sample MPF descent trajectory simulated with the multibody model based on Neustadt (IC from Table 5.3).

6

RIGID BODY OPEN-LOOP STABILITY

The study of the parachute-backshell-payload spacecraft dynamics starts with the analysis of the behaviour of the rigid-body model. Section 6.1 introduces the theory at the basis of dynamic stability studies. This theory is then applied in Section 6.2 where the nonlinear system developed in Section 3.2 is first linearised for the flight in steady-state condition and then some analytical information about its dynamics is derived.

6.1. DYNAMIC STABILITY

In Section 6.1.1, first the basic concepts about dynamic stability will be introduced. After this the Direct Method of Lyapunov, that represents the base for nonlinear stability analysis will be discussed. This method, as explained in Section 6.1.2, is easily applicable in case of linear systems but has limited practical utility with when one is dealing with nonlinear systems. In this case the Indirect Method of Lyapunov, introduced in Section 6.1.3, represents the most straightforward choice.

6.1.1. EQUILIBRIUM POINTS & DIRECT METHOD OF LYAPUNOV

A generic dynamical system is a system that satisfies the following conditions:

$$\dot{\mathbf{x}} = \mathbf{f}(\mathbf{x}, t) \qquad \mathbf{x}(t_0) = \mathbf{x}_0 \qquad \mathbf{x} \in \mathbb{R}^n \tag{6.1}$$

where $\mathbf{x}$ is a vector of generalized coordinates and $\mathbf{x}_0$ are the initial conditions the solution of the system $\mathbf{x}(t)$ has to satisfy. In addition to this, it is also requested that the function $\mathbf{f}(\mathbf{x}, t)$ guarantees that the solution $\mathbf{x}(t)$ exists and is unique.

The equilibrium point of a dynamical system is a particular state vector $\mathbf{x}^* \in \mathbb{R}^n$ for which it holds that $\mathbf{f}(\mathbf{x}^*, t) = 0$. This equilibrium point is *locally stable* if every solution $\mathbf{x}(t)$ satisfying the initial conditions $\mathbf{x}(t_0) = \mathbf{x}_0$ in the vicinity of the equilibrium point $\mathbf{x}^*$ remains close to it for every $t \geq t_0$. In the following, for practical reasons, the equilibrium point(s) will always be placed in the origin of the reference frame, so that $\mathbf{x}^* = 0$. Mathematically, an equilibrium point $\mathbf{x}^* = 0$ for $t = t_0$ is *stable in the sense of Lyapunov* if $\forall\, \epsilon > 0\ \exists\, \delta(t_0, \epsilon)$ such that:

$$\|\mathbf{x}(t_0)\| < \delta \quad \Rightarrow \quad \|\mathbf{x}(t)\| < \epsilon \quad \forall\, t > t_0 \tag{6.2}$$

The same point is also *asymptotically stable* if the solution $\mathbf{x}(t)$ gets closer to $\mathbf{x}^*$ for $t \to \infty$. In particular, an equilibrium point $\mathbf{x}^* = 0$ is *asymptotically stable* for $t = t_0$ if:

1. $\mathbf{x}^* = 0$ is stable in the sense of Lyapunov
2. $\mathbf{x}^* = 0$ is *locally attractive*, meaning that $\exists\, \delta(t_0)$ such that:

$$\|\mathbf{x}(t_0)\| < \delta \quad \Rightarrow \quad \lim_{t \to \infty} \mathbf{x}(t) = 0 \tag{6.3}$$

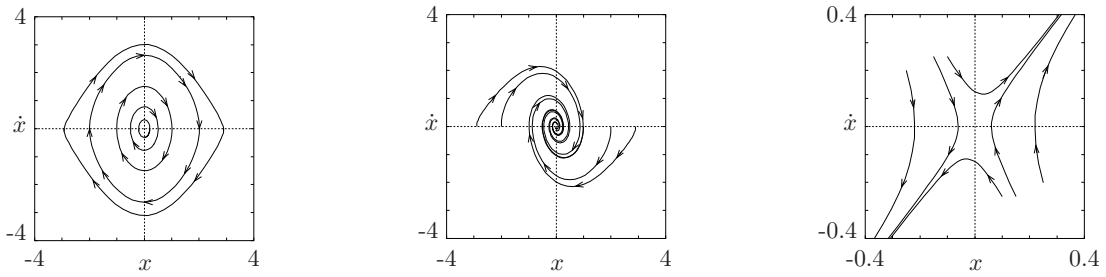

Figure 6.1: Type of equilibrium points according to Lyapunov definitions (from left to right: stable, asymptotically stable, unstable) [Murray et al., 1994].

The stability in the sense of Lyapunov is also *uniform* if the equilibrium point maintains its characteristics $\forall\, t > t_0$. This is the case if the function δ is not dependent on time t.

If the conditions expressed in Eq. (6.2) are not satisfied then the equilibrium point is said to be *unstable*. Also, Eq. (6.2) and (6.3) give conditions that have to be satisfied for assessing local stability. If the solutions $\mathbf{x}(t)$ still converges to $\mathbf{x}^*$ for initial conditions $\mathbf{x}_0$ not in the close vicinity of the equilibrium point, then the stability of $\mathbf{x}^*$ is said to be global. This latter case is a desirable property but is often difficult or impossible to obtain in practical situations. In the following we will exclusively consider systems in which the $\dot{\mathbf{x}}$ is not a direct function of the time t. These are called *time-invariant systems*.

Lyapunov introduced the basic concepts of dynamic stability. In addition, he developed the *Direct Method of Lyapunov* for evaluating the stability behaviour of a generic dynamical system. For each dynamical system, in fact, there exists an associated Lyapunov function, V, measuring a quantity that can be considered as a sort of energy related to it. According to this method, the dynamic stability characteristics of the system can be deduced, in agreement with the *Theorem of Lyapunov*, from an analysis of the properties of the Lyapunov function, whose value depends on the state of the dynamical system itself. In particular, if the equilibrium point of a system is stable, then the existence of a Lyapunov function V that satisfies the conditions the Theorem of Lyapunov for a stable equilibrium point is guaranteed. More detailed information about the Direct Method of Lyapunov and Lyapunov stability in general, as well as the formulation of the Theorem of Lyapunov can be found in Khalil [2001].

6.1.2. STABILITY OF LINEAR SYSTEMS

Consider the linear time-invariant system

$$\dot{\mathbf{x}} = \mathbf{A}\mathbf{x} \tag{6.4}$$

The Lyapunov function V of this system can simply be defined as:

$$V = \mathbf{x}^T \mathbf{P}\mathbf{x} \tag{6.5}$$

where $\mathbf{P}$, according to Khalil [2001] is the nonsingular matrix that block diagonalizes the state matrix $\mathbf{A}$. In this case the application of the Direct method of Lyapunov for the determination of the stability properties of the system reduces to the analysis of the eigenvalues and eigenvectors of $\mathbf{A}$.

Consider for example a $[2\times 2]$ state matrix $\mathbf{A}$. The corresponding state vector $\mathbf{x}$ will also be two-dimensional. Depending on the value of the eigenvalues λ_1 and λ_2 of $\mathbf{A}$, the following cases are possible:

- $\lambda_1 < \lambda_2 < 0$: the origin is a stable node
- $\lambda_1 > \lambda_2 > 0$: the origin is an unstable node
- $\lambda_1 < 0 < \lambda_2$: the origin is a saddle point
- $\lambda_{1,2} = \alpha + i\omega$: the origin is a centrum

In case of complex eigenvalues the system does not only tends towards (or diverges from) the equilibrium point but also oscillates around it. This type of equilibrium point is called centrum. In particular, as shown by

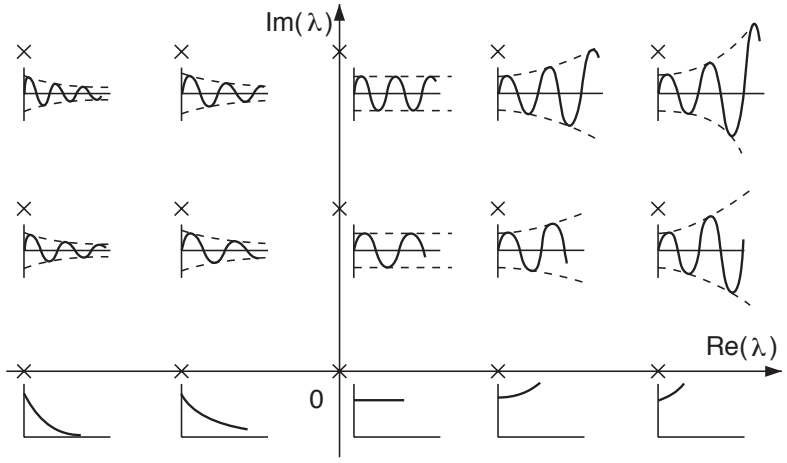

Figure 6.2: Stability and oscillation periodicity as a function of eigenvalues real and imaginary parts [D'Souza, 1988].

Figure 6.2, the real part of the eigenvalue has a major influence on the damping properties of the system. In particular, if the real part is more negative then the system, once perturbed, will tend back faster to its equilibrium position. The oscillations around the equilibrium are instead more significantly influenced by the imaginary part of the eigenvalue. If this is larger in magnitude then the oscillation frequency of the system about the equilibrium position will be higher. According to Golnaraghi and Kuo [1987], the damped oscillatory behaviour of a system around a stable centrum, defined by its natural frequency ω_n, damping ratio ζ and period P, can be dimensioned using the eigenvalues of its state matrix:

$$\omega_n = \sqrt{\mathrm{Re}(\lambda)^2 + \mathrm{Im}(\lambda)^2}, \qquad \zeta = -\frac{\mathrm{Re}(\lambda)}{\omega_n}, \qquad P = \frac{2\pi}{\mathrm{Im}(\lambda)} \tag{6.6}$$

The question is now to determine which eigenvalue of the state matrix has to be used in Eq (6.6). There are situations in which a certain eigenvalue is related to the dynamics of a single state variable. However, this is not normally true. In reality, in fact, the eigenvalues refer to a certain eigenmotion. The term eigenmotion indicates the modality through which a certain group of interrelated state variables dynamically evolve. If, for example, the state matrix describes the motion of a spaceplane along a steady-state trajectory, one eigenmotion could be represented by the attitude oscillations around the spacecraft COM. In such a case the state variables angular position θ and velocity $\dot{\theta}$ around a chosen axis would evolve together according to a certain characteristic scheme, called eigenmotion. The same dynamical system can, of course, have different types of eigenmotions and they do not necessarily need be characterized by an oscillatory behaviour. To understand how a certain eigenvalue is related to the eigenmotion variables and determine to what extent these influence the chosen eigenvalue, it is possible to analyse the eigenvectors of the state matrix. The rows of an eigenvector, that correspond to a precise eigenvalue, are related to the state variables. In principle the influence of the state variable n on the eigenvalue k is proportional to the value of the element of row n of the eigenvector k.

The state matrix associated to a linear system can be characterized by a certain number of blocks of variable dimension. Each block represents a certain eigenmotion of the system itself. If one identifies all the blocks in a certain state matrix, for example by analysing its eigenvectors, then it is possible to determine, through the study of the eigenvalues using the information above, the dynamic stability properties of each eigenmotion separately, this representing a great advantage in some cases because it greatly simplifies the calculations.

6.1.3. INDIRECT METHOD OF LYAPUNOV

The Direct Method of Lyapunov introduced in Section 6.1.3 has the advantage of being very general, because no assumption on the type of dynamical system analysed is made. In particular, deriving the Lyapunov function V for a linear system and analysing its properties, as explained in Section 6.1.2, is straightforward. Nevertheless, there is not a general methodology to derive the Lyapunov function for a nonlinear dynamic system, this making the Direct Method of Lyapunov scarcely applicable for many practical problems.

An alternative way to asses the stability that is more suitable for engineering applications is *Indirect Method of Lyapunov*. Consider the nonlinear dynamical system given by:

$$\dot{\mathbf{x}} = \mathbf{f}(\mathbf{x}) \tag{6.7}$$

in which $\mathbf{x}^T = (x_1, ..., x_n)$ is the state vector and $\mathbf{f}^T = \left(f_1, ..., f_n\right)$. The Indirect Method of Lyapunov, explained in detail by Khalil [2001], yields the conditions under which the stability characteristics of the nonlinear system in the vicinity of the linearisation point $\mathbf{x}_0$ are equivalent to those of the linear system:

$$\dot{\bar{\mathbf{x}}} = \mathbf{A}\bar{\mathbf{x}} \tag{6.8}$$

where $\bar{\mathbf{x}}$ is the deviation of the state $\mathbf{x}$ with respect to the linearisation point and $\mathbf{A}$ is the Jacobian matrix defined as:

$$\mathbf{A} = \left.\frac{\partial \mathbf{f}(\mathbf{x})}{\partial \mathbf{x}}\right|_{\mathbf{x}=\mathbf{x}_0} = \begin{bmatrix} \frac{\partial f_1(\mathbf{x})}{\partial x_1} & \cdots & \frac{\partial f_1(\mathbf{x})}{\partial x_n} \\ \vdots & \ddots & \vdots \\ \frac{\partial f_n(\mathbf{x})}{\partial x_1} & \cdots & \frac{\partial f_n(\mathbf{x})}{\partial x_n} \end{bmatrix}_{\mathbf{x}=\mathbf{x}_0} \tag{6.9}$$

This approach is used in any field of engineering. One example is Mooij [1998b], who linearises the EOM describing the motion of a spaceplane and then analyses the eigenmotion of the system by studying the eigenvalues of the resulting Jacobian matrix.

6.2. STABILITY ANALYSIS

The dynamic behaviour of a nonlinear system can be analysed in many ways. The approach that yields the most accurate results consists of investigating the properties of the Lyapunov function associated to the system. Its drawback, as already discussed in Section 6.1.1, is that a systematic procedure for determining the Lyapunov function of a generic nonlinear system does not exist. As a result, if a complex and highly nonlinear system has to be studied, the most straightforward procedure consists of analysing the linear system associated to it that, in the vicinity of the linearisation point, features the same behaviour of its nonlinear counterpart. In the following Sections, first the 3DOF parachute-payload nonlinear system developed in Section 3.2 will be linearised and then its stability properties will be investigated by means of the linear stability analysis techniques discussed in Section 6.1.2. It is remarked that it has been chosen to linearise the 3DOF rigid body model because it represents a good compromise between fidelity with respect to the real system and simplicity, the latter being a fundamental requirement if analytical results have to be derived.

6.2.1. SYSTEM LINEARISATION

The 3DOF nonlinear system describing the parachute-payload system descending in the atmosphere of Mars, introduced in Section 3.2, can be written as:

$$\dot{\mathbf{x}} = \mathbf{f}(\mathbf{x}) = \begin{pmatrix} f_1(x_4) \\ f_2(x_5) \\ f_3(x_6) \\ f_4(x_2, x_3, x_4, x_5, x_6) \\ f_5(x_2, x_3, x_4, x_5, x_6) \\ f_6(x_2, x_3, x_4, x_5, x_6) \end{pmatrix}, \quad \mathbf{x} = \begin{pmatrix} y \\ z \\ \theta \\ \dot{y} \\ \dot{z} \\ \dot{\theta} \end{pmatrix} = \begin{pmatrix} x_1 \\ x_2 \\ x_3 \\ x_4 \\ x_5 \\ x_6 \end{pmatrix} \tag{6.10}$$

From this description it is possible to derive the linear system:

$$\dot{\bar{\mathbf{x}}} = \mathbf{A}\bar{\mathbf{x}} \tag{6.11}$$

where $\bar{\mathbf{x}}$ indicates the deviation of the state with respect to its reference and $\mathbf{A}$ is the $[6 \times 6]$ Jacobian matrix associated to the system of Eq. (6.10). $\mathbf{A}$ can be found as:

$$\mathbf{A} = \begin{bmatrix} \frac{\partial f_1}{\partial x_1} & \cdots & \frac{\partial f_1}{\partial x_6} \\ \vdots & \ddots & \vdots \\ \frac{\partial f_6}{\partial x_1} & \cdots & \frac{\partial f_6}{\partial x_6} \end{bmatrix}_{\mathbf{x}=\mathbf{x}_{ss}} \tag{6.12}$$

To determine **A** we simply need to explicitly express the nonlinear system **f**(**x**) as a function of the elements of the state vector **x** and derive. However, the fact that the Jacobian has to be defined for a specific linearisation point along the trajectory, $\mathbf{x}_{ss}$, allows us to introduce in the EOM some assumptions. These, that are valid exclusively for the steady-state flight condition of the vehicle, contribute to significantly simplifying the derivation[1] of **A** for the reference MPF configuration. The following part of this section will be dedicated to this.

During a typical Mars EDL mission such as MPF, the parachute is deployed at and altitude between 10000 m and 8000 m, when the vehicle is flying with a low flight path angle, that can vary between $-10°$ and $-25°$ depending on the mission, and a Mach number between 1.5 and 2. When this happens the spacecraft experiences a deceleration peak that is followed by a transient phase in which the attitude of the system oscillates at a very high frequency and the flight path angle decreases. At an altitude of about 6000-5000 m the transient phase is concluded. At this point the vehicle is flying in steady-state conditions. During this flight phase the undisturbed spacecraft would descend vertically through the atmosphere of Mars. According to the convention in Figure 3.5, the angle of attack is $\approx 0°$ while both the attitude and flight path angles are $\approx -90°$. The vehicle has no horizontal velocity and the vertical velocity tends to the parachute-payload system equilibrium velocity, given by Eq. (5.6). For the MPF reference vehicle a representative steady-state vector would be:

$$\mathbf{x}_{ss} = \begin{pmatrix} x_1 \approx 0 \text{ [m]} \\ x_2 \approx 1000 \text{ [m]} \\ x_3 \approx 90° \\ x_4 \approx 0 \\ x_5 \approx 70 \left[\frac{\text{m}}{\text{s}}\right] \\ x_6 \approx 0 \end{pmatrix}, \quad \alpha \approx 0, \quad \gamma \approx 90° \tag{6.13}$$

While the choice of the steady-state value for the variables x_3, x_4 and x_6 is clear from the discussion above, the choices of x_1, x_2 and x_5 have to be explained. In particular, x_1, corresponding to the y-position, has absolutely no effect on the evolution of the system because it does not appear in any right hand side of the EOM, so that it can be assumed to have any value. Setting it to 0 is the most obvious choice. The altitude x_2, instead, determines the atmosphere density and the gravitational acceleration. Even tough these two variables, as will be pointed out later, vary very slowly, they still influence the dynamics of the spacecraft, so that the choice of x_2 has to be reasoned. In particular, we could have chosen any value within the steady-state range 6000-1000 m. The choice has fallen on 1000 m because in this way we can directly get information about the stability at a low altitude where, since the vertical velocity is lower, the system is more sensitive to external perturbation (this is also proven in Section 8.1.1). In addition to this, if a disturbance is experienced at a larger altitude, the system has more time to return to its stable position with respect to the case that the same disturbance happens in the vicinity of the target. In other words, we are more interested in studying the stability properties of the system where these properties have a critical influence on the success of the mission, this corresponding for our specific case to the descent phase just before the beginning of the terminal powered descent at an altitude of 1000 m. Finally, x_3=70 m/s is simply the approximated equilibrium velocity for the MPF vehicle at the altitude of 1000 m.

We start the simplification process by considering the velocity of the parachute with respect to the atmosphere. In case of no wind, according to Section 3.2.3, it is defined as:

$$\mathbf{V}_a = \begin{pmatrix} x_4 + x_6 \sin(x_3) z_{pc} \\ x_5 - x_6 \cos(x_3) z_{pc} \end{pmatrix} \tag{6.14}$$

If the vehicle is flying in steady-state conditions then $x_6 \cos(x_3) z_{pc} \approx 0$ is much smaller than x_5 and can be neglected. Also, $\sin(x_3) \approx -1$ so that $\mathbf{V}_a$ can be rewritten as:

$$\mathbf{V}_a \approx \begin{pmatrix} x_4 - x_6 z_{pc} \\ x_5 \end{pmatrix} \tag{6.15}$$

The norm of the airspeed determines the dynamic pressure on the parachute and, in turn, the aerodynamic forces. It is defined as:

$$V_a = ||\mathbf{V}_a|| = \sqrt{(x_4 - x_6 z_{pc})^2 + x_5^2} \tag{6.16}$$

[1] The most complicated steps of the analytical study reported here and in Chapter 7 have been validated using the software package `Maple` for symbolic calculus.

V_a can be simplified by considering that $x_4 \approx x_6 z_{\text{pc}} << x_5$, so that:

$$V_a \approx \sqrt{x_5^2} \tag{6.17}$$

The EOM of the first three state vector elements, i.e. the $y-$ and $z-$ position components x_1 and x_2 and the attitude angle θ, corresponding to x_3, are respectively:

$$\begin{aligned} \dot{x}_1 &= x_4 \\ \dot{x}_2 &= x_5 \\ \dot{x}_3 &= x_6 \end{aligned} \tag{6.18}$$

While these are very simple, the equations for the velocity in the *YZ*-plane and the attitude angle rotation velocity can be further simplified if the system is in its steady-state condition. To do so we need to analyse them one by one and try to physically understand the importance of each appearing term. For the velocity V_y (=x_4) we have:

$$\dot{x}_4 = \frac{-L\sin\gamma - D\cos\gamma}{m_g + m_a} \tag{6.19}$$

where m_g is the gravitational mass of the parachute-payload system while m_a is the added mass that depends on the atmosphere density ρ and, in turn, on the altitude x_2. In the steady-state flight region, corresponding to altitudes varying between 6000 m and 1000 m, however, ρ varies very slowly between 0.01 $\frac{\text{kg}}{\text{m}^3}$ and 0.015 $\frac{\text{kg}}{\text{m}^3}$. As a result, the variation of ρ, that also appears in the dynamic pressure term determining the aerodynamic forces, would not significantly affect the stability behaviour of the model and can be neglected by considering it constant in defining the linear model. If the atmospheric density is considered constant, then also the added mass is constant and equal to its value calculated in the steady-state condition. The inertial mass of the vehicle can thus be written as $m = m_g + m_a$.

In steady-state conditions, the angle of attack is $\alpha \approx 0$. This allows for a simplification of the definition of the aerodynamic coefficients. By looking at Figure 3.6 we notice that a possible simplification would be to assume that C_D is a positive constant and that both C_L and C_m can be described by a line. So we have:

$$\begin{aligned} C_D &= C_D(0) = C_{D,0} & C_{D,0} &= 0.3449 \\ C_L &= k_{C_L}\alpha & k_{C_L} &= 0.4414 \\ C_m &= k_{C_m}\alpha & k_{C_m} &= -0.7212 \end{aligned} \tag{6.20}$$

where k_{C_L} and k_{C_m} have been obtained by fitting a line on the the experimental data from Cruz et al. [2003]. This approximation has been validated by checking that the response of the nonlinear system does not change significantly when using the approximated coefficients. By substituting the coefficients of Eq. (6.20) in Eq. (6.19) we get:

$$\dot{x}_4 = -\frac{q_{\text{dyn}} S_{\text{ref}}(k_{C_L}\alpha\sin\gamma + C_{D,0}\cos\gamma)}{m} \tag{6.21}$$

If, once more, we consider that the vehicle is flying in steady-state conditions, then $k_{C_L}\alpha \approx 0$, $\sin\gamma \approx -1$ and $\cos\gamma$, that for $\gamma \to -\frac{\pi}{2}$ can be approximated as $\gamma + \frac{\pi}{2}$, tends to 0 as well. This allows us to further simplify Eq. (6.19) but also tells us that both terms at the numerator have comparable magnitude and none of them can be ignored. By introducing in Eq. (6.19) the assumptions discussed until now we get:

$$\begin{aligned} \dot{x}_4 &\approx -\frac{q_{\text{dyn}} S_{\text{ref}}\left(-k_{C_L}\alpha + C_{D,0}\left(\gamma + \frac{\pi}{2}\right)\right)}{m} \\ &= -\frac{S_{\text{ref}}\rho x_5^2\left(-k_{C_L}\left(x_3 - \arctan\left(x_5, x_4 - x_6 z_{\text{pc}}\right)\right) + C_{D,0}\left(\arctan\left(x_5, x_4 - x_6 z_{\text{pc}}\right) + \frac{\pi}{2}\right)\right)}{2m} \end{aligned} \tag{6.22}$$

The same procedure is applied to also simplify $\dot{x}_5$ and $\dot{x}_6$. For $\dot{x}_5$ we have:

$$\dot{x}_5 = \frac{m_g g - q_{\text{dyn}} S_{\text{ref}}(-k_{C_L}\alpha\cos\gamma + C_{D,0}\sin\gamma)}{m} \tag{6.23}$$

In this case we have that $k_{C_L}\alpha \approx \cos\gamma \approx 0$ while instead $\sin\gamma \approx -1$. As a result it holds that $k_{C_L}\alpha\cos\gamma << C_{D,0}\sin\gamma$ so that, in this case, the contribution of the L force can be neglected with respect to the drag force contribution. However, it is also interesting to understand how does the aerodynamic term, reduced to the only drag, compares to the gravity term in the vertical equilibrium equation. To do so we need to calculate approximated values for both terms in the steady-state condition. By inserting the spacecraft properties of MPF presented in Section 3.2.3, we get that, for a descent in steady-state conditions starting at an altitude of ≈ 6000 m with a velocity of ≈ 120 m/s, the drag force ranges between 3000 N and 1000 N while the gravity force is almost constant around 1300 N. This makes it clear that the gravitational and aerodynamic contributions to the vertical force equilibrium are comparable and none of them can be ignored. However, what can still be done to simplify this equation is to also consider the gravitational acceleration as a constant. This is justified by the fact that, similarly to what happens for the the atmosphere density, the variation of g as a function of x_2 is very small in the steady-state region and it does not significantly affect stability characteristics of the model. The resulting $\dot{x}_5$ can thus be written as:

$$\dot{x}_5 \approx \frac{2m_g g + \rho x_5^2 S_{\text{ref}} C_{D,0}}{2m} \tag{6.24}$$

Finally, we need to analyse the rotational equilibrium equation $\dot{x}_6$, that is:

$$\dot{x}_6 = -\frac{q_{\text{dyn}} S_{\text{ref}} \left(z_{\text{pc}} \left(k_{C_L}\alpha\cos\alpha + C_{D,0}\sin\alpha\right) - k_{C_m}\alpha D_0\right)}{I_{X_B} + I_{a,X_B}} \tag{6.25}$$

Since we already assumed that ρ, and in turn the added mass m_a, are constant, then the additional moment of inertia it causes will be constant as well. Because of this we write $I_{\text{tot}} = I_{X_B} + I_{a,X_B}$. Also, it is assumed that the parachute COP is fixed with respect to the body frame B and corresponds to the parachute COM. By means of numerical simulations, also this simplification has been proven to be acceptable for the purpose of this study because it does not significantly influence the stability properties of the rigid body model. In steady-state conditions ($\alpha \approx 0$) it is possible to consider that $\cos\alpha \approx 1$ and $\sin\alpha \approx \alpha$. If one inserts this information into Eq. (6.25), this gives after rearrangement:

$$\dot{x}_6 \approx -\frac{q_{\text{dyn}} S_{\text{ref}} \alpha \left(z_{\text{pc}} k_{C_L} + z_{\text{pc}} C_{D,0} - k_{C_m} D_0\right)}{I_{\text{tot}}} \tag{6.26}$$

in which all the 3 terms expressing the aerodynamic contributions, i.e., $z_{\text{pc}} k_{C_L}$, $z_{\text{pc}} C_{D,0}$, and $k_{C_m} D_0$ have comparable magnitude. Because of this none of them can be neglected. The resulting simplified explicit equation for $\dot{x}_6$ is:

$$\dot{x}_6 \approx -\frac{\rho x_5^2 S_{\text{ref}} \left(x_3 - \arctan\left(x_5, x_4 - x_6 z_{\text{pc}}\right)\right)\left(z_{\text{pc}} k_{C_N} + z_{\text{pc}} C_{D,0} - k_{C_m} D_0\right)}{2 I_{\text{tot}}} \tag{6.27}$$

The dynamics of the parachute-payload spacecraft, in proximity of the the linearisation point $\mathbf{x}_{\text{ss}}$, in which it is flying is steady-state conditions, is thus accurately described by the system:

$$\dot{\mathbf{x}} = \mathbf{f}(\mathbf{x}) = \begin{pmatrix} x_4 \\ x_5 \\ x_6 \\ -\frac{S_{\text{ref}}\rho x_5^2\left(-k_{C_L}\left(x_3 - \arctan\left(x_5, x_4 - x_6 z_{\text{pc}}\right)\right) + C_{D,0}\left(\arctan\left(x_5, x_4 - x_6 z_{\text{pc}}\right) + \frac{\pi}{2}\right)\right)}{2m} \\ \frac{2m_g g + \rho x_5^2 S_{\text{ref}} C_{D,0}}{2m} \\ -\frac{\rho x_5^2 S_{\text{ref}}\left(x_3 - \arctan\left(x_5, x_4 - x_6 z_{\text{pc}}\right)\right)\left(z_{\text{pc}} k_{C_L} + z_{\text{pc}} C_{D,0} - k_{C_m} D_0\right)}{2 I_{\text{tot}}} \end{pmatrix} \tag{6.28}$$

The nonlinear system in Eq. (6.28), thanks to the simplifications, is characterized by a much lower degree of complexity with respect to the initial nonlinear model it is derived from and will thus be used for studying analytically the stability behaviour of the parachute-payload system in steady-state conditions. The elements of

matrix **A** of Eq. (6.12) defining the associated linear system can be found, according to Eq. (6.12), by differentiating the EOM with respect to the state vector components. These are:

$$
\begin{aligned}
&\frac{\partial f_1}{\partial x_1}=0,\quad \frac{\partial f_1}{\partial x_2}=0,\quad \frac{\partial f_1}{\partial x_3}=0,\quad \frac{\partial f_1}{\partial x_4}=1,\quad \frac{\partial f_1}{\partial x_5}=0,\quad \frac{\partial f_1}{\partial x_6}=0;\\
&\frac{\partial f_2}{\partial x_1}=0,\quad \frac{\partial f_2}{\partial x_2}=0,\quad \frac{\partial f_2}{\partial x_3}=0,\quad \frac{\partial f_2}{\partial x_4}=0,\quad \frac{\partial f_2}{\partial x_5}=1,\quad \frac{\partial f_2}{\partial x_6}=0;\\
&\frac{\partial f_3}{\partial x_1}=0,\quad \frac{\partial f_3}{\partial x_2}=0,\quad \frac{\partial f_3}{\partial x_3}=0,\quad \frac{\partial f_3}{\partial x_4}=0,\quad \frac{\partial f_3}{\partial x_5}=0,\quad \frac{\partial f_3}{\partial x_6}=1;\\
&\frac{\partial f_4}{\partial x_1}=0,\quad \frac{\partial f_4}{\partial x_2}=0,\quad \frac{\partial f_4}{\partial x_3}=\frac{S_{\text{ref}}\,\rho\,{x_5}^2\,k_{C_L}}{2m},\\
&\frac{\partial f_4}{\partial x_4}=\frac{S_{\text{ref}}\,\rho\,{x_5}^3\left(C_{D,0}+k_{C_L}\right)}{2m\left(-z_{\text{pc}}\,x_6+x_4\right)^2\left(1+\frac{{x_5}^2}{\left(-z_{\text{pc}}\,x_6+x_4\right)^2}\right)},\\
&\frac{\partial f_4}{\partial x_5}=-\frac{S_{\text{ref}}\,\rho\,x_5}{2m}\left(2\left(C_{D,0}\left(\arctan\left(x_5,-z_{\text{pc}}\,x_6+x_4\right)+\frac{\pi}{2}\right)\right)+\ldots\right.\\
&\qquad\left.\ldots-k_{C_L}\left(x_3-\arctan\left(x_5,-z_{\text{pc}}\,x_6+x_4\right)\right)\right)+\frac{x_5\left(C_{D,0}+k_{C_L}\right)}{\left(-z_{\text{pc}}\,x_6+x_4\right)\left(1+\frac{{x_5}^2}{\left(-z_{\text{pc}}\,x_6+x_4\right)^2}\right)}\Bigg),\\
&\frac{\partial f_4}{\partial x_6}=-\frac{S_{\text{ref}}\,\rho\,{x_5}^3\,z_{\text{pc}}\left(C_{D,0}+k_{C_L}\right)}{2m\left(-z_{\text{pc}}\,x_6+x_4\right)^2}\left(1+\frac{{x_5}^2}{\left(-z_{\text{pc}}\,x_6+x_4\right)^2}\right)^{-1};\\
&\frac{\partial f_5}{\partial x_1}=0,\quad \frac{\partial f_5}{\partial x_2}=0,\quad \frac{\partial f_5}{\partial x_3}=0,\quad \frac{\partial f_5}{\partial x_4}=0,\quad \frac{\partial f_5}{\partial x_5}=\frac{C_{D,0}\,S_{\text{ref}}\,\rho\,x_5}{m},\quad \frac{\partial f_5}{\partial x_6}=0;\\
&\frac{\partial f_6}{\partial x_1}=0,\quad \frac{\partial f_6}{\partial x_2}=0,\quad \frac{\partial f_6}{\partial x_3}=-\frac{S_{\text{ref}}\,\rho\,{x_5}^2\left(C_{D,0}\,z_{\text{pc}}-D_0\,k_{C_m}+z_{\text{pc}}\,k_{C_L}\right)}{2I_{\text{tot}}},\\
&\frac{\partial f_6}{\partial x_4}=-\frac{S_{\text{ref}}\,\rho\,{x_5}^3\left(C_{D,0}\,z_{\text{pc}}-k_{C_m}\,D_0+k_{C_L}\,z_{\text{pc}}\right)}{2\left(-x_6\,z_{\text{pc}}+x_4\right)^2\,I_{\text{tot}}}\left(1+\frac{{x_5}^2}{\left(-x_6\,z_{\text{pc}}+x_4\right)^2}\right)^{-1},\\
&\frac{\partial f_6}{\partial x_5}=-\frac{S_{\text{ref}}\,\rho\,x_5\left(C_{D,0}\,z_{\text{pc}}-D_0\,k_{C_m}+z_{\text{pc}}\,k_{C_L}\right)}{I_{\text{tot}}}\Bigg(\frac{x_5\left(1+\frac{{x_5}^2}{\left(-x_6\,z_{\text{pc}}+x_4\right)^2}\right)^{-1}}{2\left(-x_6\,z_{\text{pc}}+x_4\right)}+\ldots\\
&\qquad\ldots-\left(x_3-\arctan\left(x_5,-x_6\,z_{\text{pc}}+x_4\right)\right)\Bigg),\\
&\frac{\partial f_6}{\partial x_6}=\frac{S_{\text{ref}}\,\rho\,{x_5}^3\,z_{\text{pc}}\left(C_{D,0}\,z_{\text{pc}}-D_0\,k_{C_m}+z_{\text{pc}}\,k_{C_L}\right)}{2\left(-x_6\,z_{\text{pc}}+x_4\right)^2\,I_{\text{tot}}}\left(1+\frac{{x_5}^2}{\left(-x_6\,z_{\text{pc}}+x_4\right)^2}\right)^{-1};
\end{aligned}
\tag{6.29}
$$

Also in this case an accurate physical analysis can lead to an even more compact system. Since the spacecraft is assumed to be flying vertically without rotating, then $x_5 >> x_4 - x_6 z_{\text{pc}}$. This results in the fact that we can approximate the recurring term:

$$
1+\frac{x_5^2}{\left(x_4-x_6\,z_{\text{pc}}\right)^2}\approx\frac{x_5^2}{\left(x_4-x_6\,z_{\text{pc}}\right)^2}
\tag{6.30}
$$

After inserting Eq. (6.30) in (6.29) and rearranging (this step is left to the reader), we also consider that:

$$
\begin{aligned}
&\arctan\left(x_5,-z_{\text{pc}}\,x_6+x_4\right)\approx-\frac{\pi}{2}\\
&x_3-\arctan\left(x_5,-z_{\text{pc}}\,x_6+x_4\right)\approx 0\\
&\frac{-z_{\text{pc}}\,x_6+x_4}{x_5}\approx 0
\end{aligned}
\tag{6.31}
$$

so that the final form of the simplified Jacobian is:

$$
\begin{aligned}
&\frac{\partial f_1}{\partial x_1}=0, \quad \frac{\partial f_1}{\partial x_2}=0, \quad \frac{\partial f_1}{\partial x_3}=0, \quad \frac{\partial f_1}{\partial x_4}=1, \quad \frac{\partial f_1}{\partial x_5}=0, \quad \frac{\partial f_1}{\partial x_6}=0;\\
&\frac{\partial f_2}{\partial x_1}=0, \quad \frac{\partial f_2}{\partial x_2}=0, \quad \frac{\partial f_2}{\partial x_3}=0, \quad \frac{\partial f_2}{\partial x_4}=0, \quad \frac{\partial f_2}{\partial x_5}=1, \quad \frac{\partial f_2}{\partial x_6}=0;\\
&\frac{\partial f_3}{\partial x_1}=0, \quad \frac{\partial f_3}{\partial x_2}=0, \quad \frac{\partial f_3}{\partial x_3}=0, \quad \frac{\partial f_3}{\partial x_4}=0, \quad \frac{\partial f_3}{\partial x_5}=0, \quad \frac{\partial f_3}{\partial x_6}=1;\\
&\frac{\partial f_4}{\partial x_1}=0, \quad \frac{\partial f_4}{\partial x_2}=0, \quad \frac{\partial f_4}{\partial x_3}=\frac{S_{\text{ref}}\,\rho\,{x_5}^2\,k_{C_L}}{2m}, \quad \frac{\partial f_4}{\partial x_4}=\frac{S_{\text{ref}}\,\rho\,x_5\left(C_{D,0}+k_{C_L}\right)}{2m},\\
&\frac{\partial f_4}{\partial x_5}\approx 0, \quad \frac{\partial f_4}{\partial x_6}=-\frac{S_{\text{ref}}\,\rho\,x_5 z_{\text{pc}}\left(C_{D,0}+k_{C_L}\right)}{2m};\\
&\frac{\partial f_5}{\partial x_1}=0, \quad \frac{\partial f_5}{\partial x_2}=0, \quad \frac{\partial f_5}{\partial x_3}=0, \quad \frac{\partial f_5}{\partial x_4}=0, \quad \frac{\partial f_5}{\partial x_5}=\frac{C_{D,0}\,S_{\text{ref}}\,\rho\,x_5}{m}, \quad \frac{\partial f_5}{\partial x_6}=0;\\
&\frac{\partial f_6}{\partial x_1}=0, \quad \frac{\partial f_6}{\partial x_2}=0, \quad \frac{\partial f_6}{\partial x_3}=-\frac{S_{\text{ref}}\,\rho\,{x_5}^2\left(C_{D,0}\,z_{\text{pc}}-D_0\,k_{C_m}+z_{\text{pc}}\,k_{C_L}\right)}{2I_{\text{tot}}},\\
&\frac{\partial f_6}{\partial x_4}=-\frac{S_{\text{ref}}\,\rho\,x_5\left(C_{D,0}\,z_{\text{pc}}-k_{C_m}\,D_0+k_{C_L}\,z_{\text{pc}}\right)}{2I_{\text{tot}}},\\
&\frac{\partial f_6}{\partial x_5}\approx 0, \quad \frac{\partial f_6}{\partial x_6}=\frac{S_{\text{ref}}\,\rho\,x_5 z_{\text{pc}}\left(C_{D,0}\,z_{\text{pc}}-D_0\,k_{C_m}+z_{\text{pc}}\,k_{C_L}\right)}{2I_{\text{tot}}};
\end{aligned}
\tag{6.32}
$$

The linear model defined by Eq. (6.32) represents the most simple linear model that it is possible to obtain from the initial nonlinear 3DOF rigid body parachute-payload model that still ensures a very good level of accuracy. It will thus be used for the following analytical stability study. It is remarked that every step of the simplification process has been verified by comparing the linearised system initial condition, step and impulse responses after the simplification of the variables having a constant equilibrium position[2], i.e., V_y, V_z, θ and $\dot{\theta}$, with the corresponding responses of the nonlinear system. In every case the two systems showed an analogous dynamic behaviour so that the simplifications were considered to be valid.

6.2.2. EIGENMOTION ANALYSIS

At this point we are ready to derive analytical expressions for the eigenvalues of the Jacobian matrix **A**, whose elements are given by Eq. (6.32). These will determine the dynamic stability properties of the parachute-payload system. However, determining these analytical expressions by solving the characteristic equation associated to the full $[6\times 6]$ **A** is not possible. An alternative solution consists of identifying the block structure of the matrix and find the eigenvalues of these blocks, that will correspond to the eigenvalues of the complete matrix. The drawback of this approach is that to identify the blocks, while still being able to get simple expressions for the eigenvalues, some other assumptions have to be introduced in the system.

First of all, it is easy to note that the columns 1 and 2 of matrix **A** only contain zeros. As a result its rank will not be higher than 4 and two eigenvalues will be null. From the physics of the problem and the assumptions we made earlier it is clear that these null eigenvalues should refer to variables x_1 and x_2. These correspond to the horizontal and vertical position components and are not present at all in the right hand sides of the elements of the Jacobian **A**. This can be proved by analysing the relationship between its eigenvalues and eigenvectors. In particular, by determining the value of the elements of **A** for a specific linearisation point, it is possible, using the `Matlab` function `eig`[3], to compute numerically both the eigenvalues and eigenvectors of **A** for that point. It has been checked that, for every point chosen of the steady-state vertical trajectory of the MPF vehicle, the first and fifth eigenvalues, λ_1 and λ_5, were null. The corresponding first and fifth eigenvectors, instead, for every considered point were:

$$
\mathbf{v}_{\lambda_1,(1)}=\begin{pmatrix}1 & 0 & 0 & 0 & 0 & 0\end{pmatrix}^T, \quad \mathbf{v}_{\lambda_5,(1)}=\begin{pmatrix}0 & 1 & 0 & 0 & 0 & 0\end{pmatrix}^T \tag{6.33}
$$

[2] The nonlinear model simulates the response the state variables of the system. The linearised system instead can only reproduce the dynamic evolution of the deviation with respect to the reference point. In general thus, comparing them is not possible. Nevertheless, it is possible that some of the state variables feature a constant condition equilibrium. In this case it is possible to translate the linear system on the nonlinear one to check whether the characteristics of the dynamic response for these particular variables in the vicinity of the reference point is analogous for the two systems.

[3] https://nl.mathworks.com/help/matlab/ref/eig.html. Last accessed: 18/01/2018.

The fact that x_1 and x_2 are dominant, respectively, in eigenvectors $\mathbf{v}_{\lambda_1}$ and $\mathbf{v}_{\lambda_5}$, proves that the null eigenvalues correspond to the horizontal and vertical position components state variables. In addition to this, the analysis of the eigenvectors has revealed that their components 2 and 5 are always 0 except for $\mathbf{v}_{\lambda_1,(1)}$ and $\mathbf{v}_{\lambda_5,(1)}$. This means, as expected, that variables x_1 and x_2 have no role in the dynamic evolution of the linearised dynamic system. Considering these, we are allowed to eliminate, without loss of information, columns 1 and 2 and rows 1 and 2, and only study the resulting $[4\times4]$ matrix that is:

$$\mathbf{A}_{(1)} = \begin{bmatrix} 0 & 0 & 0 & 1 \\ \frac{\partial f_4}{\partial x_3} & \frac{\partial f_4}{\partial x_4} & 0 & \frac{\partial f_4}{\partial x_6} \\ 0 & 0 & \frac{\partial f_5}{\partial x_5} & 0 \\ \frac{\partial f_6}{\partial x_3} & \frac{\partial f_6}{\partial x_4} & 0 & \frac{\partial f_6}{\partial x_6} \end{bmatrix} \tag{6.34}$$

where the subscript (i), in the case of Eq. (6.34) corresponding to (1), will be used throughout the eigenvalues derivation for indicating the version of the Jacobian matrix $\mathbf{A}$ that is being considered in a particular step. By swapping in $\mathbf{A}_{(1)}$ column and row 4 with column and row 2 and, then, the new column and row 4 with column and row 3 one obtains:

$$\mathbf{A}_{(2)} = \begin{bmatrix} 0 & 1 & 0 & 0 \\ \frac{\partial f_6}{\partial x_3} & \frac{\partial f_6}{\partial x_6} & \frac{\partial f_6}{\partial x_4} & 0 \\ \frac{\partial f_4}{\partial x_3} & \frac{\partial f_4}{\partial x_6} & \frac{\partial f_4}{\partial x_4} & 0 \\ 0 & 0 & 0 & \frac{\partial f_5}{\partial x_5} \end{bmatrix} \tag{6.35}$$

that makes it clear that the vertical velocity eigenmotion, related to variable x_5, is completely decoupled with respect to the rotational and translational horizontal velocity ones. The fact that eigenvalue $\lambda_{4,(2)}$ of matrix $\mathbf{A}_{(2)}$ corresponds to x_5 can be proved by noting that eigenvector $\mathbf{v}_{\lambda_4,(2)}$, for every point of the steady-state trajectory, has all zeros except for its last element, that is 1. In fact, the operations of simultaneous column and row swap were performed in such a way that in a certain row appear all the derivatives of the same EOM with respect to the state vector elements. In this way the row is directly related to a particular state variable. In this case row 4 is related to variable x_5. As a result, the eigenvalue related to the vertical velocity is given by:

$$\lambda_{V_z} = \frac{\partial f_5}{\partial x_5} = \frac{C_{D,0}\, S_{\text{ref}}\, \rho\, x_5}{m} \tag{6.36}$$

We now want to find also the eigenvalues of the remaining $[3\times3]$ block, that we rewrite as:

$$\mathbf{A}_{(3)} = \begin{bmatrix} 0 & 1 & 0 \\ \frac{\partial f_6}{\partial x_3} & \frac{\partial f_6}{\partial x_6} & \frac{\partial f_6}{\partial x_4} \\ \frac{\partial f_4}{\partial x_3} & \frac{\partial f_4}{\partial x_6} & \frac{\partial f_4}{\partial x_4} \end{bmatrix} \tag{6.37}$$

However, determining them for a $[3\times3]$ matrix by means of the characteristic equation $\det(\mathbf{A}_{(3)} - \boldsymbol{\lambda}\mathbf{I}) = 0$, where $\boldsymbol{\lambda}$ is the vector containing the eigenvalues, or by rearranging the terms in such a way that different blocks can be analytically identified would still result in overcomplicated definitions. The most efficient option consists of introducing approximations in $\mathbf{A}_{(3)}$ so that to obtain smaller blocks that can more easily be solved. First, according to the definitions in Eq. (6.32), we notice that:

$$\text{norm}\begin{pmatrix} \frac{\partial f_4}{\partial x_4} \\ \frac{\partial f_4}{\partial x_6} \end{pmatrix} = \text{norm}\begin{pmatrix} \frac{\partial f_6}{\partial x_4} \\ \frac{\partial f_6}{\partial x_6} \end{pmatrix} = \frac{1}{z_{\text{pc}}} \tag{6.38}$$

Since $z_{\text{pc}} = 23.70$ m for the considered MPF configuration, then $\frac{1}{z_{\text{pc}}} << 1$. This means that the magnitude of terms $\frac{\partial f_4}{\partial x_4}$ and $\frac{\partial f_6}{\partial x_4}$ is much smaller than the magnitude of terms $\frac{\partial f_4}{\partial x_6}$ and $\frac{\partial f_6}{\partial x_6}$. In addition to this, calculating the terms $\frac{\partial f_6}{\partial x_3}$, $\frac{\partial f_6}{\partial x_6}$, $\frac{\partial f_4}{\partial x_3}$ and $\frac{\partial f_4}{\partial x_6}$ for the MPF reference vehicle flying in steady-state conditions shows that their magnitude is in the order of 1 to 10. According to these, all the terms in column 3 of matrix $\mathbf{A}_{(3)}$ can be approximated with 0 and the Jacobian can be reduced to:

$$\mathbf{A}_{(4)} = \begin{bmatrix} 0 & 1 \\ \frac{\partial f_6}{\partial x_3} & \frac{\partial f_6}{\partial x_6} \\ \frac{\partial f_4}{\partial x_3} & \frac{\partial f_4}{\partial x_6} \end{bmatrix} \tag{6.39}$$

Matrix $\mathbf{A}_{(4)}$ is clearly rank deficient. One of its lines is linearly dependent on the others. However, we want to keep the terms of the Jacobian expressing the derivatives of the attitude angle and velocity of the system with respect to themself. In other words we want to demonstrate that the third line of matrix $\mathbf{A}_{(4)}$ is linearly dependent on rows 1 and 2 of the same matrix. Without performing the actual calculations, it is enough to notice that a linear combination of rows 2 and 3 can lead term $A_{(4)}(3,1)$ to 0 and, then, the new term $A_{(4)}(3,2)$, that will be a linear combination of $\frac{\partial f_6}{\partial x_6}$ and $\frac{\partial f_4}{\partial x_6}$, can be made 0 using the term $A_{(4)}(1,2) = 1$. This procedure leaves us with a $[2 \times 2]$ matrix:

$$\mathbf{A}_{(5)} = \begin{bmatrix} 0 & 1 \\ \frac{\partial f_6}{\partial x_3} & \frac{\partial f_6}{\partial x_6} \end{bmatrix} \tag{6.40}$$

By numerically solving for the eigenvalues of $\mathbf{A}_{(5)}$ for the MPF reference configuration one gets complex eigenvalues, that suggests that they are related to the rotational motion of the parachute payload system. Also in this case, and some other later on, it was demonstrated using the eigenvectors that a certain eigenvalue is related to some particular variables. However, these verifications, whose result is normally obvious from the analysis, will be omitted for brevity. Analytical expressions for the eigenvalues of $\mathbf{A}_{(5)}$ can be determined by solving the characteristic polynomial:

$$\begin{aligned} &\lambda\left(\frac{S_{\text{ref}}\,\rho\,x_5 z_{\text{pc}}\left(C_{D,0}\,z_{\text{pc}} - D_0\,k_{C_m} + z_{\text{pc}}\,k_{C_L}\right)}{2I_{\text{tot}}} - \lambda\right) + \dots \\ &\dots + \frac{S_{\text{ref}}\,\rho\,{x_5}^2\left(C_{D,0}\,z_{\text{pc}} - D_0\,k_{C_m} + z_{\text{pc}}\,k_{C_L}\right)}{2I_{\text{tot}}} = 0 \end{aligned} \tag{6.41}$$

whose solution yields:

$$\begin{aligned} \lambda_\theta &= \frac{x_5}{2}\left(k z_{\text{pc}} \pm \sqrt{k\left(k z_{\text{pc}}^2 - 4\right)}\right), \\ k &= \frac{S_{\text{ref}}\,\rho\left(C_{D,0}\,z_{\text{pc}} - D_0\,k_{C_m} + z_{\text{pc}}\,k_{C_L}\right)}{2I_{\text{tot}}} \end{aligned} \tag{6.42}$$

At this point, however, we still need one eigenvalue of the dynamical system, the one related to the horizontal motion. The information to derive it was lost when the Jacobian was reduced to $\mathbf{A}_{(4)}$, where we neglected the column of the derivatives with respect to x_4. As a result, to be able to calculate λ_{V_y} we need to go back to matrix $\mathbf{A}_{(3)}$:

$$\mathbf{A}_{(3)} = \begin{bmatrix} 0 & 1 & 0 \\ \frac{\partial f_6}{\partial x_3} & \frac{\partial f_6}{\partial x_6} & \frac{\partial f_6}{\partial x_4} \\ \frac{\partial f_4}{\partial x_3} & \frac{\partial f_4}{\partial x_6} & \frac{\partial f_4}{\partial x_4} \end{bmatrix} \tag{6.43}$$

According to the Gaussian elimination method, that is well explained in Press et al. [2007], a matrix can be made block diagonal by means of only row operations. These can be row swap, row subtractions or multiplication of a row by a scalar different from 0. Also, we know from the derivation of the rotational motion eigenvalues, that elements $A_{(3)}(1,1)$, $A_{(3)}(1,2)$, $A_{(3)}(2,1)$ and $A_{(3)}(2,2)$ can be approximated to an independent block. As a result it is true that the horizontal eigenmotion can be represented by a $[1 \times 1]$ block and that the only element in this block is a linear combination of the elements in column 3 of matrix $\mathbf{A}_{(3)}$, i.e., $\frac{\partial f_6}{\partial x_4}$ and $\frac{\partial f_4}{\partial x_4}$.

What we still don' t know, however, are the parameters we need for relating these terms and determine the analytical expression for the horizontal motion eigenvalue. These will be determined experimentally to keep the expression of the eigenvalue as simple as possible. To do so we calculate the eigenvalue λ_{V_y} numerically for the MPF in steady-state flight. The fact that it is real allows us to write it as a linear combination of the elements defining it. We have:

$$\text{Re}\left(\lambda_{V_y,\text{ss}}\right) = \left.\frac{\partial f_6}{\partial x_4}\right|_{\text{ss}} k_{1,o} + \left.\frac{\partial f_4}{\partial x_4}\right|_{\text{ss}} k_{2,o} \tag{6.44}$$

One of the parameters can be determine as a function of the other:

$$k_{2,o} = \frac{\mathrm{Re}\left(\lambda_{V_y,\mathrm{ss}}\right) - \left.\frac{\partial f_4}{\partial x_4}\right|_{\mathrm{ss}} k_{1,o}}{\left.\frac{\partial f_6}{\partial x_4}\right|_{\mathrm{ss}}} \tag{6.45}$$

The approximated analytical λ_{V_y} eigenvalue is then given by:

$$\lambda_{V_y} = \frac{S_{\mathrm{ref}}\,\rho\,x_5}{2}\left(-\frac{\left(C_{D,0}+k_{C_L}\right)z_{\mathrm{pc}} - k_{C_m}D_0}{I_{\mathrm{tot}}}k_{1,o} + \frac{C_{D,0}+k_{C_L}}{m}k_{2,o}\right) \tag{6.46}$$

where the coefficients $k_{1,o}$ and $k_{2,o}$, determined by means of an optimization that minimizes the error between the analytical and numerical eigenvalues for the MPF reference vehicle flying in steady-state conditions, are:

$$k_{1,o} = 0.047611578, \quad k_{2,o} = 0.489989999 \tag{6.47}$$

The analytical eigenvalues given by Eq. (6.36), (6.42) and (6.46) yield accurate results for the dynamics of the MPF reference vehicle in steady-state descent, as Figure 6.3 shows. In particular, while λ_{V_z} eigenvalue is exact, the approximation introduced to derive λ_θ causes errors in the order of 2% for both the real and imaginary parts. Also, the introduction of the coefficients $k_{1,o}$ and $k_{2,o}$ causes an error for λ_{V_y} calculated analytically always smaller than 0.015% throughout the descent with respect to the case in which it is defined numerically. These coefficients, as said, have been determined for the MPF reference vehicle, so that if its configuration changes then the error of the λ_{V_y} eigenvalue will grow. Nevertheless, even large variations (up to ±100% with respect to MPF reference value) in vehicle mass and geometry or aerodynamic parameters, cause an additional relative error in the order of 1%. These facts all together demonstrate that the analytical definition of the eigenvalues derived for the parachute-payload system is consistent and can be used for further analysis.

Figure 6.3 shows on the left hand side the relative error of the approximated analytical eigenvalues of the parachute-payload system with respect to the same eigenvalues calculated numerically without any approximation along a steady-state trajectory. On the right hand side is depicted how the eigenvalues associated to the system, determined using Eq. (6.36), (6.42) and (6.46), vary along the steady-state trajectory of the spacecraft. The sample trajectory consists in a vertical flight with IC: $\gamma_0 = -90°$, $\theta_0 = -90°$, $\dot{\theta}_0 = 0°/\mathrm{s}$, $V_0 = 120\ \frac{\mathrm{m}}{\mathrm{s}}$, $z_0 = 6000$ m, $y_0 = 0$ m.

The first interesting aspect to notice about the dynamics of the system is that for our reference configuration the eigenvalues λ_θ are complex and conjugate, with negative real part. This results in the fact that the rotational eigenmotion is periodical and converges to the equilibrium point. For this eigenmotion it is possible to determine the natural frequency ω_θ, the damping factor ζ_θ and the period P_θ according to Eq. (6.6). After some rearrangements we get:

$$\omega_\theta = |x_5|\sqrt{k} \tag{6.48}$$

$$\zeta_\theta = \frac{\sqrt{k}z_{\mathrm{pc}}}{2} \tag{6.49}$$

$$P_\theta = \frac{4\pi}{|x_5|\sqrt{k\left(kz_{\mathrm{pc}}^2 - 4\right)}} \tag{6.50}$$

where the recurring parameter k is given by:

$$k = \frac{S_{\mathrm{ref}}\,\rho\left(\left(C_{D,0}+k_{C_L}\right)z_{\mathrm{pc}} - D_0\,k_{C_m}\right)}{2I_{\mathrm{tot}}} \tag{6.51}$$

These formulas confirm the physical expectations about the attitude behaviour of the parachute-payload system. It is clear that the characteristics of the pendulum motion mode of the spacecraft result from the balance between the inertia properties of the body and the effect of the aerodynamic forces, mathematically

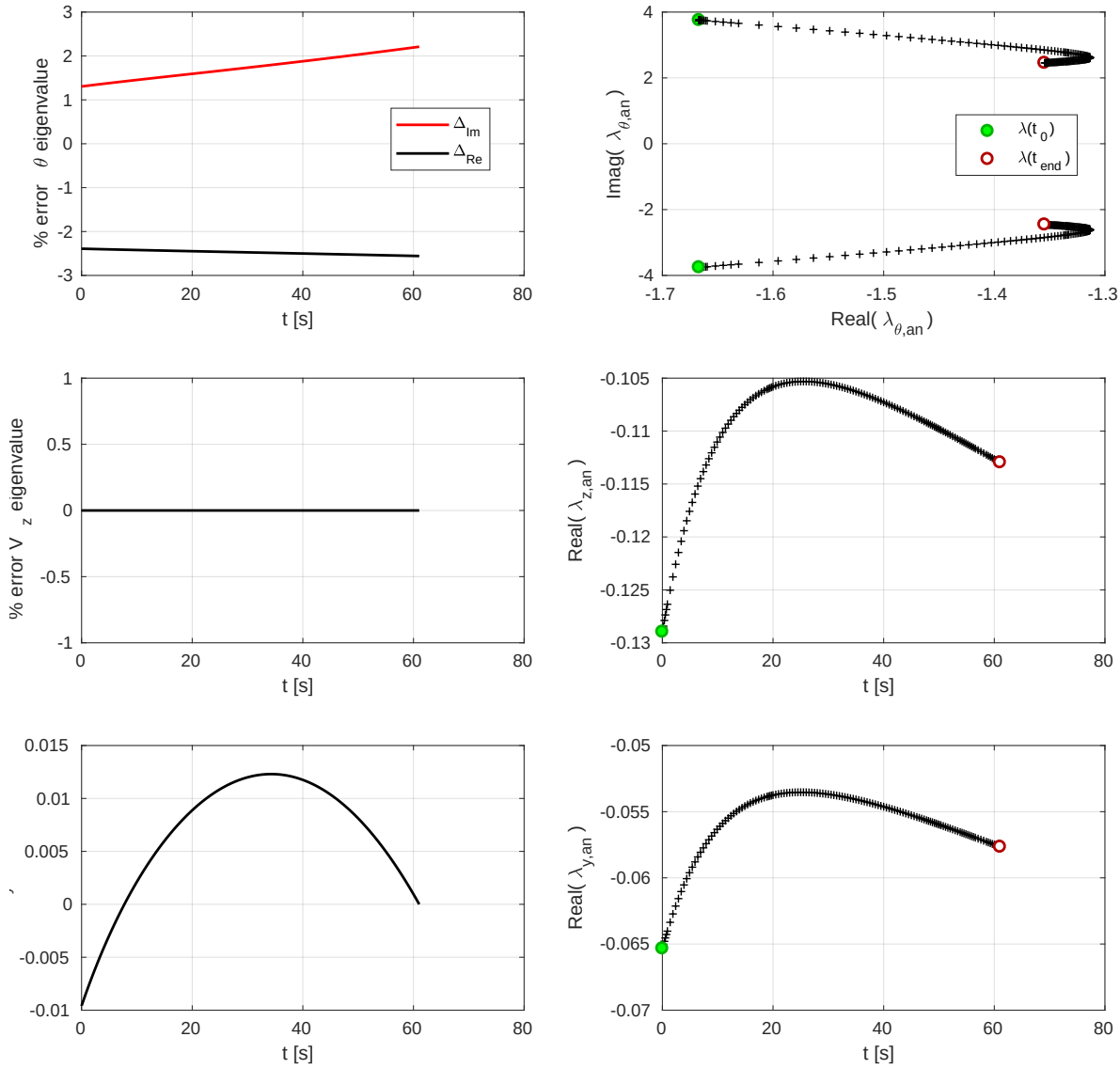

Figure 6.3: Eigenvalue analysis for the steady-state flight of the open-loop rigid body MPF reference vehicle.

Table 6.1: MPF open-loop descent system attitude stability characteristics in the steady-state point $\mathbf{x}_{ss}$ (from Eq. (6.13)).

Property	Value
P_θ	2.52 s
ω_θ	2.85 $\frac{\text{rad}}{\text{s}}$
ζ_θ	0.48

expressed by the parameter k. In general, a larger k, corresponding to a predominance of the aerodynamic contributions, results in higher frequency and better damped oscillations. If k is smaller the situation is opposite but external perturbations have a lower impact on the attitude of the system.

With respect to the single parameters appearing in Eq. (6.48) to (6.51), it is easy to notice that larger (in magnitude) $C_{D,0}$, k_{C_L} and k_{C_m} coefficients all contribute to an increase of the relative weight of the aerodynamic effect. On the other hand, the interpretation of the influence of the parameters z_{pc} and D_0, respectively the distance of the body COM from the parachute and its radius, is not straightforward because they influence both the aerodynamic and inertia properties of the system. Finally, smaller vertical velocity x_5 and atmospheric density ρ are responsible for a lower dynamic pressure and clearly this causes the aerodynamic contribution to lose importance.

The characteristics of the oscillatory motion of the parachute-payload system, i.e., the oscillatory period, frequency and damping ratio, have been calculated for the MPF reference configuration in the linearisation point given by Eq. (6.13) using Eq. (6.48) to (6.50). The resulting values are stored in Table 6.1. Clearly, these numbers would change in case the parameters of the MPF reference vehicle vary and also along the trajectory. This is the result of a varying dynamic pressure and, in agreement with the discussion of the previous paragraphs, a varying ratio between the aerodynamic and inertia properties of the system.

By looking once more at Figure 6.3 it is possible to notice that λ_{V_y} and λ_{V_z}, for the considered reference case, are real and negative. This suggests that the vertical and horizontal velocities will simply exhibit a converging monotonous behaviour. Also, the figure shows that there is a point in which these values are maximum and, as a result, the V_z and V_y are less stable around the respective equilibrium positions. This maximum corresponds to the condition in which the dynamic pressure, during the descent flight, reaches a minimum. This minimum is due to the fact that the vertical velocity x_5 has reduced due to the drag dissipation but the density ρ has not yet increased significantly as a result of the lower altitude.

The balance between aerodynamic and inertia properties of the system is also visible from an analysis of the equations expressing the eigenvalues for the vertical and horizontal velocity. In particular, the interpretation of Eq. (6.36) is straightforward. Larger $C_{D,0}$ and S_{ref} and lower m result in the fact that the vertical velocity, once perturbed, tends back faster to the equilibrium velocity. Eq. (6.46) for the horizontal velocity eigenvalue is more interesting. It is characterized by two terms. The second term, that has m at the denominator, implies a stability behaviour analogous to that of the vertical velocity. The first term is instead due to the influence of the attitude of the vehicle on its horizontal eigenmotion. This is physically consistent. In fact, differently from the case of the vertical velocity, when the horizontal velocity is perturbed, then the angle of attack of the spacecraft varies. The resulting lateral aerodynamic forces cause it to incline in the airspeed direction. This effect, however, has opposite sign with respect to that due to the second term and is thus destabilising for the horizontal velocity of the system. This destabilization most probably derives from the fact that when the vehicle reorientates in the direction of the airspeed, the angle of attack caused by the presence of the perturbation reduces. As a result the magnitude of the aerodynamic forces that had grown in horizontal direction, and that are responsible for the deceleration to V_y =0 just after the perturbation, reduce as well and the convergence to the equilibrium condition is less prompt. Nevertheless, the fact that $k_{1,o} << k_{2,o}$ suggests that this destabilizing effect has a much smaller magnitude with respect to that due to the second term.

7

RIGID BODY CLOSED-LOOP STABILITY

The objective of the present Master Thesis project, as introduced in Chapter 2, is to evaluate whether a control system exploiting the force generated by the backshell thrusters can represent a performing and efficient solution for guiding the a parachute-payload spacecraft during the descent in the atmosphere of Mars. This chapter is dedicated to the definition and preliminary evaluation of a guidance concept that satisfies the system requirements listed in Table 2.2.

After a preliminary discussion about feedback control, Section 7.1 introduces the guidance system concept. The resulting system is optimized and analytically investigated, with techniques analogous to those already used for the open-loop system in Section 6.2, in Section 7.2.

7.1. GUIDANCE

As already explained in Section 2.2, the size of the landing ellipse for a Mars landing mission depends on a number of factors. Among these there are the wind drift effect during the parachute descent and the navigation error that gets accumulated during all the three EDL mission phases. The main objective of the guidance logic we want to design is to control the horizontal position of the parachute-payload system during the descent flight by means of backshell thrust. In this way the wind drift effect can be counteracted and the position error already present at parachute deployment can be reduced.

The results of the open-loop stability analysis in Chapter 6 have proved, as it was expected, that for a parachute-payload system like the MPF, the attitude and the horizontal and vertical velocities of the system are all naturally stable during the steady-state flight in the atmosphere of Mars. The horizontal and vertical position components, however, do not have the same property. This means that there is not an equilibrium YZ-position the uncontrolled spacecraft automatically tends to. The control system we are going to design and integrate in the existing dynamic models, as said, will have the purpose of stabilizing the horizontal motion of the system so that, if it is subjected to an external disturbance, it will tend back to the equilibrium y-position that is given in input to the controller. Also, it is required that the eventual negative influence of the control action does not compromises other aspects of the dynamics of the system.

Of course, it would also be possible to design a guidance and control system that can control the vertical motion of the vehicle. In fact, the size of the landing ellipse is also influenced by the fact that the vertical velocity at a certain altitude is different from its nominal value, for example due to vertical winds or navigation errors causing a late parachute deployment and a consequent late deceleration. However, the time constraints for the Master Thesis project would not allow an in depth study of both vertical and horizontal closed-loop parachute-payload system stability behaviour, so that a choice had to be made. First, it was considered that a system that used backshell thrust to reduce vertical speed before touchdown was already equipped on the MPF. This means that vertical motion control would not have been an absolute novelty, while instead the control of the horizontal motion, up to this point, has never been integrated on any mission. Also, the information gathered in Section 6.2 have shown that a parachute-payload system similar to MPF ensures very good vertical velocity damping capabilities. In addition to this, the plane on which the landing ellipse lies is parallel to the horizontal Y_I-axis, this suggesting that the capability to control the horizontal motion of the system could influence much more significantly its size with respect to the vertical control. Finally, studying the impact of horizontal thrust pushes on the attitude dynamics of the non-rigid descent spacecraft is much more interesting from the attitude

stability point of view because, as already mentioned, the parachute-payload system is particularly sensitive to horizontal perturbations. Considering these, from now on we will focus on horizontal motion control.

Before to discuss the guidance concept, however, some considerations, that directly follow from the purpose of the study, have to be introduced. The final output of the study will include information on the performances that can be achieved with such a system, data on how horizontal thrust influences the dynamics of the spacecraft and parachute-payload systems design headlines to favourish the integration of active control on future systems. In fact, no existing literature about the use of backshell thrust for horizontal parachute descent control purposes is available up to the present moment. Assuming this, it is clear that analytical results can yield additional insight into this new problem. This is why the guidance system that will be designed and examined will have, as a main requirement, simplicity. In this way it will possible to treat the closed-loop system analytically and focus the attention on its dynamic behaviour. In particular, in this section we will limit ourselves to studying the dynamics of the controlled parachute-payload system only during the steady-state flight, similarly to Section 6.2, once more using the 3DOF rigid body model described in Section 3.2.

The first thing to choose is the configuration of the control thrusters on the backshell. Since the vehicle in steady-state conditions flies vertically and we want the system to be as simple as possible, we assume that the thrusters always push perpendicularly to the symmetry axis of the backshell. For the case of the rigid body model then the thrust force $\mathbf{T}$ is perpendicular to the Z_B-axis that is the rotational symmetry axis of the whole parachute-payload system. With respect to the body frame B, we have:

$$\mathbf{T}_B = \begin{pmatrix} 0 \\ T \\ 0 \end{pmatrix} \tag{7.1}$$

and, by rotating frame B clockwise of an angle $\frac{\pi}{2} - (-\theta)$ around the X_B-axis, with the thrust vector can be expressed with respect the inertial frame I:

$$\mathbf{T}_I = \begin{bmatrix} 1 & 0 & 0 \\ 0 & \cos\left(\frac{\pi}{2}+\theta\right) & -\sin\left(\frac{\pi}{2}+\theta\right) \\ 0 & \sin\left(\frac{\pi}{2}+\theta\right) & \cos\left(\frac{\pi}{2}+\theta\right) \end{bmatrix} \begin{pmatrix} 0 \\ T \\ 0 \end{pmatrix} = \begin{pmatrix} 0 \\ -T\sin\theta \\ T\cos\theta \end{pmatrix} \tag{7.2}$$

The backshell thrust $\mathbf{T}$ also has an effect on the rotational equilibrium. By assuming that it is applied in the COM of the backshell, whose position in the B frame is:

$$\mathbf{L}_{\text{bs}} = \begin{pmatrix} 0 \\ 0 \\ z_{\text{bs}} \end{pmatrix} \tag{7.3}$$

The moment that the thrust generates around the parachute-payload system COM is:

$$\mathbf{M}_{\text{T}} = \mathbf{L}_{\text{bs}} \times \mathbf{T}_B = \begin{pmatrix} 0 \\ 0 \\ z_{\text{bs}} \end{pmatrix} \times \begin{pmatrix} 0 \\ T \\ 0 \end{pmatrix} = -Tz_{\text{bs}}\hat{\mathbf{x}}_B \tag{7.4}$$

By including the effect of control thrust T in Eq. (3.28) and (3.41), in which the added mass effect has been introduced, we get:

$$\begin{aligned} \ddot{y} &= \frac{-L\cos\gamma - D\sin\gamma - T\sin\theta}{m_g + m_a} \\ \ddot{z} &= \frac{m_g g + L\sin\gamma - D\cos\gamma + T\cos\theta}{m_g + m_a} \\ \ddot{\theta} &= \frac{(-L\cos\alpha - D\sin\alpha)z_{\text{COP}} + M - Tz_{\text{bs}}}{I_{X_B} + I_{a,X_B}} \end{aligned} \tag{7.5}$$

Equations (7.5) introduce in the system the effect of the backshell thrust. An analogous procedure was also adopted for modifying the EOM describing the dynamics of the single backshell in the multibody model given by Eq. (3.61).

Up to now, however, the thrust force has not been defined as a function of the state variables as, for example, the aerodynamic forces are. To control the dynamic evolution of the system, the command can be calculated externally, parametrized with respect to some peculiar variable characterizing the evolution of the system, e.g., the altitude, the dynamic pressure or the time, and given to the system as an external input. However, it is also possible to define the control input T so that it is proportional to the estimated value of one or more elements of the state vector. In this case we are dealing with a feedback controller and a closed-loop system. Feedback controllers can be simple, versatile, offer good performance and are perfectly suitable for deriving analytical results, so that we choose to implement one for stabilizing the horizontal motion of our parachute-payload spacecraft.

7.1.1. STATE AND OUTPUT FEEDBACK

The working principle of a feedback controller consists of taking in input the state or the output of a system, that in control engineering jargon is called *plant*, and compare it with a commanded signal, i.e., the desired state or output. The difference between these two quantities yields an error value that the controller has to nullify by generating an appropriate input for the actuators of the plant.

The dynamic evolution of a linear controlled dynamic system, whose state is determined by the $n\times 1$ vector $\mathbf{x}$, controlled using the $m\times 1$ control vector $\mathbf{u}$, is described by the *dynamics equation*:

$$\dot{\mathbf{x}} = \mathbf{A}\mathbf{x} + \mathbf{B}\mathbf{u} \tag{7.6}$$

where $\mathbf{A}$ is the state matrix, analogous to that already defined for the system given by (6.7), and $\mathbf{B}$ is the control coefficient matrix. They have dimensions respectively $n \times n$ and $n \times m$. In this case the system is said to be written in *state-space form*. The output of the system is instead defined by the *output equation*:

$$\mathbf{y} = \mathbf{C}\mathbf{x} + \mathbf{D}\mathbf{u} \tag{7.7}$$

in which $\mathbf{y}$ is the $k \times 1$ output vector, and $\mathbf{C}$ and $\mathbf{D}$ are the output and direct transmission matrices, with dimensions $k \times n$ and $k \times m$ respectively.

Even if it is possible to describe a nonlinear system in *state-space form*, classical control theory has been developed for linear systems. As explained in Section 6.1.3, under certain conditions a nonlinear system can be studied using linear techniques. In particular, its $\mathbf{A}$, $\mathbf{B}$, $\mathbf{C}$, and $\mathbf{D}$ matrices are normally determined after linearisation of the EOM describing the system to be controlled. In such a case the state vector $\mathbf{x}$ and the output vector $\mathbf{y}$ are substituted in Eq. (7.6) and (7.7) by the state error vector $\bar{\mathbf{x}}$ and the output error vector $\bar{\mathbf{y}}$ that define, respectively, the difference of the state and output of the system with respect to a certain reference. In other words, when a system is linearised it is the state error and output error that evolve linearly in the vicinity of the linearisation point. From now on, we will assume that we are dealing with a linearised system and that the $\mathbf{A}$, $\mathbf{B}$, $\mathbf{C}$, and $\mathbf{D}$ matrices are constant, this making the system also *time invariant*. Also, as for the majority of dynamic systems, it is possible to assume that $\mathbf{D} = 0$, this making the implementation of the controller much easier.

The control action of a controller can be either proportional to its output (or output error) or to its state (or state error). In the following, as explained in Section 7.1.4, we will implement a *state-feedback controller*. In our case the control action will be somehow proportional to the state error vector $\bar{\mathbf{x}}$. The control law is:

$$\mathbf{u} = -\mathbf{K}\bar{\mathbf{x}} \tag{7.8}$$

in which $\mathbf{K}$ is the gain matrix. After substitution of Eq. (7.8) in Eq. (7.6) we get:

$$\dot{\bar{\mathbf{x}}} = (\mathbf{A} - \mathbf{B}\mathbf{K})\,\bar{\mathbf{x}} = \mathbf{A}^*\bar{\mathbf{x}} \tag{7.9}$$

where $\mathbf{A}^*$ is the state matrix of the closed-loop system. Its eigenvalues λ directly depend on the gain matrix $\mathbf{K}$. They can be determined by solving the associated equation:

$$\det\left|\mathbf{A}^* - \lambda\mathbf{I}\right| = \det|\mathbf{A} - \mathbf{B}\mathbf{K} - \lambda\mathbf{I}| = 0 \tag{7.10}$$

In summary, the control action consists of modifying the eigenvalues and eigenvectors of the state matrix $\mathbf{A}$ by means of the gain matrix $\mathbf{K}$ and control matrix $\mathbf{B}$. For a certain $\mathbf{B}$, then the control problem reduces to the determination of $\mathbf{K}$ in such a way that the system will behave as desired.

7.1.2. CONTROLLER PERFORMANCE ANALYSIS

The response of a control system can be written as:

$$c(t) = c_{tr}(t) + c_{ss}(t) \tag{7.11}$$

in which c_{tr} is called *transient response* and represents the system response from the initial to the final state and c_{ss} is the *steady-state response* that characterizes the behaviour of the system for $t \to \infty$. In general, it is the transient response that most characterizes the performance characteristics of a controller. To measure these performance characteristics the system is given a unit-step input, that is easy to generate, when it is at rest. In fact, if the transient response of a linear system to a unit-step input is known then it is mathematically possible to reconstruct the response to an arbitrary input that indeed can be modelled as a series of sequential unit-step inputs.

First of all, the dynamic response of a system is characterized by oscillations with a frequency that is called natural frequency ω_n. The damping ratio ζ is instead a measure of how well these oscillations are damped by the system. For a second-order system $0.4 \leq \zeta \leq 0.8$ is desirable. Indeed, systems with $\zeta \leq 0.4$ are characterized by excessive overshoot, while, on the other hand if $\zeta \geq 0.8$ the response will be sluggish. These two parameters can be determined as a function of the eigenvalues of the model matrix $\mathbf{A}$ of the system, as already introduced in Section 6.1.

The performance criteria thanks to which it is possible to evaluate the characteristic response of the system a unit-step impulse, depicted in Figure 7.1, are defined as follows [Ogata, 2010]:

1. *Delay time t_d:* time required for the response to reach half the final value the very first time. According to Golnaraghi and Kuo [1987] for an overdamped system it can be estimated as:

$$t_d \approx \frac{1 + 0.7\zeta}{\omega_n}, \quad 0 < \zeta < 1 \tag{7.12}$$

2. *Rise time t_r:* time required for the response to rise from 10% to 90%, 5% to 95%, or 0% to 100% of its final value. For underdamped second-order systems,the 0% to 100% rise time is normally used. For overdamped systems the 10% to 90% rise time can be estimated, asccording to Golnaraghi and Kuo [1987], as:

$$t_r \approx \frac{0.8 + 2.5\zeta}{\omega_n}, \quad 0 < \zeta < 1 \tag{7.13}$$

3. *Peak time t_p:* time required for the response to reach the first peak of the overshoot.

4. *Maximum overshoot M_p:* maximum peak value of the response curve measured from unity. If the final steady-state value of the response differs from unity, then it is common to use the maximum percent overshoot. The amount of the maximum (percent) overshoot directly indicates the relative stability of the system.

5. *Settling time t_s:* time required for the response curve to reach and stay within a range about the final value of size specified by an absolute percentage of the final value (usually 2% or 5%). The settling time is related to the largest time constant of the control system. Once more Golnaraghi and Kuo [1987] give an estimation of this parameter as a function of the system natural frequency and damping ratio. For a threshold of 5% it the settling time can be estimated as:

$$t_s \approx \begin{cases} \frac{3.2}{\zeta\omega_n}, & 0 < \zeta < 0.69 \\ \\ \frac{4.5\zeta}{\omega_n}, & \zeta > 0.69 \end{cases} \tag{7.14}$$

In addition to these transient response performance criteria, also the *steady-state error*, consisting of the error between the state on which the system stabilizes for $t \to \infty$ and the desired state is something to minimize when designing a control system.

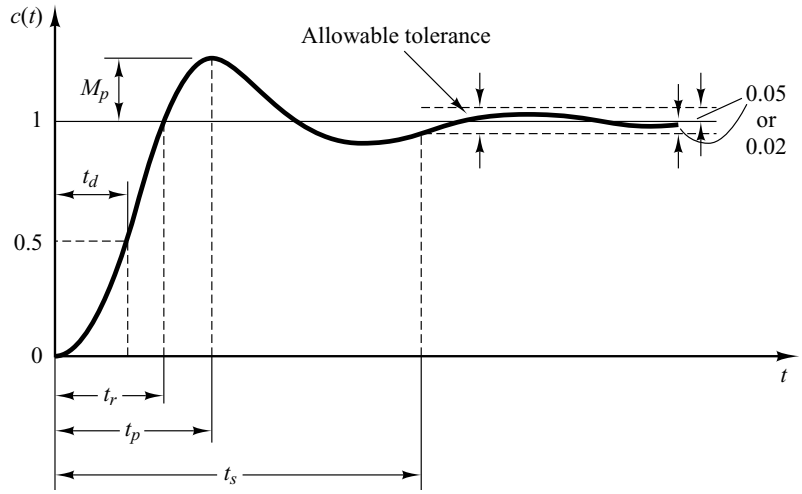

Figure 7.1: Feedback control transient response and steady-state response performance criteria [Ogata, 2010].

7.1.3. PID CONTROL

The *PID controller* is the most commonly used closed-loop feedback controller. It takes in input an error signal $\mathbf{e}(t)$ and produces a control signal $\mathbf{u}(t)$ so that to drive this error to zero. However, the PID algorithm does not guarantee optimal control nor system stability. It is particularly good for applications were uncertainties play a significant role.

As for any other feedback-control system, also for the PID controller the parameters that determine its performance characteristics are the gains. As said, these can be either constant during the whole mission or can be parametrized according to a specific variable. It is remarked, however, that parametrization with respect to time, for the majority of applications, could be a badly performing choice since uncertainties, such as winds, could shift the critical mission variables with respect to the time schedule. For gain scheduling in aerospace applications the dynamic pressure, the altitude or the Mach number are more appropriate.

Assuming now we are dealing with a single-input single-output (SISO) system, the one-dimensional control signal $u(t)$ can be written as:

$$u(t) = K_p e(t) + K_i \int_0^t e(\tau) d\tau + K_d \frac{de(t)}{dt} \tag{7.15}$$

from which is clear that the control action is the sum of three different contributions. These are:

1. *Proportional action:* this control signal contribution is directly proportional to the error signal. It resembles the behaviour of an amplifier. However, if K_p is too large then the system could be unstable but if it is too small the response will be too slow.

2. *Integral action:* the control signal contribution is in this case proportional to the accumulation of past errors. The integral contribution causes an increase in overshoot but reduces or removes steady-state error. Large K_i values can result in a growth of the error and, eventually, can cause saturation, in which case a small error signal triggers a large control action. To avoid this it is possible to realize a controller that deactivates the integral action when the error signal is small.

3. *Derivative action:* in this case the control signal contribution is proportional to the prediction of future error based on its current rate of change. The derivative contribution slows down the rate of change of the controller output, i.e., the transient response, by augmenting the controller stability but is not effective for slowly varying error signals. A larger K_d can reduce overshoot but yields could have an unfavourable influence on the steady-state error.

The gains of the PID controller can be determined in many ways. For example the Ziegler-Nichols tuning rules, available from Ogata [2010], define an heuristic method to determine the gains with a low effort that is based on the transient response characteristics of the controlled plant. The most straightforward method, however, is to simulate the dynamics of the closed-loop system and tune the gains so that to obtain the desired step or impulse response.

7.1.4. PARACHUTE-PAYLOAD HORIZONTAL POSITION CONTROL

In agreement with the requirements introduced in Section 2.5 and the discussion at the beginning of this section, we require our controller to stabilize the horizontal position of the parachute payload system. This means that the control signal shall be proportional to the horizontal position error. In addition to this, we also want to avoid that at the end of the parachute descent, when the terminal descent engines need to be ignited for decelerating the payload until it reaches touchdown velocity, the system still features a significant horizontal velocity. This can be avoided if the control signal is also proportional to the error of the horizontal velocity with respect to the reference, that clearly will be 0. According to these, we would have a control input that is proportional to the horizontal position error and to its true, not numerically estimated, time derivative, i.e., the error of the estimated horizontal velocity. The resulting PD controller, with appropriately tuned gains, can ensure a satisfactory responsiveness and low overshoot, while still maintaining the fundamental characteristic of simplicity we need for deriving analytical results.

It is remarked that the control signal is in reality proportional to the estimated state. The estimated state corresponds to the actual state that is estimated by the navigation system and is thus affected by a navigation error. If however the purpose is to study the controlled system closed loop stability, we can for now neglect the navigation error and consider it in a later stage of the work. Assuming these, the control signal for our specific case can be written as:

$$u = T = -\mathbf{K}\bar{\mathbf{x}} = -\begin{bmatrix} K_p & 0 & 0 & K_d & 0 & 0 \end{bmatrix} \begin{pmatrix} \bar{x}_1 \\ \bar{x}_2 \\ \bar{x}_3 \\ \bar{x}_4 \\ \bar{x}_5 \\ \bar{x}_6 \end{pmatrix} = -K_p \bar{x}_1 - K_d \bar{x}_4 \tag{7.16}$$

in which $\bar{x}_i$, for $i = 1,...,6$ indicate the displacement of the state vector elements with respect to their references.

What still remains to determine is the reference trajectory with respect to which the state vector error $\bar{\mathbf{x}}$ can be calculated. We assume to this is a simple vertical trajectory along the Z_I-axis. In this way both the horizontal position and velocity reference values are constant and equal to 0. This choice is realistic, because it corresponds to an undisturbed parachute descent steady-state trajectory and is particularly appropriate for the purpose of deriving analytical results and for studying the performance characteristics of the closed-loop systems.

For real applications, however, the values that the controller uses as a reference for the state variables of the system and the control strategy should adapt to different flight situations. For example, if the reference is kept constant, it is possible that when the target altitude is reached, the control input is still dominated by the position error and the horizontal velocity is large. A possible solution to this problem would be stop the control action before to reach the target so that the system naturally tends back to the vertical flight condition. Another possible strategy would be to reschedule the target as the farthest point that the system can reach without violating certain constraints, eventually also taking into account the effect of wind. These considerations are not needed for the purpose of studying the feasibility of the parachute horizontal position control concept from the points of view of efficiency, dynamic stability and achievable nominal performance, but should be taken into account for designing a control algorithm that can be equipped on a real spacecraft, that represents the next step of the technology development.

7.2. STABILITY ANALYSIS

In this section the motion of the closed-loop parachute-payload system will be analysed. A similar approach to that used in Section 6.2 will be applied, with the only difference consisting in the fact that now the 3DOF rigid body model, that is appropriate for deriving analytical results, will also include the thrust contribute. The gain optimization for the controller will also be carried out within this section, after the system linearisation, because it is based on the analysis of the linear response of the system, and before than the derivation of the analytical expressions for the eigenvalues of the system, since the values of the gains are needed for this last task.

7.2.1. SYSTEM LINEARISATION

To study the stability properties of the controlled parachute-payload system once more we start by linearising it and then to analyse its eigenmotion. The EOM to linearise, given by Eq. (7.5), now include the thrust force. We want to translate this nonlinear system to its state-space form, given by:

$$\dot{\bar{\mathbf{x}}} = \mathbf{A}\bar{\mathbf{x}} + \mathbf{B}\mathbf{u} \tag{7.17}$$

Matrix **A** for the closed-loop system is equivalent to the Jacobian already defined for the open-loop system, whose elements are given by Eq. (6.32), because it is calculated in the steady-steady condition that in our case, amongst others, requests the thrust magnitude T to be 0. The input matrix **B** is instead defined as:

$$\mathbf{B} = \frac{\partial \mathbf{f}}{\partial \mathbf{u}} \tag{7.18}$$

where **f** is the system of nonlinear equations consisting of the first three elements of Eq. (6.10) and the EOM from (7.5). In our case the control vector **u** is simply the thrust magnitude T, so that if the same assumptions already introduced for deriving the simplified version of the **A** matrix in Section 6.2.1 are also used for determining **B**, we get:

$$\mathbf{B} = \begin{bmatrix} 0 \\ 0 \\ 0 \\ -\frac{\sin x_3}{m} \\ \frac{\cos x_3}{m} \\ -\frac{z_{\text{bs}}}{I_{\text{tot}}} \end{bmatrix} \tag{7.19}$$

By inserting Eq. (7.19), (7.16) and (6.32) in (7.9) it is possible to determine the elements of matrix $\mathbf{A}^*$ describing the controlled parachute-payload linearised system. These are:

$$\begin{aligned}
&A^*_{11} = 0, \quad A^*_{12} = 0, \quad A^*_{13} = 0, \quad A^*_{14} = 1, \quad A^*_{15} = 0, \quad A^*_{16} = 0; \\
&A^*_{21} = 0, \quad A^*_{22} = 0, \quad A^*_{23} = 0, \quad A^*_{24} = 0, \quad A^*_{25} = 1, \quad A^*_{26} = 0; \\
&A^*_{31} = 0, \quad A^*_{32} = 0, \quad A^*_{33} = 0, \quad A^*_{34} = 0, \quad A^*_{35} = 0, \quad A^*_{36} = 1; \\
&A^*_{41} = \frac{\sin x_3 K_p}{m}, \quad A^*_{42} = 0, \quad A^*_{43} = \frac{S_{\text{ref}} \rho x_5^2}{2m}, \\
&A^*_{44} = \frac{S_{\text{ref}} \rho x_5 \left(C_{D,0} + k_{C_L}\right)}{2m} + \frac{\sin x_3 K_d}{m}, \quad A^*_{45} = 0, \quad A^*_{46} = -\frac{S_{\text{ref}} \rho x_5 \left(C_{D,0} + k_{C_L}\right)}{2m}; \\
&A^*_{51} = \frac{\cos x_3 K_p}{m}, \quad A^*_{52} = 0, \quad A^*_{53} = 0, \quad A^*_{54} = -\frac{\cos x_3 K_d}{m}, \quad A^*_{55} = \frac{C_{D,0} S_{\text{ref}} \rho x_5}{m}, \quad A^*_{56} = 0; \\
&A^*_{61} = -\frac{z_{\text{bs}} K_p}{I_{\text{tot}}}, \quad A^*_{62} = 0, \quad A^*_{63} = -\frac{S_{\text{ref}} \rho x_5^2 \left(\left(C_{D,0} + k_{C_L}\right) z_{\text{pc}} + k_{C_m} D_0\right)}{2 I_{\text{tot}}}, \\
&A^*_{64} = -\frac{S_{\text{ref}} \rho x_5 \left(\left(C_{D,0} + k_{C_L}\right) z_{\text{pc}} + k_{C_m} D_0\right)}{2 I_{\text{tot}}} + \frac{z_{\text{bs}} K_d}{I_{\text{tot}}}, \quad A^*_{65} = 0, \\
&A^*_{66} = \frac{S_{\text{ref}} \rho x_5 \left(\left(C_{D,0} + k_{C_L}\right) z_{\text{pc}} + k_{C_m} D_0\right) z_{\text{pc}}}{2 I_{\text{tot}}};
\end{aligned} \tag{7.20}$$

Also in this case the consistency of the linear system expressed by matrix $\mathbf{A}^*$ has been validated, using sample controller gains, by verifying that the error between its step, initial conditions and impulse responses of the variables having a constant equilibrium position, i.e., y V_y, V_z, θ and $\dot{\theta}$, and the corresponding responses of the nonlinear controlled system was negligible.

7.2.2. GAIN TUNING

To get appropriate gains for the PD controller several options are available. Some methods yield the gains optimized according to a specific cost function while others instead give a first estimation of the gains depending on some specific parameters of the system to be controlled. Clearly, the latter methods are generally faster

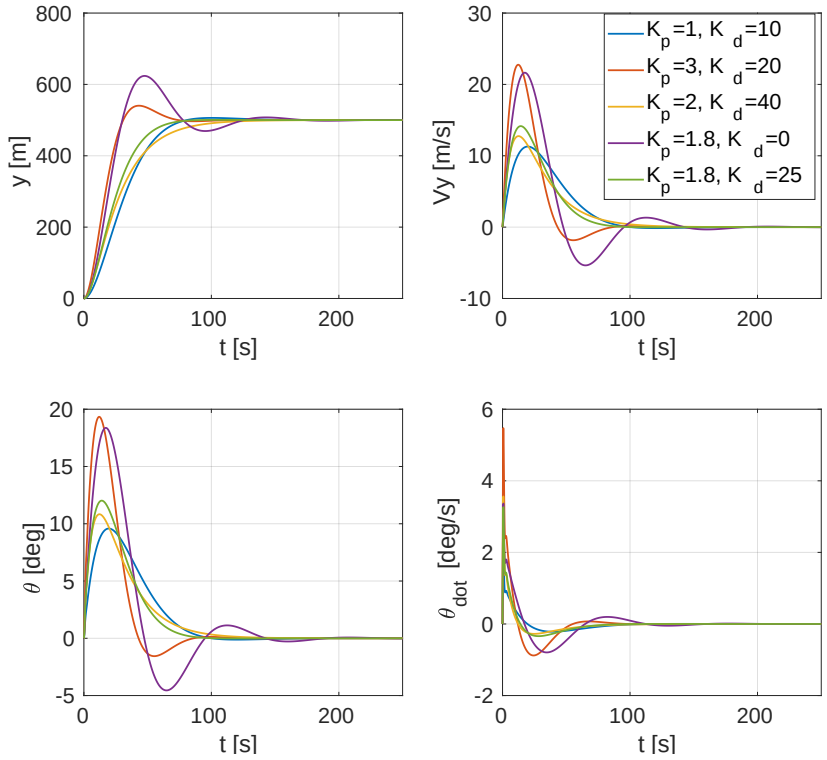

Figure 7.2: Parachute-payload linear system response for different K_p and K_d gains.

but less accurate. Another very much used strategy is to exploit the linear response to tune, by trial and error, the gains for the linear system. This approach is particularly appropriate when the response of the system depends on a limited number of gains and when controller optimality is not a key requirement.

The present project aims at evaluating the feasibility of controlling, with propulsive actuators, the horizontal position of the spacecraft during the parachute descent, so that a highly optimal controller is not needed. In addition to this, the PD controller has only two gains and the linear system to use for response analysis, expressed by Eq. (7.22), has already been developed and proved to be valid. The choice of applying trial and error for tuning the controller gains seems to be the most appropriate.

Figure 7.2 shows the response of the linearised parachute-payload closed-loop system for different proportional and derivative gains K_p and K_d. For this analysis a sample error of 500 m in the horizontal position y has been given in input to the system as initial condition. To tune the gains we need to focus mainly on the the response of y that is the variable we want to stabilize through the use of a controller. Despite this, also the response of the others is significant. In general, it is possible to notice that a larger K_p causes a faster response but also increases the overshoot. This, in turn, can result in a higher fuel consumption for the guidance system whose control force is thrust. The K_d gain, instead, contributes to limiting the overshoot but lowers the responsiveness. A good compromise for having minimum rise time and almost no overshoot is $K_p = 1.8$ and $K_d = 25$. These controller gains will be used as reference values in the following analyses.

7.2.3. EIGENMOTION ANALYSIS

The linear system described by Eq. (7.20) is simple. It can be used for response analysis and, in turn, for tuning the gains K_p and K_d of the PD controller according to the requirements for the MPF parachute-payload guidance system, as has been done in Section 7.2.2. This optimization has yielded $K_p = 1.8$ and $K_d = 25$. In addition to this, we know that for the reference vehicle MPF the backshell position along the Z_B-axis with respect to the body COM is $z_{\text{bs}} = 3.04$ m while its total moment of inertia, also considering the added mass inertial effect calculated in the steady-state point, is $I_{\text{tot}} \approx 1500$ kgm^2. Considering these, the following holds for the terms due to the control action in row 6 of $\mathbf{A}^*$:

$$\frac{z_{\text{bs}} K_p}{I_{\text{tot}}} = 0\left(10^{-3}\right), \quad \frac{z_{\text{bs}} K_d}{I_{\text{tot}}} = 0\left(10^{-2}\right) \tag{7.21}$$

By introducing in $\mathbf{A}^*$ the parameters of the MPF for the steady-state condition, it has been checked that all the other terms appearing in the right hand sides of the elements of row 6, containing the derivatives of the rotational acceleration with respect to the state variables, are significantly larger with respect to those in Eq. (7.21). This means that their influence on the system eigenmotion is negligible and we can ignore them. In addition, A^*_{51} and A^*_{54} are ≈ 0 due to the fact that in steady-state flight $x_3 \approx -90°$ and $\cos x_3 \approx 0$. In summary, the influence of the controller on the rotational and vertical motions of the vehicle is marginal and it is possible to simplify the elements of the model matrix $\mathbf{A}^*$ to:

$$
\begin{aligned}
&A^*_{11}=0, \quad A^*_{12}=0, \quad A^*_{13}=0, \quad A^*_{14}=1, \quad A^*_{15}=0, \quad A^*_{16}=0;\\
&A^*_{21}=0, \quad A^*_{22}=0, \quad A^*_{23}=0, \quad A^*_{24}=0, \quad A^*_{25}=1, \quad A^*_{26}=0;\\
&A^*_{31}=0, \quad A^*_{32}=0, \quad A^*_{33}=0, \quad A^*_{34}=0, \quad A^*_{35}=0, \quad A^*_{36}=1;\\
&A^*_{41}=\frac{\sin x_3 K_p}{m}, \quad A^*_{42}=0, \quad A^*_{43}=\frac{S_{\text{ref}}\rho x_5^2}{2m},\\
&A^*_{44}=\frac{S_{\text{ref}}\rho x_5\left(C_{D,0}+k_{C_L}\right)}{2m}+\frac{\sin x_3 K_d}{m}, \quad A^*_{45}=0, \quad A^*_{46}=-\frac{S_{\text{ref}}\rho x_5\left(C_{D,0}+k_{C_L}\right)}{2m};\\
&A^*_{51}\approx 0, \quad A^*_{52}=0, \quad A^*_{53}=0, \quad A^*_{54}\approx 0, \quad A^*_{55}=\frac{S_{\text{ref}}\rho x_5}{m}, \quad A^*_{56}=0;\\
&A^*_{61}\approx 0, \quad A^*_{62}=0, \quad A^*_{63}=-\frac{S_{\text{ref}}\rho x_5^2\left(\left(C_{D,0}+k_{C_L}\right)z_{\text{pc}}-k_{C_m}D_0\right)}{2I_{\text{tot}}},\\
&A^*_{64}\approx -\frac{S_{\text{ref}}\rho x_5\left(\left(C_{D,0}+k_{C_L}\right)z_{\text{pc}}-k_{C_m}D_0\right)}{2I_{\text{tot}}}, \quad A^*_{65}=0,\\
&A^*_{66}=\frac{S_{\text{ref}}\rho x_5\left(\left(C_{D,0}+k_{C_L}\right)z_{\text{pc}}-k_{C_m}D_0\right)z_{\text{pc}}}{2I_{\text{tot}}};
\end{aligned}
\tag{7.22}
$$

Before to go on we need to notice that the terms taking into account the control action in row 4:

$$
\frac{\sin(x_3)K_p}{m}=0\left(10^{-3}\right), \quad \frac{\sin(x_3)K_d}{m}=0\left(10^{-2}\right) \tag{7.23}
$$

are also small and have magnitude comparable with those in Eq. (7.21). Nevertheless, the other terms appearing in the right hand sides of row 4 of $\mathbf{A}^*$ are not much larger. This, together with the fact that these terms directly influence the translational eigenmotion, that is the one we want to stabilize by means of the controller, implies that they cannot be neglected.

Figure 7.3 shows on the left hand side the relative error that is committed when determining numerically the eigenvalues using $\mathbf{A}^*$ in the form of Eq. (7.22) instead of Eq. (7.20). The fact that this error is really small proves that the assumptions above are valid. On the right hand side of the figure is instead reported how the eigenvalues associated to the system, calculated numerically using $\mathbf{A}^*$ in the form Eq. (7.22), vary along the steady-state trajectory of the spacecraft. The IC for this trajectory are once more $\gamma_0 = -90°$, $\theta_0 = -90°$, $\dot{\theta}_0 = 0°/\text{s}$, $V_0 = 120\ \frac{\text{m}}{\text{s}}$, $z_0 = 6000$ m, $y_0 = 0$ m. Also in this case the analysis of the eigenvectors has been exploited to understand how the state variables are related to a certain eigenvalue.

In a similar way to what has been done for deriving analytical expressions for the eigenvalues of the open-loop system in Section 7.2.3 we can now determine analytical expressions for the eigenvalues of the closed-loop parachute-payload system. First of all we write down matrix $\mathbf{A}^*$ as:

$$
\mathbf{A}^*=\begin{bmatrix}
0 & 0 & 0 & 1 & 0 & 0\\
0 & 0 & 0 & 0 & 1 & 0\\
0 & 0 & 0 & 0 & 0 & 1\\
A^*_{41} & 0 & A^*_{43} & A^*_{44} & 0 & A^*_{46}\\
0 & 0 & 0 & 0 & A^*_{55} & 0\\
0 & 0 & A^*_{63} & A^*_{64} & 0 & A^*_{66}
\end{bmatrix} \tag{7.24}
$$

By eliminating column and row 2, that are related to variable x_2, i.e., the altitude, that has no influence on the dynamic evolution of the other variables in this simplified model, and by swapping row and column 5 with row and column 6 and row and column 3 with row and column 4, in such a way that the rows and columns related to the rotational motion and to the horizontal motion are grouped, we get:

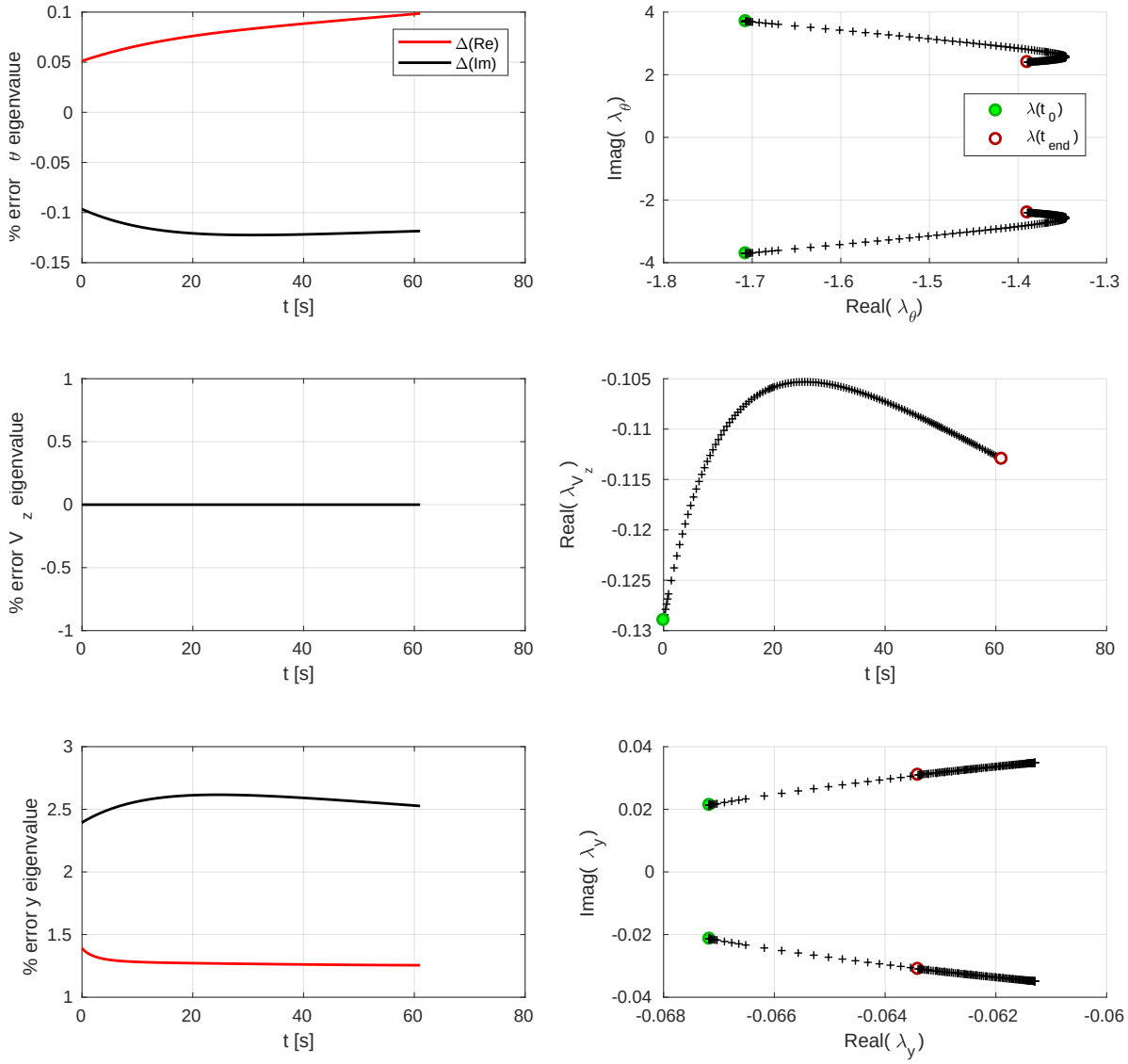

Figure 7.3: Eigenvalue analysis for the steady-state flight of the closed-loop rigid body MPF reference vehicle.

$$\mathbf{A}^*_{(1)} = \begin{bmatrix} 0 & 1 & 0 & 0 & 0 \\ A^*_{41} & A^*_{44} & A^*_{43} & A^*_{46} & 0 \\ 0 & 0 & 0 & 1 & 0 \\ 0 & A^*_{64} & A^*_{63} & A^*_{66} & 0 \\ 0 & 0 & 0 & 0 & A^*_{55} \end{bmatrix} \tag{7.25}$$

From Eq. (7.25) it is already clear that A^*_{55} represents a block on itself. This block, related to the vertical eigenmotion, is equivalent to that of the open-loop system. The eigenvalue related to the vertical velocity then, also in this case, is defined by Eq. (6.36). We now rewrite our matrix as:

$$\mathbf{A}^*_{(2)} = \begin{bmatrix} 0 & 1 & 0 & 0 \\ A^*_{41} & A^*_{44} & A^*_{43} & A^*_{46} \\ 0 & 0 & 0 & 1 \\ 0 & A^*_{64} & A^*_{63} & A^*_{66} \end{bmatrix} \tag{7.26}$$

By means of Schur decomposition, for which once more the interested reader is referred to Press et al. [2007], it has been numerically demonstrated, using the `Matlab` function `bdschur`[1], that matrix $\mathbf{A}^*_{(2)}$ can be diagonalized in two $[2 \times 2]$ size blocks. These are the blocks related to the horizontal and rotational motion modes and we want to determine the respective eigenvalues that characterize them.

It is already interesting to notice how the introduction of the control action has caused a variation in the block structure of the Jacobian matrix associated to the closed-loop system. In particular, differently from the case of the open-loop system, now the horizontal eigenmotion is represented by a $[2 \times 2]$ block whose eigenvalues that, as Figure 7.3 shows, are complex and conjugate with negative real part. This implies a damped oscillatory motion about an equilibrium position.

Consider now the rotational eigenmotion of the controlled system. By comparing the graphs in the right columns of Figure 7.3 and Figure 6.3, one notices that the eigenvalues that are more influenced by the action of the guidance system are those related to the horizontal eigenmotion. The eigenvalues λ_θ for the rotational eigenmotion in the closed-loop case are not significantly different with respect to those defined for the open-loop system. As mentioned earlier, this is due to the fact that the control action has negligible magnitude in the rows of $\mathbf{A}^*$ containing the derivatives of the attitude angle and velocity, θ and $\dot{\theta}$. This suggests that the rotational motion eigenvalues for the closed-loop system can be approximated with the analytical expressions found for the open-loop case, given by Eq. (6.42).

The analytical expression for λ_θ had been determined by demonstrating that columns 1 and 2 of $\mathbf{A}_{(3)}$ could be rearranged to a $[2\times2]$ size block. Since columns 1 and 2 of $\mathbf{A}_{(3)}$, after the simplifications introduced until now, exactly correspond to columns 3 and 4 of $\mathbf{A}^*_{(2)}$ (only the row order is different), this suggests that columns 1 and 2 of of $\mathbf{A}^*_{(2)}$ can be rearranged in such a way to yield the $[2 \times 2]$ block describing the horizontal eigenmotion of the spacecraft. We can use once more the fact that, according to the Gaussian elimination method, a matrix can be block diagonalized by only row operations. This means that, also in this case, the eigenvalues of the $[2 \times 2]$ horizontal eigenmotion block can be determined as a linear combination of the terms appearing in columns 1 and 2 of $\mathbf{A}^*_{(2)}$, i.e., A^*_{41}, A^*_{44} and A^*_{64}.

As for the open-loop analysis, there is not a straightforward way to determine the linear combination coefficients for obtaining exact and simple analytical expressions for the eigenvalues. We thus choose also in this case to approximate them experimentally for the steady-state flight of the MPF reference vehicle.

We start by multiplying row 2 by a scalar $k_{1,c}$ and row 4 by a scalar $k_{2,c}$ and sum the latter to the former. Also, the real part of the eigenvalues of the $[2 \times 2]$ horizontal motion block is exclusively a function of the terms on its diagonal. So, similarly to what has been done in Section 7.2.3, it is possible to express $\mathrm{Re}(\lambda_y)$ as a function of terms $A^*_{44,\mathrm{ss}}$ and $A^*_{64,\mathrm{ss}}$ multiplied by the experimental coefficients $k_{1,c}$ and $k_{2,c}$, and then use the computed $\mathrm{Re}(\lambda_y)$ to express one of the parameters as a function of the other. Considering that the real part of a complex eigenvalue, for a $[2 \times 2]$ matrix, is equal to half the sum of its diagonal terms, then we can write:

$$2\mathrm{Re}\left(\lambda_{y,\mathrm{ss}}\right) = A^*_{44,\mathrm{ss}} k_{1,c} + A^*_{64,\mathrm{ss}} k_{2,c} \quad \rightarrow \quad k_{2,c} = \frac{2\mathrm{Re}\left(\lambda_{y,\mathrm{ss}}\right) - A^*_{44,\mathrm{ss}} k_{1,c}}{A^*_{64,\mathrm{ss}}} \tag{7.27}$$

The imaginary part of the eigenvalues, however, depends on both the diagonal and off-diagonal terms. This means that the optimization of $k_{1,c}$ and $k_{2,c}$ must also take into account the value of the imaginary part

[1] https://nl.mathworks.com/help/control/ref/bdschur.html. Last accessed: 17/01/2018

of the horizontal motion eigenvalues. In addition to this, we choose to introduce a third parameter, $k_{3,c}$, that multiplies row 1 of $\mathbf{A}^*_{(2)}$. The resulting $[2\times 2]$ matrix from which the eigenvalues will be derived is thus:

$$\mathbf{A}^*_{(3)} = \begin{bmatrix} 0 & k_{3,c} \\ A^*_{41}k_{1,c} & A^*_{44}k_1 + A^*_{64}k_{2,c} \end{bmatrix} \tag{7.28}$$

whose conjugate eigenvalues are:

$$\begin{aligned} \mathrm{Re}(\lambda_y) &= \frac{S_{\mathrm{ref}}\rho x_5 \left(C_{D,0}+k_{C_L}\right)k_{1,c}}{4m} - \frac{S_{\mathrm{ref}}\rho x_5 \left(\left(C_{D,0}+k_{C_L}\right)z_{\mathrm{pc}} - D_0 k_{C_m}\right)k_{2,c}}{4I_{\mathrm{tot}}} + \frac{\sin x_3 K_d k_{1,c}}{2m} \\ \mathrm{Im}(\lambda_y) &= \sqrt{\frac{\sin x_3 K_p k_{1,c}k_{3,c}}{m} + \frac{\mathrm{Re}^2(\lambda_y)}{16}} \end{aligned} \tag{7.29}$$

To determine the parameters $k_{1,c}$ and $k_{3,c}$ a 2DOF optimization procedure is needed. In particular, it has been chosen to determine $k_{1,c}$ and $k_{3,c}$ so that the error between the analytical eigenvalues from Eq. (7.29) and the numerically computed ones, in correspondence of the linearisation point of Eq. (6.13), is minimum. For this purpose a graphical method was applied. This resulted in:

$$k_{1,c} = 0.6734, \quad k_{2,c} = 0.0515, \quad k_{3,c} = 1.518 \tag{7.30}$$

A set of experimental coefficients, however, can be optimized for a single point and reference vehicle. With respect to the open-loop case, the error of the horizontal motion analytical eigenvalues with respect to the numerical ones is much more sensitive to variations of the trajectory point in which these are computed and of the parameters of the spacecraft. For very accurate results one should optimise the coefficients specifically per every point in the trajectory and every change in its configuration. Of course, this procedure is really time consuming and would yield no value added to our analysis that, from a qualitative point view, aims at determining how changing a parameter influences the stability behaviour of the spacecraft.

In our case, along the steady-state trajectory for Figure 7.3, the error of the analytical real part is always lower than $\approx 2\%$, while the imaginary part can have an error up to $\approx 20\%$. The larger error are of course experienced in the first part of the trajectory, where the vertical velocity is really different from the value for which it was optimized. However, if the trajectory stays close to the chosen optimisation point, then the errors reduce to a maximum of 1% for the real part and 7% for the imaginary part. In this case, also significant variations of the system parameters, for example the payload mass or the riser length, in the order of 20%, cause an increase of only some % points in these errors. This allows us to say that the translational eigenvalues definition, given by Eq. (7.29), is consistent and can be used for determining the stability properties of the system, in particular in the vicinity of the linearisation point for which the coefficients $k_{1,c}$, $k_{2,c}$ and $k_{3,c}$ have been optimized.

Consider now the real part of the horizontal motion eigenvalue λ_y in Eq. (7.29). This is characterized by three terms. The first two, that express a ratio between the aerodynamic and inertia properties of the system, are analogous to those determining λ_{V_y} in Eq. (6.46) for the open-loop case. In particular the second term, featuring the moment of inertia of the spacecraft at the denominator, expresses the influence of the attitude equilibrium of the system on its translational motion. As before, this term is positive for the considered MPF reference configuration but also much smaller with respect to the others ($k_{2,c} << k_{1,c}$). This means that even if it is destabilising, its contribution to the horizontal eigenmotion of the spacecraft is negligible. The first term, that instead is negative ($x_5 < 0$), suggests that if the aerodynamic forces generated by the parachute are larger, then it will damp faster a perturbation in its horizontal position and velocity state. The term that marks the difference with respect to the open-loop case, however, is the third. It is directly due to the presence of the control action in the dynamics of the system and is the most important contribution to $\mathrm{Re}(\lambda_y)$. In particular, it demonstrates that a larger derivative gain K_d and a smaller spacecraft mass m contribute to making more stable the horizontal eigenmotion of the system.

The imaginary part of λ_y is also really interesting. It includes two terms. One, that is negative, is proportional to the gain K_p, while the other corresponds to $\frac{\mathrm{Re}(\lambda_y)}{4}$ squared. This second term is clearly always positive and, as described earlier, is influenced by the aerodynamic and inertia properties of the system and by the derivative gain K_d. The contribution of the two terms to $\mathrm{Im}(\lambda_y)$ is opposite. In particular, the oscillatory behaviour is present only if the eigenvalues are complex, this requiring that the first term in $\mathrm{Im}(\lambda_y)$ is larger in magnitude than the second. In this situation, according to Eq. (7.29), the oscillatory motion around the equilibrium position will be more relevant in the dynamics of the vehicle if K_p is larger, K_d lower and if the inertia

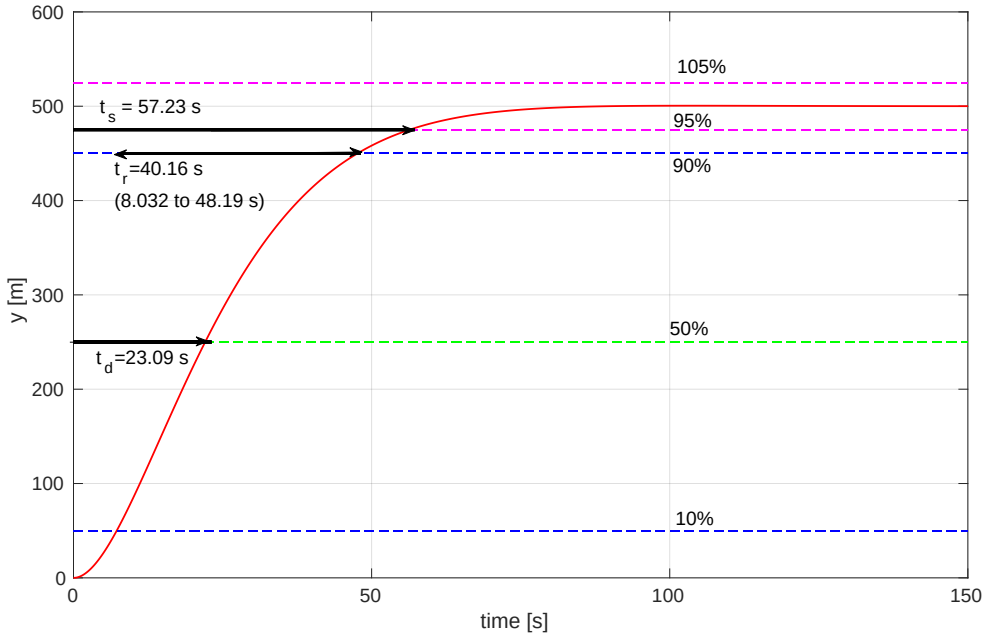

Figure 7.4: Linear Response analysis of the closed-loop rigid body MPF reference vehicle.

Table 7.1: MPF closed-loop descent system horizontal position stability characteristics in the the steady-state point $\mathbf{x}_{ss}$ (from Eq. (6.13)).

Property	Value
ω_y	0.0706 $\frac{\text{rad}}{\text{s}}$
ζ_y	0.906
P_y	209.4 s
t_d	23.15 s
t_r	43.40 s
t_s	57.73 s

of the system dominates over its aerodynamic properties. This is the case for the MPF reference vehicle and mission.

By inserting Eq. (7.29) in Eq. (6.6) it is possible to determine analytical expressions for the the natural frequency ω_y and damping ratio ζ_y of the horizontal eigenmotion of the spacecraft. However, the interpretation of the influence that the various parameters of the spacecraft have on these characteristic values is not straightforward to analyse. This is due to the fact that the analytical expressions describing them, that are not reported here, are more complicated and feature the same dynamic contribution in more places. Nevertheless, it is still possible to state that, in case the λ_y are complex and conjugate, a larger K_p results in a higher ω_y and lower ζ_y.

Table 7.1 reports the properties of the horizontal eigenmotion of the MPF reference spacecraft for the chosen gains. In particular, the delay time t_d, rise time t_r and settling time t_s have been calculated by inserting the damping ratio and natural frequency in Eq. (7.12) to (7.14). The tabled values show a good correspondence with the t_d, t_r and t_s estimated graphically using the response of Figure 7.4. Also, the response shown in Figure 7.4 seems to have no oscillatory behaviour, as instead the complex eigenvalues predict. This can be explained by noting that its period is really large, in the order of 200 s and thus the oscillations around the equilibrium condition, despite being present, are absolutely negligible. This comparison represents a further proof of the validity of the analysis of the present section.

8

MULTIBODY SYSTEM PERFORMANCE

Chapter 3 was dedicated to the development of two models, verified in Chapter 5, for describing the dynamics of a parachute-backshell-payload systems descending through the atmosphere of Mars, whose environment was defined in Chapter 4. The rigid body model was then used in Chapters 6 and 7 for deriving analytical information about the stability behaviour of the system and for tuning the gains of its guidance logic. This model, despite being useful for a preliminary understanding of the dynamics of parachute-payload systems, cannot describe the relative motion of the elements of the spacecraft. On the other hand, the multibody model is less appropriate for linearisation and analytical studies but can reproduce the motion of the descending non-rigid spacecraft with a higher degree of accuracy. The analytical information based on the study of the rigid body model derived until now, will be used as a reference for the analysis of the dynamic stability and horizontal position control system performance of the descent vehicle, modelled as a multibody system. It is remarked that for the multibody model used in the analyses of this chapter the spring constant of the risers is so large that their elasticity is hardly noticeable. In fact, this characteristic is more important for the study of the vibrations affecting the spacecraft and is not really relevant for its attitude that is instead what we are more interested in.

The present chapter is subdivided in two main areas. Section 8.1 will analyse the dynamic response of the system to isolated and continuous inputs, simulating respectively the effect of wind gusts and turbulences that invest horizontally the spacecraft during the descent. In Section 8.2, instead, the use of backshell thrusters for controlling the horizontal position of the spacecraft during the descent will be analysed from the points of view of efficiency and performance it can achieve in correcting an horizontal position error and compensating wind. The chapter is concluded with a discussion about the navigation and control aspects that influence the characteristics of the parachute descent guidance system.

8.1. OPEN-LOOP SYSTEM PERFORMANCE

In this Section the aim is to characterize the dynamic response of the parachute-backshell-payload system. In particular, this will be tested with a single gust in Section 8.1.1 and turbulence in Section 8.1.2. While the first analysis provides valuable information on how an isolated wind disturbance is absorbed and damped, the latter is important for characterizing the frequency response of the spacecraft. Also, by varying some of the parameters of the spacecraft, the analysis will determine the influence that these have on its stability properties.

8.1.1. RESPONSE TO WIND GUSTS

During the parachute descent in the planetary boundary layer of Mars the spacecraft can encounter a wind gust. According to the description given in Section 4.1, the gust resembles a net discontinuity in the constant wind speed profile. Considering a parachute-backshell-payload system flying vertically, a vertical gust causes an increase in the drag forces generated by its body elements as a result of a larger dynamic pressure. These force contributions, however, are parallel to the rotational symmetry axis of the spacecraft along which relative movement is constrained. If on one hand these gusts can cause significant variation in vertical velocity and, in turn, shifts in the mission schedule, on the other hand they do not represent a critical issue from the attitude dynamics point of view. Because of this, the system response to a vertical gust will not be analysed in detail.

Table 8.1: Set of IC for the MPF reference vehicle used for gust response open-loop system simulations.

Parameter	Value	Parameter	Value	Parameter	Value
γ_{10} [deg]	-90	γ_{20} [deg]	-90	γ_{30} [deg]	-90
θ_{10} [deg]	-90	θ_{20} [deg]	-90	θ_{30} [deg]	-90
$\dot{\theta}_{10}$ [deg/s]	0	$\dot{\theta}_{20}$ [deg/s]	0	$\dot{\theta}_{30}$ [deg/s]	0
V_{10} [m/s]	100	V_{20} [m/s]	100	V_{30} [m/s]	100
z_{10} [m]	6000	z_{20} [m]	5978.83	z_{30} [m]	5970.83
y_{10} [m]	0	y_{20} [m]	0	y_{30} [m]	0

Table 8.2: Sample gust characteristics.

Parameter	Value
h_i [m]	4000
h_e [m]	3900
Δh_t [m]	10
V_{gu} [m/s]	20

The situation is completely different in case of a horizontal gust. This is indeed very dangerous for the attitude stability of the parachute-payload vehicle. Assuming a null background wind speed, as the gust impacts the system, the angles of attack of the parachute, backshell and payload vary and the aerodynamic forces grow in horizontal direction. In particular, if the spacecraft is flying in steady-state flight in absence of wind before the gust, then the new angle of attack and in turn the magnitude of the aerodynamic forces that the gust generates depend on the difference between the velocity of the spacecraft and that of the gust. At this point the elements of the spacecraft experience different accelerations that cause them to oscillate one with respect to the other. Also, the newly generated aerodynamic forces cause the horizontal velocity of the whole system, depending on its aerodynamic and inertia properties and on the characteristics of the gust, to increase asymptotically and tend to the maximum gust speed. In this new equilibrium condition the angles of attack, and in turn the horizontal component of the aerodynamic forces, would be once more null. However, a gust is normally so short that the horizontal velocity variation is not really significant so that the wind speed discontinuity at the end of the gust and the consequent horizontal aerodynamic force variation it generates are negligible. After this point the spacecraft tends back to its original steady-state flight condition in absence of wind.

The attitude behaviour of the MPF reference spacecraft is depicted in Figure 8.1 that shows how its body elements are excited at the beginning of the gust and oscillate in different ways before to be damped once the gust has ended. The oscillation amplitude of the system elements is determined by the intensity of the gust and for the considered vehicle it can reach 45° for the payload in case of a 20 m/s gust. Also, it is interesting to notice how the oscillation of the backshell is clearly the result of the superimposition of two sinusoids with different frequencies. This characteristic is due to its direct interaction with both the parachute and the payload that, through the connection forces, impose to the backshell the respective oscillatory behaviour. The same behaviour is valid also for the other two boldy elements but less noticeable. Figure 8.2 displays instead the step in the descent trajectory of the MPF reference vehicle caused by the presence of gusts of different duration. In general, a gust with a duration of a few seconds can cause a displacement in the order of 100 m.

In the following, the study of the response of the MPF reference vehicle to sample gusts will be used to underline the general characteristics of its attitude dynamics behaviour. It is remarked that not only the attitude of the vehicle oscillates, but also the positions of the COM of the elements of the spacecraft. However, these two aspects are strictly correlated thanks to the connections that bond the bodies. In other words the analyses of the two would lead to the same general considerations about the dynamic stability of the system. We choose to focus the attention on investigating the spacecraft attitude dynamics because, differently from the position components of the COM, the attitude angles of the system elements have a constant equilibrium position even in case of external perturbations such as winds, and because this allows us to compare the results derived here with those from previous sections, that also focus mainly on the attitude of the system.

The response of the parachute-payload system to a horizontal gust depends on its attitude when the gust is met. In fact, with respect to the factors influences the aerodynamic forces generated by the parachute, the gust speed causes variations in the angle of attack and in the dynamic pressure. Consider that the system is flying in steady-state conditions. If the gust invests the parachute perpendicularly to its rotational symmetry axis the side force increase caused by the variation of the angle of attack is the dominant effect. If instead the parachute

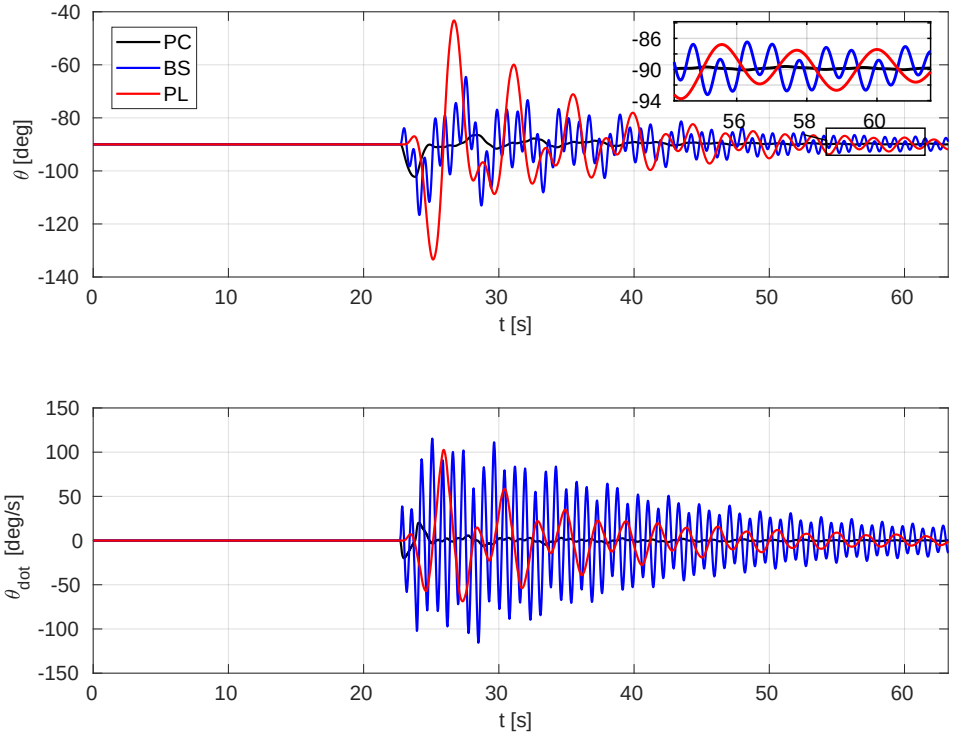

Figure 8.1: Effect of a sample wind gust (Table 8.2) on the attitude behaviour of the MPF reference vehicle (IC from Table 8.1).

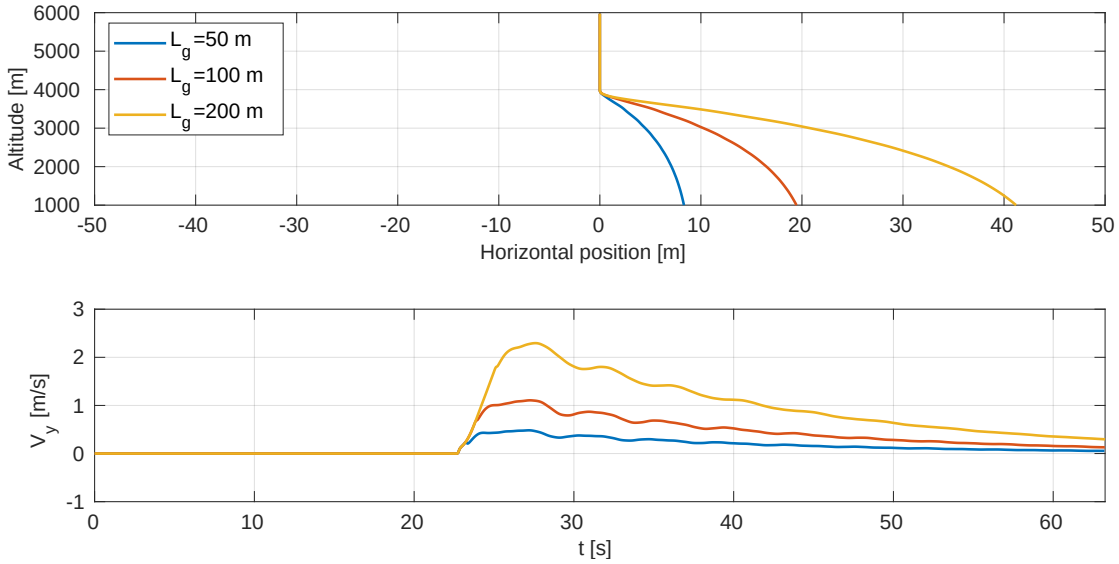

Figure 8.2: Effect of wind gusts (Table 8.2) of different size L_g on the trajectory of the MPF reference vehicle (IC from Table 8.1).

is partially oriented in the direction of the gust speed, then the increase of drag force in horizontal direction due to a larger dynamic pressure will be the dominant effect. The drag increase in horizontal direction is much larger than the side force that is generated by the variation of the angle of attack and can thus generate much more dangerous attitude oscillations of the whole system.

The spacecraft horizontal and vertical velocities of the spacecraft in the moment when the gust is met also have a significant influence on the oscillatory motion that this disturbance causes. As already suggested, the intensity of the gust that the spacecraft senses depends on the difference between the horizontal velocity of the vehicle and that of the gust. If instead the vertical velocity is larger, then the variation of the angle of attack

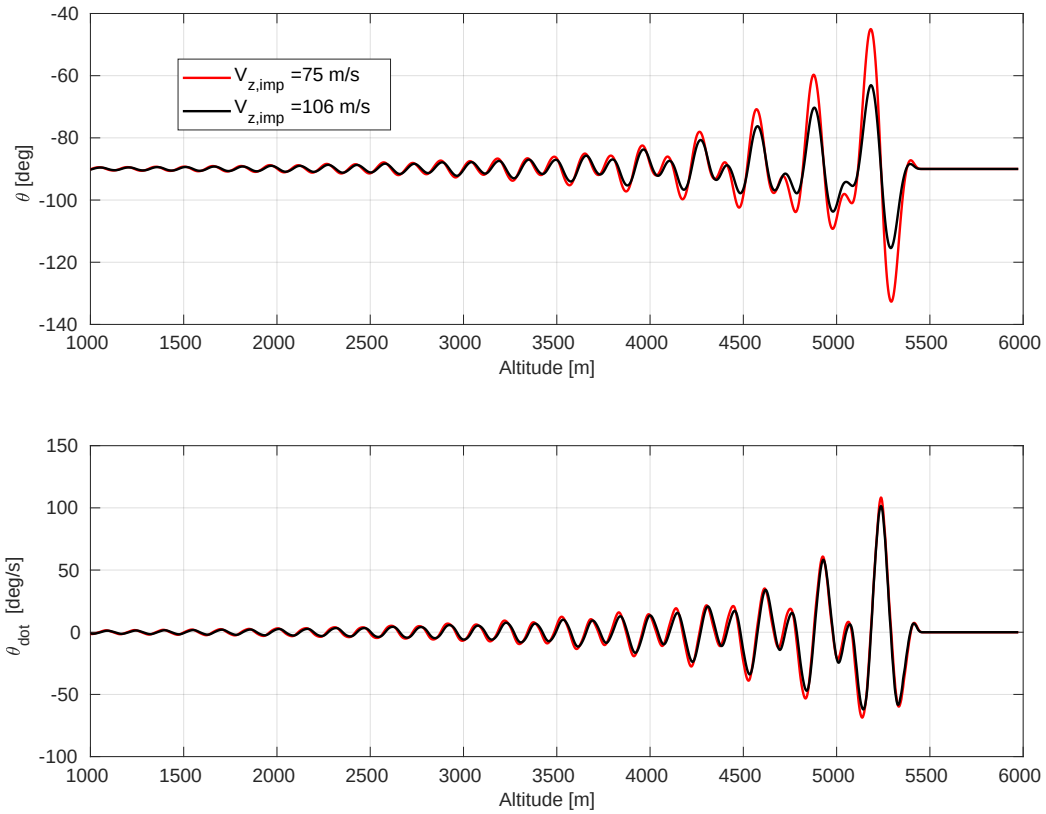

Figure 8.3: Effect of gust on the attitude oscillations of the payload for different vertical velocities.

due to the same gust is lower because the horizontal airspeed component due to the gust is more negligible with respect to the vertical one. As a result, the horizontal aerodynamic forces that the gust generates will have a lower magnitude. In other words, the system is stiffer and will withstand better the impact of the gust. Considering these, a gust at lower altitude, where the vertical velocity of the spacecraft is lower as well, is more critical and, additionally, the system has less time for damping the resulting oscillatory motion before than the terminal descent thruster ignition target altitude is reached.

This analysis is proved by Figure 8.3 that shows the effect of the spacecraft vertical velocity on the influence that the same gust ($h_i = 5500$ m, $h_e = 5400$ m, $\Delta h_t = 10$ m, $V_{gu} = 20$ m/s) has on its oscillatory behaviour. For clarity reasons the image shows only the attitude oscillations of the payload, where this effect is better visible. The IC for the descent flight simulation of the MPF reference vehicle are those listed in Table 8.1 for the red plot, while for the black plot an initial velocity of 200 m/s has been assumed for all the three elements. The simulation has assumed constant atmosphere density equal to 0.0138 kg/m^3 that corresponds to an altitude of 1000 m.

The most important factors determining the dynamic response to a gust are those related to the aerodynamic and inertia properties of the vehicle. One of these is the reference surface of the parachute that influences different aspects of the descent flight. In fact, if on one hand it is desirable that the equilibrium velocity, proportional to the inverse of the parachute reference surface, is as low as possible, this meaning that the aerodecelerator can dissipate more energy before to reach the target, on the other hand a larger parachute weights more and causes the wind drift error contribution to increase due to the fact that the descent phase is longer. Also, a larger deceleration implies that the vertical velocity is lower and, as earlier demonstrated, this represents a disadvantage from the point of view of attitude dynamic stability when the gust is met. However, the driving requirement for deciding the parachute size remains the equilibrium velocity that has to be achieved before terminal descent thrusters ignition and, in turn, the payload mass whose weight has to be balanced.

Other parameters that have a significant influence on the attitude behaviour of the system include the type of parachute (namely its aerodynamic properties), whose choice is heavily influenced by the mission heritage, and, above all, the spacecraft configuration, i.e., the distances between its three elements. Indeed, once the

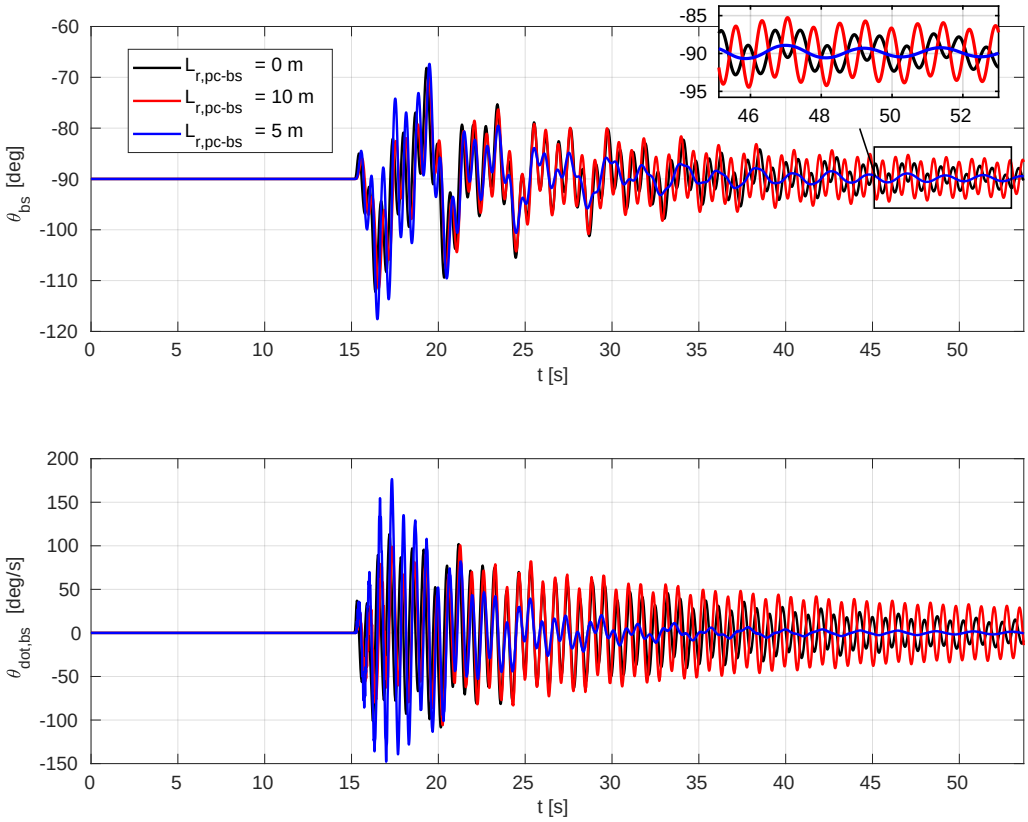

Figure 8.4: Effect of a sample wind gust (Table 8.2) on the reference vehicle MPF backshell attitude behaviour for different parachute-backshell riser lengths.

spacecraft baseline has been defined, its configuration can be adjusted by varying the lengths of the risers connecting the parachute with the backshell and the backshell with the payload, so that to achieve the desired dynamic response.

By running several gust response simulations with different lengths of both risers, it has been verified that these parameters have a marginal effect on the oscillatory behaviour of the parachute body. This was expected because its attitude is dominated by the aerodynamic forces that grow as soon as its angle of attack moves with respect to the 0 equilibrium condition. In addition to this, while the length of the riser between the parachute and the backshell $L_{\text{r,pc-bs}}$ has a major influence on the backshell attitude behaviour, it influences only marginally the characteristics of the payload oscillations. The opposite happens for the riser between the backshell and the payload $L_{\text{r,bs-pl}}$. Considering these, we can analyse the attitude behaviour of the backshell and payload as exclusive functions of, respectively, $L_{\text{r,pc-bs}}$ and $L_{\text{r,bs-pl}}$.

Figure 8.4 shows the oscillatory response of the backshell when the spacecraft is hit by a sample 20 m/s horizontal gust, for different values of $L_{\text{r,pc-bs}}$. The IC are those listed in Table 8.1 with the exception of the $z_{0,2}$ and $z_{0,3}$ initial position components. These depend indeed on the riser lengths that are varied in the figure, but can easily be determined by considering that the simulation starts with the vehicle oriented vertically and that the risers are not lengthened at t_0. The same holds also for the IC of Figure 8.5. From this figure it is really interesting to notice that, while the response for the cases of $L_{\text{r,pc-bs}} = 0$ m and $L_{\text{r,pc-bs}} = 10$ m is pretty much similar, in case of the intermediate value $L_{\text{r,pc-bs}} = 5$ m the oscillations are damped much more efficiently and, still, the maximum backshell attitude angle variation does not go beyond 30°.

The influence of the backshell-payload riser length $L_{\text{r,bs-pl}}$ on the oscillations of the payload body, that represents most of the mass of the MPF spacecraft, can easily be explained. Figure 8.5 confirms that, as expected, a shorter riser, that results in a lower moment of inertia for the lower section of the spacecraft (lower riser attached to the payload), causes the payload attitude angle oscillation amplitude to be larger at the impact of the gust, up to 40°, but also that these oscillations are damped faster in the remainder of the descent.

The stability of the backshell is fundamental if the thrusters to be used for horizontal position control purposes during the descent are fixed with respect to it. In fact, these should always push as parallel to the ground

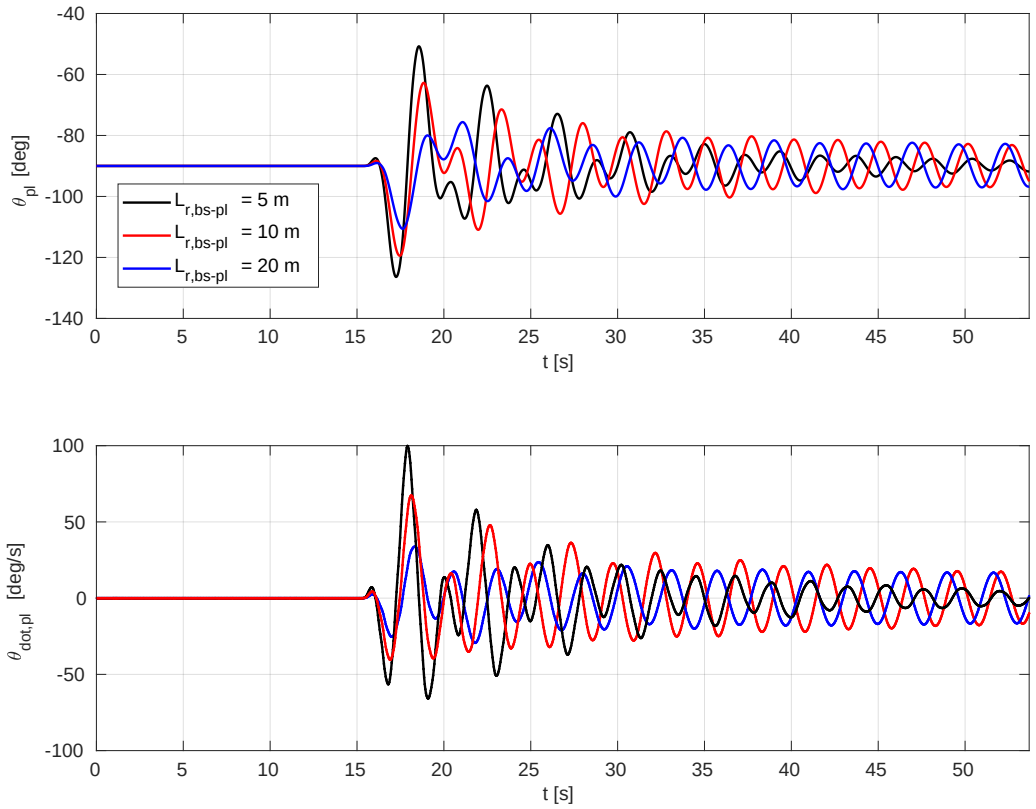

Figure 8.5: Effect of a sample wind gust (Table 8.2) on the reference vehicle MPF payload attitude behaviour for different backshell-payload riser lengths.

as possible. If the thrust direction oscillates, then the system loses efficiency. The condition $L_{\text{r,pc-bs}} = 5$ m, even if it causes the impact of the gust to be a little bit more critical for the backshell, represents an optimum for the purpose of our guided system and will be used for studying the performance of the closed-loop system in Section 8.2. With respect to the backshell-payload riser length, instead, a shorter riser, as already suggested in Chapter 2, results in a system that is more sensitive to external perturbations but damps the oscillations faster and is more responsive. The latter are desirable characteristics for the purpose of controlling the trajectory and thus this parameter will be kept equal to 5 m.

When choosing the riser lengths, however, also impingement of the thrusters plumes with the parachute or payload has to be taken into account. For the original MPF spacecraft, equipped with backshell thrusters pushing downwards, the payload was at least at a distance of 20 m. In our case the thrusters push horizontally and we can accept a payload that is closer to the backshell, at more than 5 m. Also, since the spacecraft flies vertically, the plumes of the engines will extend upwards from the backshell to the parachute and this could represent a danger. However, the suspension lines, together with the parachute backshell riser, keep the canopy at a distance of around 25 m that is assumed to be adequate to avoid impingement, even if more accurate studies about this topic are suggested.

Finally, it is interesting to notice that the oscillatory motion of the payload body, shown in Figure 8.5 for the original MPF reference case with and $L_{\text{r,bs-pl}} = 5$ m, has a period between 2 and 2.4 s. This is comparable to the period for the attitude oscillatory motion of the parachute-payload rigid body system whose attitude behaviour properties, derived analytically for the case of steady-state flight in Section 6.2, are reported in Table 6.1. In addition to this, the payload attitude oscillations are clearly under-damped, as also predicted for the rigid body by the damping ratio value. This parallelism can be explained by considering that the payload represents the major contribution to the moment of inertia of the spacecraft and that for small angles of attack, this representing one of the assumption for the linearisation of the system in steady state conditions, the attitude motion of the system is dominated by its inertia properties over the aerodynamic forces generated by the parachute.

Table 8.3: Set of IC for the MPF new reference vehicle used for turbulence response and closed-loop system simulations.

Parameter	Value	Parameter	Value	Parameter	Value
γ_{10} [deg]	-90	γ_{20} [deg]	-90	γ_{30} [deg]	-90
θ_{10} [deg]	-90	θ_{20} [deg]	-90	θ_{30} [deg]	-90
$\dot{\theta}_{10}$ [deg/s]	0	$\dot{\theta}_{20}$ [deg/s]	0	$\dot{\theta}_{30}$ [deg/s]	0
V_{10} [m/s]	100	V_{20} [m/s]	100	V_{30} [m/s]	100
z_{10} [m]	6000	z_{20} [m]	5973.83	z_{30} [m]	5965.83
y_{10} [m]	0	y_{20} [m]	0	y_{30} [m]	0

Table 8.4: Mars planetary boundary layer sample turbulence characteristics.

Parameter	Value
h_i [m]	4000
h_e [m]	3000
σ [m/s]	2.4
$\omega_{t,\max}$ [Hz]	40.82

8.1.2. RESPONSE TO TURBULENCE

The analysis of Section 8.1.1, based on the response to an isolated sample gust, has served for determining some general characteristics of the attitude dynamics of a parachute-backshell-payload non-rigid spacecraft. Some of the conclusions derived there, such as the fact that longer risers result in a system that can withstand more effectively the impact of external perturbations, could have been derived also by analysing the attitude response to a turbulence investing it. However, studying the response to a single gust was considered to be the most straightforward approach. In this section the aim is to analyse the frequency response of the spacecraft. This is in fact particularly important for a non-rigid system. For this purpose we will evaluate how the attitude of the system reacts to the continuous excitement due to the atmospheric turbulence in the planetary boundary layer of Mars that, as explained in Section 4.1.3, has been modelled as a sinusoidal signal.

Figure 8.6 shows the oscillatory behaviour of the attitude angles θ due to sinusoidal wind velocity profiles with different frequencies. The blue dot in the plot for θ_{bs} indicates when the turbulence begins while the red dot indicates when it ends. The first thing to notice here is that the minimum frequency for the atmospheric turbulence on Mars ω_t =40.82 Hz is not an issue for the dynamics of the system that, in this case, does not significantly senses the disturbance. As the frequency decreases the effects of turbulence, especially on the parachute and backshell elements, become significant. At 10 Hz these two bodies experience a resonance effect. The similarity of their attitude motion is due to the fact that they have comparable moment of inertia. However, the oscillation amplitude for the parachute is much smaller because of the dominant contribution of the horizontal aerodynamic forces when its angle of attack increases. At these frequencies the motion of the payload is not yet significantly influenced because of the fact that it has a much larger moment of inertia. When increasing the turbulence signal period even more, also the natural oscillation frequency of the payload body is matched at around 1-5 Hz. At this point, however, the turbulence is already not an issue for the parachute and backshell elements. After 1 Hz the influence of turbulence on the attitude behaviour of the system becomes progressively less important. At 0.1 Hz its effect on the spacecraft dynamics is comparable to that of a long lasting shallow gust and causes mainly oscillations in its horizontal velocity and, in turn, in the descent trajectory.

These results have been derived for the MPF configuration with $L_{\text{r,bs-pl}} = L_{\text{r,pc-bs}} = 5$ m. By changing the riser lengths the frequencies at which the attitude angles oscillation amplitudes are maximum vary as well but these maximum amplitudes will not change significantly. In fact, the latter are directly proportional to the amplitude of the excitation signal and do not really depend on its configuration. Figure 8.6 shows that the atmospheric turbulence on Mars represents a minor issue for the attitude motion if compared with the effect of gusts. In particular, the 2.4 m/s horizontal velocity profile standard deviation due to atmospheric turbulence causes at most oscillations with an amplitude of 15° for the backshell, while a gust of 20 m/s, that according to the available wind data for Mars is an average value, can result in angular variations of up to 30°. This suggests that dimensioning the spacecraft configuration according to the gust attitude response, as done in the previous section, is an appropriate choice.

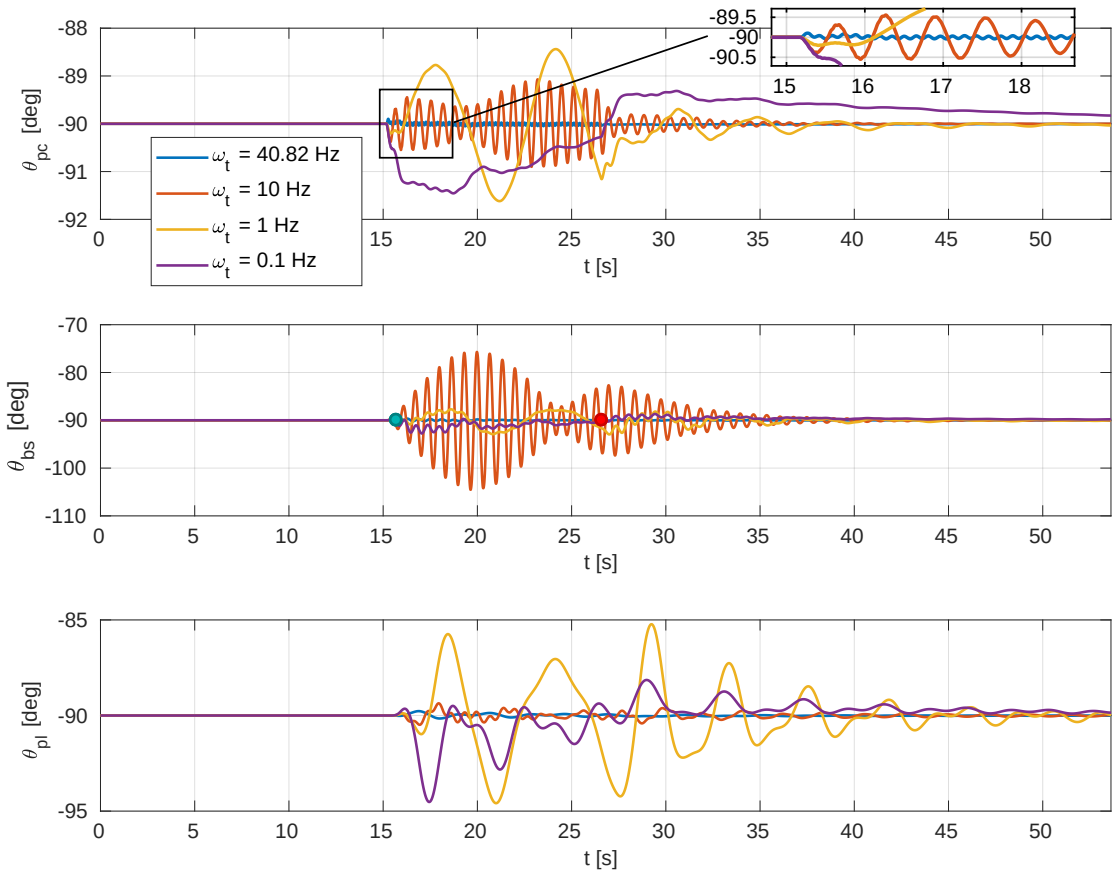

Figure 8.6: Effect of different turbulence (Table 8.4) frequencies on the attitude oscillations of the new MPF reference vehicle (IC from Table 8.3).

8.2. CLOSED-LOOP SYSTEM PERFORMANCE

As already mentioned multiple times, the purpose of the present study is to evaluate the possibility to implement a guidance system based on the backshell thrusters that can control the horizontal position of a spacecraft during the parachute descent on Mars. In this section we will characterize the performance that this system, equippend on the MPF reference vehicle, can achieve in correcting a trajectory error and compensating a horizontal wind. Also, we will evaluate how backshell thrust affects, amongst others, the attitude behaviour and the mass of the spacecraft. In addition, the effect of atmospheric perturbations on the closed-loop system will also be evaluated. A discussion about the influence of the navigation and control aspects on the performance of the guidance system concludes the chapter.

8.2.1. PERFORMANCE IN NOMINAL CONDITIONS

In the previous chapters the characteristics of the spacecraft and of the guidance system for controlling its trajectory during the parachute descent have been defined. The only parameter for which a reference value has not been set yet is the maximum thrust T_{max} of the hydrazine-based reference backshell thrusters.

A larger T_{max} implies a larger maximum error that can be corrected and a better system responsiveness. On the other hand, however, the mass and volume of a hydrazine thruster is somehow proportional to the T_{max} it can generate. In addition to this, a thrust push, similarly to a short wind gust, causes the attitude of the system to oscillate with an amplitude proportional to the intensity of the push, that in the worst case is T_{max}. By running a number of tests with different sample errors between 100 and 500 m, that represent the order of magnitude of the wind drift error, it has been verified that the system responsiveness does not increase significantly with values of T_{max} larger than 500 N. A sudden push at T_{max} = 500 N, also, causes θ angles oscillations, estimated for a vehicle vertical speed of 100 m/s, with a maximum amplitude of 35° (this worst case is for the payload whose oscillations have a larger amplitude than for the other elements), that is

comparable to that due to an average Mars gust, analysed in Section 8.1. Finally, a 500 N hydrazine thruster weights about 2 kg and is 45 cm long[1]. These dimensions are considered to be acceptable for housing the thrusters in the backshell of the MPF spacecraft.

Now the reference configuration for the spacecraft is complete and we can use the available information to determine the performance that the parachute descent control system can achieve. Figure 8.7 shows how the system responds to initial errors of different magnitude. In general, the system always gets close to the $y = 0$, $V_y = 0$ equilibrium condition, but, already for an initial error of 900 m, the accuracy at target altitude is low. At this point indeed the spacecraft is still 60 m far from its target and features a horizontal velocity slightly larger than 5 m/s. In this situation the system is clearly at its limit, this being confirmed by the fact that for half of the descent the thrusters are saturated. The situation improves if the error to correct is 700 or 500 m. However, even for a small initial error of 100 m, whose correction never requires the system to push at $T_{\max}$, a small residual error, in the order of 1 m and 0.1 m/s for respectively the horizontal position and velocity, is present when the target altitude is reached. This is caused by the fact that when the position error is small, i.e., when the system is close to the target, then the proportional and derivative contributions determining the control signal have comparable magnitude and opposite sign, so that the commanded thrust is about null and the spacecraft tends to fly almost vertically even if it has not reached the target. This behaviour can be changed by increasing the controller gain K_p or reducing K_d. This would result in a higher responsiveness at the cost of having a system that consumes more propellant and that oscillates around the equilibrium position, the latter causing, in turn, also undesirable attitude oscillations of the non-rigid spacecraft. Finally, a larger initial position error causes the trajectory to be more curved and longer and, as a result, the total descent time will be larger as well.

From Figure 8.7 it was possible to estimate the delay times t_d for the various descent trajectories (indicated by the coloured dots). It is interesting to notice that the delay times for $\Delta_{y,0} = 100, 300, 500$ m are comparable to the delay time $t_d = 23.15$ s estimated analytically for the parachute-payload rigid body model flying in steady-state conditions. As $\Delta_{y,0}$ increases, however, the descent segment during which the thrusters are saturated enlarges accordingly and, as a result, the delay time increases. In this case in fact the actual thrust that the system generates, i.e., $T_{\max}$, is lower than the thrust proportional to the state error that the PD controller computes. In general, all the differences with respect to the linear system response depicted in Figure 7.4 are imputable to the non-linearities of the multibody model and to differences in the configuration of the spacecraft.

Each of the trajectories depicted in Figure 8.7 is characterized by a certain fuel consumption. Clearly, the maximum consumption of 7.1 kg of fuel is for $\Delta_{y,0} = 900$ m, while instead for correcting $\Delta_{y,0} = 100$ m the system needs 0.9 kg of hydrazine. Considering this, a tank containing 8 kg of fuel is assumed to be appropriate and redundant for ensuring control authority enough to handle different mission scenarios. If we assume that the backshell is equipped with 6 thrusters, then the whole guidance and control system for parachute descent, assuming that the computing hardware is the same already installed for guiding the entry and terminal descent phases, would have a mass of about 20 kg[2]. This mass has not been taken into account in the calculations. However, this does not represent a problem because the MPF payload mass is much larger and 20 kg more would not dramatically affect the total descent time or trajectory. Conversely, if the the thrusters and tank are installed in the backshell, then it would cause a non negligible increase in its mass and moment of inertia, thus making its attitude less sensitive to external perturbations or thrust pushes. In summary, not considering the mass contribution of the the parachute descent guidance and control unit does not result in significant inaccuracies and is a conservative approach with respect to attitude dynamics.

A final remark has to be made with respect to the guidance command update frequency. This parameter, if too small, causes an increase of the overall consumption and a less smooth trajectory. However, for values larger than 1 Hz, the system performance characteristics do not significantly improve while instead the computational time for the simulation increases dramatically. Assuming a guidance command update frequency of 1 Hz for the simulations in Figure 8.7 represents a good compromise between computational time and accuracy.

[1] These data are derived from the data sheets available from http://www.rocket.com/propulsion-systems/monopropellant-rockets. Last accessed: 05/02/2018.

[2] This value gives the order of magnitude of the mass of the whole parachute descent guidance and control unit for the parachute descent. However, depending on the hardware and amount of control authority that the mission requires this estimation can significantly vary.

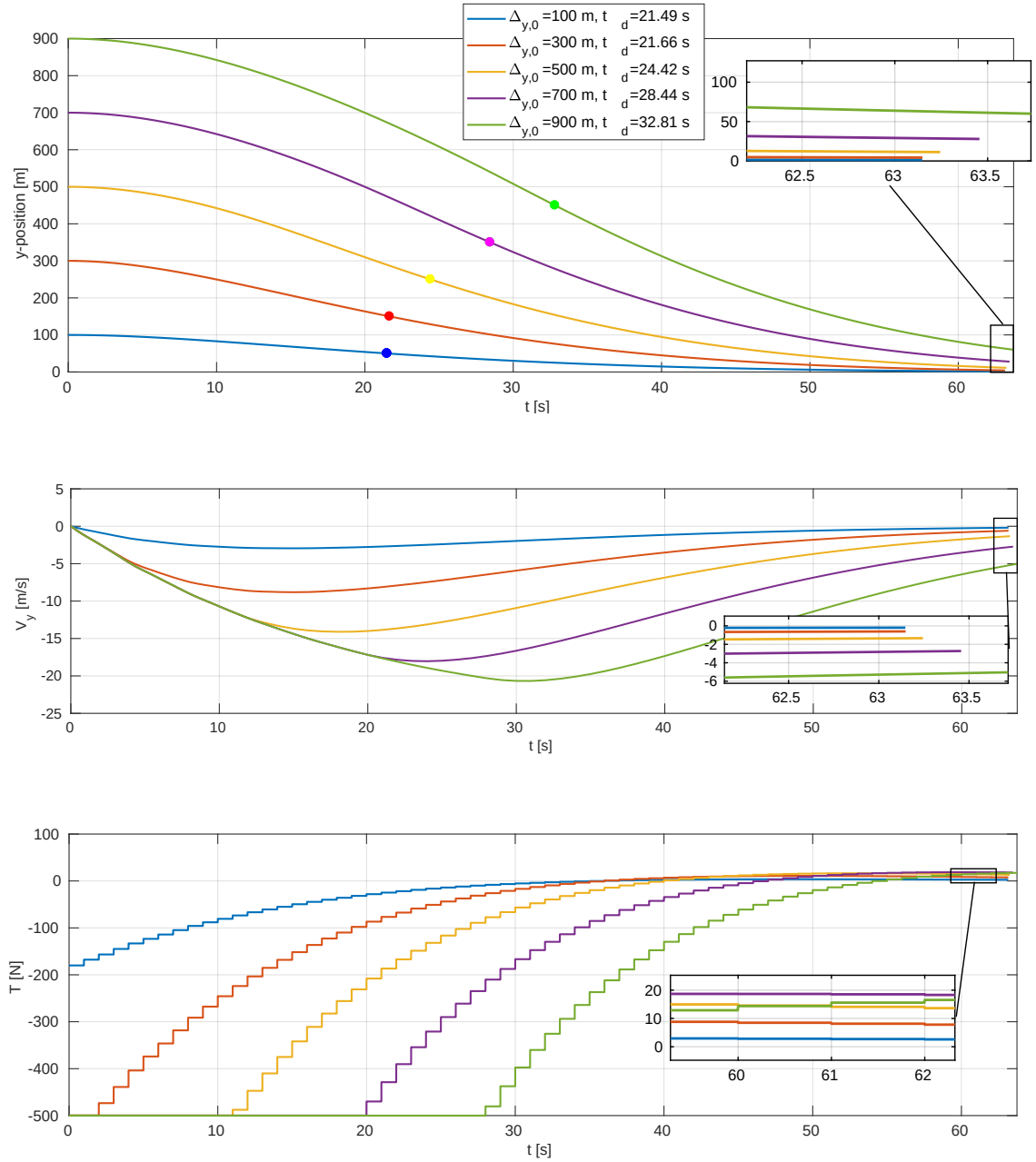

Figure 8.7: Response of the closed-loop system to different initial horizontal position errors (IC from Table 8.3 except that for y position components that vary with the initial error).

8.2.2. PERFORMANCE IN PERTURBED CONDITIONS

In Section 8.2.1 the nominal performance of the system in absence of external disturbances has been evaluated and discussed. The purpose of this section is instead to understand how the MPF reference spacecraft, for which the configuration and GNC system characteristics have been updated in the previous paragraphs according to the results that were progressively derived, behaves in presence of constant wind and how the performance of the parachute descent GNC system varies in case the spacecraft is subjected to turbulence during the flight.

While descending through the atmosphere of Mars the spacecraft can encounter constant winds. A horizontal constant wind speed causes the equilibrium condition of the parachute-backshell-payload system to vary. In particular, after a transient phase in which the system behaves analogously to the case of the gust due to the airspeed discontinuity, the horizontal velocity stabilizes and becomes equal to the horizontal wind speed. The angles of attack and attitude angles of the elements of the spacecraft are 0 also in this case but the descent is not vertical any more. Depending on the characteristics of the spacecraft, the duration of the transient phase can vary but the final equilibrium condition depends exclusively on the wind situation.

The thrust force generated by the backshell thrusters can be exploited to compensate the effect of wind up to a certain wind speed. Figure 8.8 shows how the guided trajectory of the system responds to constant winds of variable intensity. The system is also given an initial horizontal position error of 500 m so that at an altitude of 6000 m, where the wind is supposed to begin, it is already pushing at $T_{\max}$. It is easy to notice that the thrust generated by the backshell engines can easily handle a horizontal wind with a speed up to 15 m/s. In fact, in these cases the system would be able to reach the target by simply pushing at $T_{\max}$ for a longer period. To obtain this behaviour, however, a more sophisticated control law taking into account the effective airspeed of the vehicle is needed. As the wind speed increases, the horizontal component of the aerodynamic force generated by the parachute increases as well until at $V_w = 26$ m/s it almost balances with the thrust force. As Figure 8.9 shows, in this situation the parachute bends in the direction of the wind, opposite to the direction of the thrust, so that, assuming a wind with positive speed in the inertial frame I, its attitude angle increases. The equilibrium is reached when the horizontal component of the parachute drag equals the backshell thrust. This happens when $\theta_{\text{pc}} \approx -110°$. For wind speeds larger than 26 m/s the horizontal component of the parachute drag becomes dominant over the backshell thrust and the system cannot any more compensate for it even pushing constantly at $T_{\max}$. By increasing $T_{\max}$, the maximum wind speed that can be compensated increases accordingly but then, for reaching the equilibrium condition, the parachute has to bend even more with respect to the backshell and this represents an issue for impingement reasons. The fact that the θ_{bs} does not stabilize exactly on -90° is due to the fact that the attitude of this element is influenced by both the forces generated by the parachute and payload that are transmitted through the risers. In the situation depicted in Figure 8.9 the backshell is tilted in the same direction of the parachute because the drag it generates is dominant over the payload weight.

The performance of the backshell thrust guidance system has been evaluated also in case the spacecraft is subjected to turbulence for the whole descent flight. In particular, the response has been tested using a turbulence frequency of 10 Hz, that, as demonstrated earlier, is the most critical frequency for the attitude behaviour of the backshell and parachute, and 1 Hz, that is instead dangerous for the attitude oscillations of the payload body. The results of this analysis, however, have shown that the spacecraft trajectory, as well as the overall guidance system consumption, are not significantly influenced by the presence of this perturbation.

8.2.3. GNC-SYSTEM CONSTRAINTS

The state of the art for Mars EDL missions, as said, is represented by MSL. Indeed, Curiosity rover was landed with an accuracy of about 10 km. This result, however, is still far from the 100 m accuracy that NASA has set as long term objective for enabling manned missions to the Red Planet. The major contribution to these residual 10 km is the navigation error that the spacecraft accumulates during the cruise, entry, and descent phases. In other words, navigation error on Mars represents still the biggest step to climb for achieving pinpoint landing accuracy.

When the parachute phase starts, at an altitude between 10000 m and 8000 m over the surface of Mars, the deployment position inaccuracy is in the order of 3 km (3σ) and is almost totally due to navigation error. This inaccuracy then increases due to additional navigation error, wind drift and other effects in the remainder of the flight. The parachute descent horizontal control concept has the objective to ensure the system a certain control authority budget to compensate for the disturbances that affect this flight phase and to correct some of the inaccuracy already present at deployment. In the real case, however, its performance is affected by the characteristics of the navigation and control subsystems. These two topics, despite can be treated indepen-

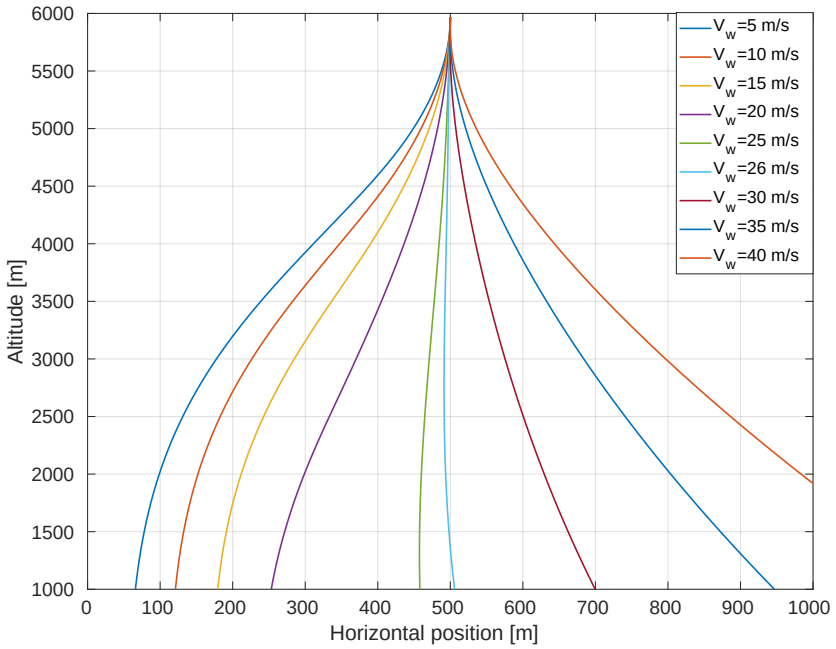

Figure 8.8: Effect of horizontal wind on the guided parachute descent trajectory (IC: from Table 8.3 except $y_{1,0} = y_{2,0} = y_{3,0} = 500$ m).

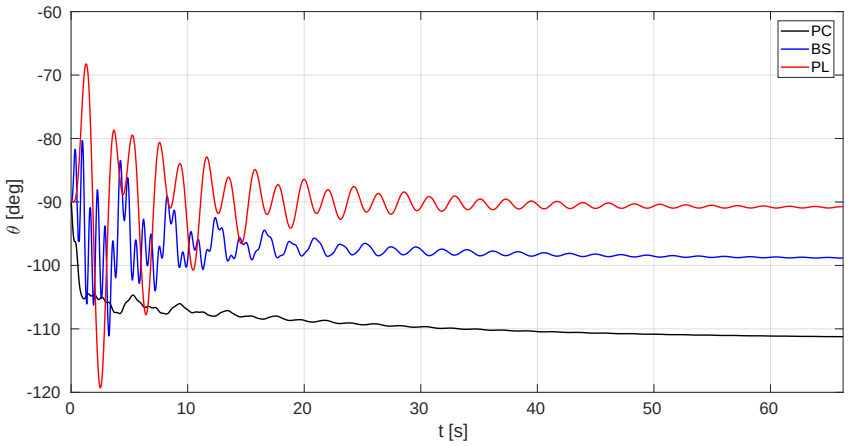

Figure 8.9: Effect of 26 m/s horizontal wind on the attitude behaviour of MPF reference guided vehicle (IC from Table 8.3 except $y_{1,0} = y_{2,0} = y_{3,0} = 500$ m).

dently with respect to the argument of the present study, are closely related to it and thus need to be discussed. The navigation error is not an error contribution just like the others that can be compensated if the vehicle has enough control authority. In fact, it causes the error signal that the guidance logic takes in input to be wrong, so that the resulting command, that is tuned for correcting the error signal, will not be appropriate for correcting the real error.

What normally happens during a generic EDL mission is that at lower altitudes and lower speeds, progressively more accurate navigation units can be used. For example, during entry the main navigation unit is the IMU. When the altitude decreases the radar can be activated and the altitude estimation improves. Finally, during the descent phase, when the spacecraft is closer to the surface it is possible to use an optical navigation system that ensures the highest level of accuracy for Mars navigation.

In recent years the performance of optical navigation systems based on Mars craters mapping and recognition has grown significantly so that they seem to represent a step forward in the direction of pinpoint landing accuracy. The position estimation uncertainty of these systems, that have only been designed for being used up to altitudes of 3000 m, depends on the accuracy they can achieve at locating a feature on the surface with

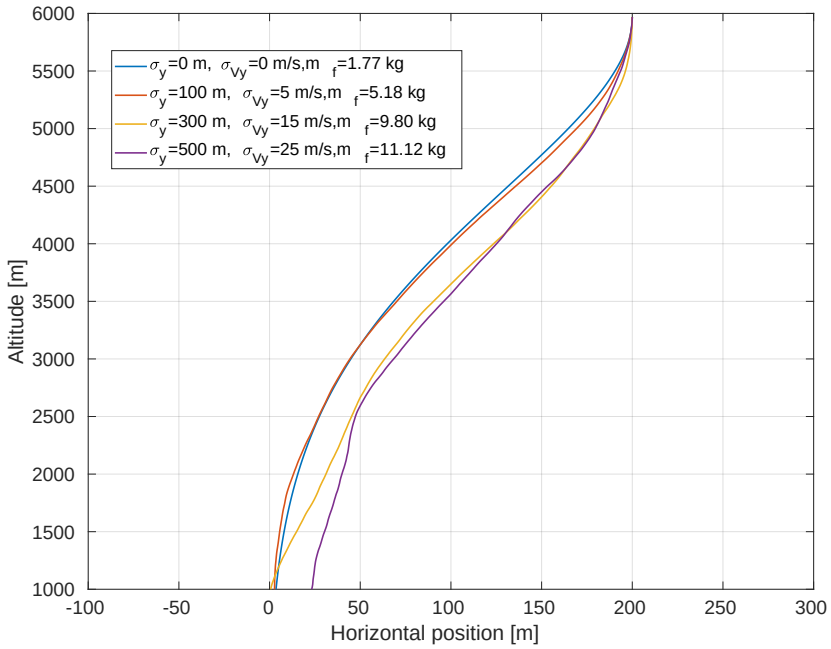

Figure 8.10: Effect of navigation error (navigation update frequency $\omega_{\text{nav}} = 10$ Hz) on the performance of the guided parachute descent control concept (IC from Table 8.3 except $y_{1,0} = y_{2,0} = y_{3,0} = 200$ m).

respect to the inertial space. This accuracy varies from 500 m to 1 km for standard systems and can be improved to 100 m if orbital imaging is integrated. Further information about optical navigation for Mars can be found in Johnson et al. [2015]. Future improvements, triggered by the need to use optical navigation also during the parachute flight, could yield optical navigation systems that can work also at higher altitudes over the surface of Mars.

It is remarked that parachute descent control on Earth can already achieve pinpoint landing accuracy. This is possible thanks to the longer descent time and, most of all, to the use of GPS navigation, that is clearly unavailable on Mars, and wind probes placed in the landing site area to offer real-time wind speed estimations. This second tool could eventually be adapted for a Mars landing.

Figure 8.10 shows how the performance and efficiency of the parachute descent guidance system vary for different navigation errors with a magnitude that is realistic for an optical system according to the data reported above. What is particularly evident is that a decrease in the accuracy of the navigation system causes significant increases in the consumption and horizontal position error at target altitude. In fact, even a small sample 200 m horizontal position error can require about 10 kg of fuel to be compensated. Also, these trajectories have been obtained by assuming a GNC system update frequency of 10 Hz. It was verified that increasing this parameter beyond 10 Hz has a marginal effect on the consumption but can contribute to make the trajectory smoother.

The navigation system has to determine not only the position and velocity of the spacecraft, but also its attitude and in particular its orientation around the rotational symmetry axis that, in steady-state conditions, is placed perpendicularly with respect to the surface of Mars. The accuracy of the navigation system in estimating the attitude of the spacecraft is key for the control system that has to generate the commanded thrust force according to the orientation of the vehicle. Other aspects of the control system that affect with variable magnitude the performance of the parachute horizontal position control concept include the delay of the controller in achieving the desired thrust level, its accuracy, the configuration of the thrusters on the backshell and the possibility to tilt them so that to be able to push horizontally more precisely.

9

CONCLUSIONS AND RECOMMENDATIONS

The previous chapters were dedicated to an extensive analysis of the stability properties of parachute-backshell-payload systems and to the evaluation of the potentialities of a guidance system for controlling the trajectory of the spacecraft during the parachute descent on Mars. The analysis has been guided by the research question and subquestions introduced in Chapter 1. In Section 9.1 the results of the study will be summarized to give concise replies to these questions. The analysis, however, has highlighted some interesting aspects of the research that should be studied in more detail. These are briefly discussed in Section 9.2.

9.1. CONCLUSIONS

In this section we will respond to the question addressed in Chapter 1:

Q1. *What are the most relevant external disturbances during the parachute descent on Mars?*

R1. During the parachute descent on Mars the spacecraft can encounter gusts and turbulences. These phenomena have a more significant effect on the attitude behaviour of the non-rigid vehicle and cause dangerous oscillations of its body elements. In particular, a typical 20 m/s Mars gust causes attitude oscillations that have a larger amplitude with respect to those due to a typical Mars turbulence, but the latter can result in a resonance effect if the input frequency of the disturbance matches with the natural oscillation frequency of one of the elements of the spacecraft. The descent trajectory is instead very sensitive to lateral wind that causes the vehicle to drift up to a few km away from its reference path. In general, horizontal perturbations are more critical than vertical ones both from the points of view of the effect they have on the attitude and on the trajectory of the vehicle.

Q2. *What actuators are more appropriate for controlling the spacecraft descent trajectory on Mars and what guidance strategy could be more performing?*

R2. The use of backshell thrusters for guiding the spacecraft during the parachute descent seems to represent the most performing choice compared to others as, for example, a guided parafoil or a gliding parachute (commanded by varying the length of its risers). In fact, a parafoil is in general a less robust solution with respect to a parachute for space recovery applications and, also, the size of a Mars parafoil, for compensating the low density of the atmosphere, would be prohibitive. With respect to the gliding parachute, instead, backshell thrusters ensure a much better responsiveness. Also, backshell thrusters have already been used for deceleration purposes on the MPF spacecraft. An appropriate guidance strategy for the guided descent concept is to use the backshell thrust to control the horizontal position and velocity of the spacecraft. These are indeed the state variables that most influence the size of the final landing ellipse on Mars.

Q3. *What are the key characteristics of modelling the spacecraft as a rigid body or a multibody system? When are the differences between these two approaches significant?*

R3. A rigid body model can only reproduce the pendulum motion mode of the parachute-payload vehicle. This approach is appropriate for rough estimations of its position-velocity descent trajectory and is simple enough if analytical data have to be derived. For simulating the relative motion of the elements of the spacecraft, a

multibody model is needed. With this second approach one can simulate with a much higher fidelity the dynamics of the system. In particular, the time required for designing a multibody model using the method of Neustadt is significantly lower than with other approaches. This is why this formulation is particularly indicated for preliminary studies.

Q4. *How do the the key system parameters determine the dynamic properties of the parachute-payload spacecraft in both the cases of passive and guided descent?*

R4. The analysis of the previous chapters has highlighted that the stability characteristics of the rigid body open-loop parachute-payload system depend on the balance between its aerodynamic and inertia properties. In general, if the former dominates over the latter, in case of a perturbation the system will tend back faster to the vertical flight steady-state condition. At the same time, however, a lower relative weight of the inertia of the system makes it more sensitive to external disturbances. The most important parameters to adjust for optimizing the dynamic response of the system as desired are the risers' lengths. Other parameters, such as the size of the parachute or the payload mass, are more bounded by other requirements of the specific EDL mission. The response of the closed-loop system is analogous to that of the open-loop system except for the horizontal motion. This, as a result of the control action, governed by the gains K_p and K_d, stabilizes around the condition y=0, V_y=0.

Q5. *How much control authority can the designed guided descent system yield and what target accuracy it can achieve? How is the system performance influenced in case of external perturbations?*

Q6. *What are the disadvantages of controlling the parachute descent spacecraft trajectory with the designed system?*

Q7. *How is the guided descent system influenced by the performance of the navigation and control subsystems of the spacecraft?*

R5-6-7. From the results in Chapter 8.2 it emerges that the guided descent system, in absence of wind, is able to significantly reduce the horizontal position error. The position-velocity target accuracy, however, decreases for large initial horizontal position errors and is around 60 m and 5 m/s if the initial error is 900 m. This can be considered to be the limit of the system. The first disadvantage of using it is the fact that the use of thrust significantly affect the attitude of the system. It has been verified that a sudden push at $T_{\max}$ of 500 N, that has been estimated to be an appropriate value with respect to the aim and constraints of the mission, causes dangerous oscillations of the elements non-rigid spacecraft. However, a 20 m/s horizontal gust has been proved to be more critical for its attitude behaviour, this meaning that the response to gusts should still be used as primary test bed for the stability properties of a Mars descent spacecraft, even in case this is going to be equipped with a guidance system analogous to the one designed here. The system can compensate a horizontal constant wind speed up to 26 m/s that represents an extreme condition (the average is around 5-10 m/s according to the data from Prince et al. [2008]). Also, the backshell thrust control system performance is only marginally affected by the presence of turbulences and gusts during the descent. The fuel needed for the descent depends on the conditions the spacecraft has to face. With a total amount of 8 kg the system can correct an horizontal position error of 900 m. This is assumed to be enough for most mission scenarios. If the system comprises also 6 thrusters then the total redundant mass of the guidance and control unit can be estimated around 20 kg. This estimation, however, greatly varies in the real case due to navigation error that causes the fuel efficiency of the system to reduce dramatically. The additional vehicle mass due to the guidance and control hardware and fuel mass is a second disadvantage of using the descent guidance system.

With these information it is now possible to give a concise reply to the main research question:

Q. Can a guidance system for controlling the spacecraft parachute descent trajectory represent a performing and efficient solution for increasing the landing accuracy on Mars?

R. Yes, a guidance system for controlling the spacecraft parachute descent could represent a performing and efficient solution for increasing the landing accuracy on Mars, but more research about its potentialities and its drawbacks is needed.

9.2. RECOMMENDATIONS

The results obtained are encouraging. This suggest that continuing the research related to parachute descent guidance is desirable, because it could lead to a system that can contribute to the achievement of pinpoint landing accuracy on Mars. Some aspects of the problem analysed in this thesis, however, shall be analysed in more detail:

1. *Sensitivity analysis of the system parameters:* in the present study the influence of the system parameters on its dynamics has been evaluated qualitatively using two tools. First, the analytical expressions derived in Chapters 6 and 7 for the rigid body model and then the response simulations obtained with the multibody model. This type of approach, however, cannot give detailed information about the effect of variation of each single parameter when it influences multiple aspects of the dynamics of the system. In this case a sensitivity analysis with the analytical formulas and the multibody model could yield more in depth results.

2. *Guidance during the parachute transient phase:* in the present study we focused on evaluating the potentialities of a guidance system that can control the trajectory of the spacecraft during the steady-state parachute flight. It would be interesting to understand whether a similar system can also be implemented for the flight segment just after the parachute deployment. In this case the system would have more time to correct the position error and could contribute more significantly to the reduction of the size of the landing ellipse.

3. *Analytical study with multibody model:* the multibody model developed with the approach of Neustadt is more extensive and complex than the rigid body model. Nevertheless, its EOM are simpler and offer a better insight than those that can be derived with other multibody mechanics methodologies such as the one of Wittenburg [2008]. It would be interesting to determine analytical expressions that describe the dynamics of the descent spacecraft also using the EOM of the multibody model.

4. *More extensive multibody model with Neustadt:* the multibody model that has been developed is planar and does not consider the aerodynamic contributions of the backshell and payload elements. The development of a 3D multibody model using the Neustadt approach that also considers the aerodynamics of the bodies other than the parachute, its inflation, a more accurate definition of the elasticity of the risers and the rotation about the rotational symmetry axis would represent a valuable tool for accurate descent simulation. An additional value added for this tool would also be the integration with the EMCD for simulating the atmosphere of Mars.

5. *Analysis of vertical disturbances:* in the present study we focused on the analysis of atmospheric perturbations that impact perpendicularly the descending parachute-paylaod vehicle. These are indeed more critical for its attitude stability and the mission landing accuracy. However, it would be interesting to also study in detail the response of the system to perturbations that are parallel with respect to its rotational symmetry axis.

In addition to these recommendations, some research topics related to the present study include:

1. *An optical navigation for Mars parachute descent:* the performance of the descent horizontal position control system is particularly sensitive to navigation accuracy. Advancements in optical navigation for Mars are key for enabling this technology. In particular, it would be interesting to increase the operative range of current optical system so that to reach the altitude band where the parachute descent takes place.

2. *A more performing guidance algorithm:* the PD controller developed for the purpose of studying the feasibility of the concept is not enough for a system that has to be equipped on a real spacecraft. In particular, a guidance scheme that can take into account the presence of wind, capable of rescheduling the target depending on the flight situation and that is also more optimal and accurate, is highly desirable.

3. *A backshell thrust control system:* the guidance logic yields a commanded thrust according to a certain estimated state error. The thrust command that it generates has to be reproduced by the control system according to the current spacecraft attitude. The development of the control system could also take into account the possibility to tilt the thrusters with respect to the backshell and determine an optimal configuration for the thrusters, tank and so on.

BIBLIOGRAPHY

Abdulkadir, L. [2011]. "Stability of Multibody Systems for Mars Descent and Landing", Thesis, TU Delft.

Baker, R. S., Casillas, A. R., Guernsey, C. S., and Weiss, J. M. [2014]. "Mars Science Laboratory Descent-Stage Integrated Propulsion Subsystem: Development and Flight Performance", *Journal of Spacecraft and Rockets*, volume 51, no. 4, pp. 1217–1226, doi:10.2514/1.A32788.

Ball, A., Garry, J., Lorentz, R., and Kerzhanovich, V. [2007]. *Planetary Landers and Entry Probes*, Cambridge University Press.

Bayle, O., Lorenzoni, L., Blancquaert, T., Langlois, S., Walloschek, T., and Portigliotti, S. [2016]. "Exomars Entry Descent and Landing Demonstrator Mission and Design Overview", *Nasa Solar System*, , no. 1, p. 10.

Benney, R., Barber, J., McGrath, J., McHugh, J., Noetscher, G., and Tavan, S. [2005]. "The Joint Precision Airdrop System Advanced Concept Technology Demonstration", *18th AIAA Aerodynamic Decelerator Systems Technology Conference and Seminar*, doi:10.2514/6.2005-1601.

Brand, T., Fuhrman, L., Geller, D., Hattis, P., Paschall, S., and Tao, Y. [2004]. "GN&C Technology Needed to Achieve Pinpoint Landing Accuracy at Mars", *AIAA/AAS Astrodynamics Specialist Conference and Exhibit*, doi:10.2514/6.2004-4748.

Braun, R., Spencer, D., Kallemeyn, P., Vaughan, R., Braun, R., Spencer, D., Kallemeyn, P., and Vaughan, R. [1997]. "Mars Pathfinder atmospheric entry navigation operations", *22nd Atmospheric Flight Mechanics Conference*, doi:10.2514/6.1997-3663.

Cheng-Chih, C. [2006]. "Development of advanced entry, descent, and landing technologies for future Mars missions", *Aerospace Conference, 2006 IEEE*, p. 8 pp., doi:10.1109/AERO.2006.1655784.

Cruz, J., Mineck, R., Keller, D., and Bobskill, M. [2003]. "Wind Tunnel Testing of Various Disk-Gap-Band Parachutes", *17th AIAA Aerodynamic Decelerator Systems Technology Conference and Seminar*, doi:10.2514/6.2003-2129.

Cruz, J. R., Way, D. W., Shidner, J. D., Davis, J. L., Adams, D. S., and Kipp, D. M. [2014]. "Reconstruction of the Mars Science Laboratory Parachute Performance", *Journal of Spacecraft and Rockets*, volume 51, no. 4, pp. 1185–1196, doi:10.2514/1.A32816.

Dellicker, S., Benney, R., LeMoine, D., Brown, G., Gilles, B., and Howard, R. [2003]. "Steering a Flat Circular Parachute - They Said It Couldn't Be Done", *17th AIAA Aerodynamic Decelerator Systems Technology Conference and Seminar*, doi:10.2514/6.2003-2101.

Desai, P. and Knocke, P. [2004]. "Mars Exploration Rovers Entry, Descent, and Landing Trajectory Analysis", *AIAA/AAS Astrodynamics Specialist Conference and Exhibit*, doi:10.2514/6.2004-509210.2514/6.2004-5092.

Doherr, K.-F. and Schilling, H. [1991]. "9DOF-simulation of rotating parachute systems", *11th Aerodynamic Decelerator Systems Technology Conference*, doi:10.2514/6.1991-877.

D'Souza, A. F. [1988]. *Design of Control Systems*, Prentice-Hall International Editions, Prentice-Hall.

Edquist, K. T., Desai, P. N., and Schoenenberger, M. [2011]. "Aerodynamics for Mars Phoenix Entry Capsule", *Journal of Spacecraft and Rockets*, volume 48, no. 5, pp. 713–726, doi:10.2514/1.46219.

Fallon, E. [1991]. "Parachute dynamics and stability analysis of the Queen Match Recovery System", *11th Aerodynamic Decelerator Systems Technology Conference*, doi:10.2514/6.1991-879.

Forget, F., Hourdin, F., Fournier, R., Hourdin, C., Talagrand, O., Collins, M., Lewis, S. R., Read, P. L., and Huot, J.-P. [1999]. "Improved general circulation models of the Martian atmosphere from the surface to above 80 km", *Journal of Geophysical Research: Planets*, volume 104, no. E10, pp. 24 155–24 175, doi:10.1029/1999JE001025.

Golnaraghi, F. and Kuo, B. [1987]. *Automatic Control Systems*, volume 212, 9th edition, Wiley, doi:10.1038/2121031a0.

Guglieri, G. [2012]. "Parachute-payload system flight dynamics and trajectory simulation", *International Journal of Aerospace Engineering*, volume 2012, doi:10.1155/2012/182907.

Haberle, R., Clancy, R., Forget, F., Smith, M., and Zurek, R. [2017]. *The Atmosphere and Climate of Mars*, Cambridge University Press, doi:10.1017/âĂŃ9781139060172.

Hattis, P., Fill, T., Rubenstein, D., Wright, R., and Benney, R. [2000]. "An advanced on-board airdrop planner to facilitate precision payload delivery", *Modeling and Simulation Technologies Conference*, doi:10.2514/6.2000-4307.

Heinrich, H. G. and Haak, E. L. [1971]. "Stability and Drag of Parachutes with Varying Effective Porosity", Technical report, Air Force Flight Dynamics Laboratory.

Helmut, G. H. and Lawrence Jr., W. R. [1965]. "Dynamic stability of a parachute point-mass load system", Report FDL-TDR-64-126, Department of Aeronautics and Engineering Mechanics, University of Minnesota, Minneapolis, Minnesota.

Holmberg, N. A., Faust, R. P., and Holt, H. M. [1980]. "Viking '75 Spacecraft Design and Test Summary: Lander design", Report, NASA Langley Research Center.

Hume, R. [1973]. "A Two dimensional Mathematical Model of a Parachute in Steady Descent", Technical Report 1260, Aeronautical Research Council.

Ibrahim, S. and Engdahl, R. [1974]. "Parachute Dynamics and Stability Analysis", Technical report, System and Research Center Honeywell Inc.

Johnson, A. E., Cheng, Y., Montgomery, J. F., Trawny, N., Tweddle, B., and Zheng, J. X. [2015]. "Real-Time Terrain Relative Navigation Test Results from a Relevant Environment for Mars Landing", *AIAA Guidance, Navigation, and Control Conference*, doi:10.2514/6.2015-0851.

Jorgensen, D. and Hickey, M. [2005]. "The AGAS 2000 Precision Airdrop System", *Infotech@Aerospace*, doi:10.2514/6.2005-7072.

Kaas, D., Schofield, J., Michaels, T., Rafkin, S., Richardson, M., and Toigo, A. [2003]. "Analysis of atmospheric mesoscale models for entry, descent, and landing", *Journal of Geophysical Research: Planets*, volume 10, pp. 1–10, doi:10.1029/2003JE002065.

Karlgaard, C. D., Kutty, P., Schoenenberger, M., and Shidner, J. [2012]. "Mars Science Laboratory Entry, Descent, and Landing Trajectory and Atmosphere Reconstruction", Technical report.

Khalil, H. [2001]. *Nonlinear Systems*, 3rd edition, Prentice Hall.

Ley, W., Wittmann, K., and Hallmann, W. [2009]. *Handbook of Space Technology*, John Wiley & Sons, Ltd.

Lingard, J., Underwood, J., Glynn, S., Franqueville, D., Arfi, P., Bayle, O., Potenza, F., and Portigliotti, S. [2009]. "ExoMars Parachute System", *20th AIAA Aerodynamic Decelerator Systems Technology Conference and Seminar*, doi:10.2514/6.2009-2975.

Lissauer, J. J. and de Pater, I. [2013]. *Fundamental Planetary Science*, Cambridge University Press, New York.

McKinney, J. and Lowry, C. [2009]. "Mars Precision Landing Using Guided Parachutes", *20th AIAA Aerodynamic Decelerator Systems Technology Conference and Seminar*, doi:10.2514/6.2009-2983.

Mendeck, G. F. and Craig McGrew, L. [2014]. "Entry Guidance Design and Postflight Performance for 2011 Mars Science Laboratory Mission", *Journal of Spacecraft and Rockets*, volume 51, no. 4, pp. 1094–1105, doi:10.2514/1.A32737.

Millour, E., Forget, F., Spiga, A., Navarro, T., Madeleine, J. B., Montabone, L., Pottier, A., Lefèvre, F., Montmessin, F., Chaufray, J.-Y., Lòpez-Valverde, M. A., Gonzàlez-Galindo, F., Lewis, S. R., Read, P. L., Lebonnois, S., Huot, J. P., Desjean, M. C., and Team, M. D. [2015]. "The Mars Climate Database (MCD version 5.2)", in *European Planetary Science Congress 2015*, volume 10.

Mooij, E. [1998a]. "Aerospace-plane flight dynamics: analysis of guidance and control concepts", Ph.D. thesis, TU Delft.

Mooij, E. [1998b]. *Linear quadratic regulator design for an unpowered winged re-entry vehicle*, Delft University Press.

Mooij, E. [2015]. *Re-entry Systems: Lecture Notes Course AE4870B*, TU Delft.

Mooij, E. D. S. B., Wijnands, Q. E., and Schat, B. E. [2003]. "9 Dof Parafoil/Payload Simulator Development and Validation", *AIAA Modeling and Simulation Technologies Conference and Exhibit 2003*, , no. August, pp. 1–12, doi:doi:10.2514/6.2003-5459.

Müller, S., Wagner, O., and Sachs, G. [2003]. "A High-fidelity Nonlinear Multibody Simulation Model for Parafoil Systems", *17th AIAA Aerodynamic Decelerator Systems Technology Conference and Seminar*, , no. May, doi: 10.2514/6.2003-2120.

Murray, R. M., Li, Z., and Sastry, S. S. [1994]. *A Mathematical Introduction to Robotic Manipulation*, volume 29, CRC Press, doi:10.1.1.169.3957.

Neustadt, M., Ericksen, R. E., Guiteras, J., and Larrivee, J. a. [1967]. "A parachute recovery system dynamic analysis.", *Journal of Spacecraft and Rockets*, volume 4, no. March, pp. 321–326, doi:10.2514/3.28860.

Nielsen, T. T. [2016]. "EXOMARS 2016 - Schiaparelli Anomaly Inquiry", Technical report, ESA.

Northey, D. [2003]. "The Main Parachute for the Beagle 2 Mars Lander", *17th AIAA Aerodynamic Decelerator Systems Technology Conference and Seminar*, , no. May, doi:10.2514/6.2003-2170.

Ogata, K. [2010]. *Modern Control Engineering*, Prentice Hall, doi:10.1109/TAC.1972.1100013.

Petrosyan, A., Galperin, B., Larsen, S. E., Lewis, S. R., Määttänen, A., Read, P. L., Renno, N., Rogberg, L. P. H. T., Savijärvi, H., Siili, T., Spiga, A., Toigo, A., and Vázquez, L. [2011]. "THE MARTIAN ATMOSPHERIC BOUNDARY LAYER", *Reviews of Geophysics*, volume 49, no. 3, p. RG3005, doi:10.1029/2010RG000351.

Pope, S. [2000]. *Turbulent Flows*, Cambridge University Press.

Portigliotti, S., Dumontel, M., and Capuano, M. [2010]. "Landing Site Targeting and Constraints for Exomars 2016 Mission", Number June, International Planetary Probe Workshop (2010), pp. 14–18.

Press, W., Flannery, B., Teukolsky, S., and Vetterling, W. [2007]. *Numerical Recipes: The Art of Scientific Computing*, volume 29, Cambridge University Press, doi:10.2307/1269484.

Prince, J., Desai, P., Queen, E., and Grover, M. [2008]. "Mars Phoenix Entry, Descent, and Landing Simulation Design and Modeling Analysis", *AIAA/AAS Astrodynamics Specialist Conference and Exhibit*, doi:10.2514/6. 2008-7507.

Spencer, D. A., Blanchard, R. C., Braun, R. D., Kallemeyn, P. H., and Thurman, S. W. [1999]. "Mars Pathfinder Entry, Descent, and Landing Reconstruction", *Journal of Spacecraft and Rockets*, volume 36, no. 3, pp. 357–366, doi:10.2514/2.3478.

Spencer, D. a. and Braun, R. D. [1996]. "Mars Pathfinder atmospheric entry - Trajectory design and dispersion analysis", *Journal of Spacecraft and Rockets*, volume 33, no. 5, pp. 670–676, doi:10.2514/3.26819.

Sreenivasan, K. [1991]. "Fractals And Multifractals In Fluid Turbulence", *Annual Review of Fluid Mechanics*, volume 23, no. 1, pp. 539–600, doi:10.1146/annurev.fluid.23.1.539.

Striepe, S. A., Way, D. W., Dwyer, A. M., and Balaram, J. [2006]. "Mars Science Laboratory Simulations for Entry, Descent, and Landing", *Journal of Spacecraft and Rockets*, volume 43, no. 2, pp. 311–323, doi:10.2514/1.19649.

Vishnyak, A. [1993]. "Simulation of the Payload-Parachute-Wing System Flight Dynamics", *American Institute of Aeronautics and Astronautics*.

Wie, B. [2008]. *Space Vehicle Dynamics and Control, Second Edition*, American Institute of Aeronautics and Astronautics, doi:10.2514/4.860119.

Witkowski, A., Kandis, M., Bruno, R., and Cruz, J. [2005]. "Mars Exploration Rover Parachute System Performance", *18th AIAA Aerodynamic Decelerator Systems Technology Conference and Seminar*, doi:10.2514/6. 2005-1605.

Wittenburg, J. [2008]. *Dynamics of Multibody Systems*, Springer-Verlag Berlin Heidelberg.

Wolf, A. A., Acikmese, B., Cheng, Y., Casoliva, J., Carson, J. M., and Ivanov, M. C. [2011]. "Toward improved landing precision on Mars", in *2011 Aerospace Conference*, pp. 1–8, doi:10.1109/AERO.2011.5747243.

Wolf, A. A., Graves, C., Powell, R., and Johnson, W. [2005]. "Systems for pinpoint landing at Mars", *Advances in the Astronautical Sciences*, volume 119, no. SUPPL., pp. 2677–2696.